

**EINBLICKE IN DIE MOLEKULAREN MECHANISMEN ZUR REGULIERUNG DER
AKTIVITÄT VON MULTIDOMAIN-PROTEINEN IN LEBENDEN ZELLEN MIT HILFE
VON FRET-FLIM UNTERSUCHUNGEN**

**INSIGHTS INTO MOLECULAR MECHANISMS REGULATING THE ACTIVITY OF
MULTIDOMAIN PROTEINS IN LIVING CELLS USING FRET-FLIM**

Dissertation

zur Erlangung des akademischen Grades

**doctor rerum naturalium
(Dr. rer. nat.)**

genehmigt durch die Fakultät für Naturwissenschaften
der Otto-von-Guericke-Universität Magdeburg

Von **Master of Science in Physics Deepak Kumaran Nair**

geb. am 10.03.1980 in Mararikulam, Kerala, India

Gutachter: **Prof. Dr. Stephan Diekmann**
Privatdozent Dr. Reinhard König

eingereicht am **01. Oktober 2007**

verteidigt **19. März 2008**

Dedicated to my family and teachers for their love and support, which have encouraged and motivated me to achieve what I have...

ACKNOWLEDGEMENTS

I thank my wife Mini, whose love and support has inspired me in research and life. I thank my daughter Naina, who along with my wife has silently suffered all the hardships in the last few months.

I sincerely thank Prof. Eckart Gundelfinger for motivating me to learn and appreciate cell biology and I will always be grateful for his help and consideration shown towards the successful completion of my work. I thank Dr. Werner Zuschratter and Dr. Roland Hartig for giving me the opportunity to work in their laboratories. I thank them for their belief in me, by giving me the opportunity to work in both biology and physics. I thank Prof. Burkhard Schraven and Dr. Reinhard König for their encouragement and opinions.

One of the special people I would like to thank is Kathrin; without whose timely and sincere effort I would not have completed many experiments in time.

I am grateful to Prof. Thomas Kuner, Prof. Athar Chishti, Prof. Hannes Stockinger, Prof. Philip Beesley Dr. Michael Kreutz, Dr. Toshihiko Hanada and Dr. Karl-Heinz Smalla for providing the constructs used in my work.

I am very indebted to Dr. Ronald Steffen, a friend, a co-worker and a very patient scientist who taught me to appreciate the complexities of photophysical processes. I am extremely thankful to Dr. Ulrich Thomas who spent a lot of his time to make me understand various aspects of molecular biology and protein biochemistry.

I am very thankful to Moni, Heidi, and Ilona who always found time to help me in my need. I also thank Ela, Roser and Falco who had spent their valuable time to make me a better cell biologist. I am grateful to the assistance from mechanical and electrical workshops to make the work more comfortable.

I would like to thank the members of the Neurochemistry Department at IFN and Institute of Immunology, Magdeburg for their valuable suggestions and help in improving my work.

This list will not be complete without mentioning many people whom I cannot name but only thank for their love, support, and concern.

I would also like to thank Deutsche Forschungsgemeinschaft for funding me through the project FOR-521-HA 3498/1.

I would like to thank my teachers who have moulded me into what I am and I hope that I have held their esteem with this humble effort. I thank my parents and my family who taught me to work hard in whatever I did. I thank them for their love, prayers, and the encouragement they gave whenever I expressed my interest for higher studies. Finally, I thank god for giving me good teachers and a loving family.

01-10-2007

Deepak Nair

TABLE OF CONTENTS

SUMMARY	1
1 INTRODUCTION.....	2
1.1 Immune system.....	2
1.2 Adaptive immune response.....	2
1.3 T cells and B cells.....	3
1.4 Antigen presenting cells.....	3
1.5 Immunological synapse:-formation and molecular organisation.....	4
1.6 Src kinases: structure and function	7
1.6.1 Lck	9
1.7 Discs Large family of proteins and the generation of modular scaffolds	10
1.7.1 SAP97/hDlg	11
1.8 Aims.....	12
1.8.1 Real-time conformational changes of Lck	13
1.8.2 Calicum-dependent conformational changes of SAP97 and PSD95	14
1.8.3 Role of Lck-SAP97 association in synaptic stabilisation.....	16
2 THEORETICAL FOUNDATIONS AND INSTRUMENTATION.....	17
2.1 Fluorescence of organic molecules.....	17
2.2 Theory of spectral separation.....	19
2.3 Fast excited state reactions	22
2.4 FRET.....	24
2.5 Fluorescence Lifetime Imaging Microscopy to probe FRET	26
2.6 FLIM-FLMS.....	27
2.6.1 Time and Space Correlated Single Photon Counting (TSCSPC)	27
2.6.2 Detectors	27
2.6.3 Instrumentation	28
2.6.4 Steady state imaging.....	30
2.6.5 Calibration of the setup	30
2.6.6 Data analysis	32
2.7 Fluorescence tags to image macromolecular dynamics.....	35
2.8 Photophysics of GFP based FRET.....	36
3 MATERIALS AND METHODS.....	37
3.1 Materials	37
3.1.1 Chemicals.....	37
3.1.2 Bacteria and mammalian cell culture media and antibiotics	37
3.1.3 Buffers.....	37
3.1.4 Cell strains.....	37
3.1.5 Antibodies	38
3.1.6 GFP fusion constructs	38
3.1.7 Primers	39
3.1.8 Animals	39
3.2 Methods	39
3.2.1 Biochemical methods.....	39
3.2.2 Cell biological methods.....	42
3.2.3 Structural modelling of Lck	44
4 RESULTS.....	45
4.1 Photophysics of FRET between CFP and YFP in living cells.....	45
4.1.1 Fluorescence dynamics of ECFP in Jurkat T cells	45
4.1.2 Fluorescence emission dynamics of size variants of Clomeleon.....	46
4.1.3 Fluorescence emission spectra of size variants of Clomeleon.....	47
4.1.4 Modelling of intensity decays	47
4.1.5 Fluorescence lifetime dynamics of size variants of Clomeleon	48
4.2 Activity-dependent conformational changes of Lck in living cells	53

4.2.1 Domain organisation of Lck fusion constructs	54
4.2.2 Fluorescence dynamics of Lck FRET-control	55
4.2.3 Fluorescence emission spectrum of Lck FRET variants	55
4.2.4 Fluorescence lifetime dynamics of Lck FRET variants	55
4.2.5 Intermolecular FRET in Lck	57
4.2.6 Real-time conformational changes of Lck upon T-cell receptor stimulation	58
4.2.7 Real-time conformational distribution of Lck upon contact with APC	60
4.3 Conformational dynamics of SH3-HOOK-GUK units of MAGUKs in COS7 cells	61
4.3.1 Organisation of GFPs in SH3-HOOK-GUK module	61
4.3.2 Fluorescence dynamics of the PSD95 ^{FRET control}	61
4.3.3 Fluorescence dynamics of the FRET constructs in COS7 cells	62
4.3.4 Fluorescence dynamics of PSD95 ^{FRET}	62
4.3.5 Fluorescence dynamics of SAP97 ^{FRET}	64
4.4 Relevance of alternative splicing of insertion I1 in SAP97/hDlg in Jurkat T cells	66
4.4.1 Distribution of I1 (I1A and I1B) insertions of SAP97/hDlg in Jurkat T cells	66
4.4.2 Subcellular localisation of endogenous SAP97/hDlg in Jurkat T cells	67
4.4.3 Localisation of I1-containing isoforms to the cell-bead contact	68
5 DISCUSSION	70
5.1 FRET as excited state reactions	70
5.1.1 Kinetic model of FRET from a two state donor to single state acceptor	71
5.1.2 Significance of DAS in living cells	73
5.2 Activity dependent conformational changes of Lck: structure as a key to the function	74
5.2.1 Conformations of Lck in unstimulated Jurkat T cells	74
5.2.2 Conformational dynamics of Lck in stimulated Jurkat T cells	77
5.3 Calcium-dependent conformational changes of MAGUKs: modular scaffolds and near- membrane complexes	78
5.3.1 Regulatory structure of Dlg family proteins and comparison with Src kinases	78
5.3.2 Calcium-dependent conformational changes of Dlg family of proteins	79
5.3.3 Role of MAGUKs in near-membrane scaffolds	80
5.4 Lck as a regulatory protein affecting localisation SAP97/hDlg to synapses	81
5.4.1 Relevance of I1 splicing on the recruitment of SAP97/hDlg to the immunological synapse	81
5.4.2 Role of SAP97/hDlg-Lck interaction in the immunological synapse	82
6 CONCLUSIONS	84
REFERENCES	86
ABBREVIATIONS	96
CURRICULAM VITAE	99
SCIENTIFIC PUBLICATIONS	100

SUMMARY

Macromolecular association and dissociation are key events involved in the subcellular organisation below the limit of optical resolution. Foersters/Fluorescence Resonance Energy Transfer (FRET) in combination with Fluorescence Lifetime Imaging Microscopy (FLIM) is among the best quantitative methods to probe these events at the subcellular regime. In this work, FRET dynamics of Green Fluorescent Protein (GFP) based tandem constructs were investigated in living cells using a combination of FLIM and Fluorescence Lifetime Micro-Spectroscopy (FLMS) at picosecond time resolution and nanometer spectral resolution. Simultaneous detection and analysis of intensity decays of donor and acceptor probes as coupled excited state reactions identified the lifetimes participating in energy transfer. This method differentiated the involvement of multiple conformations of Cyan Fluorescent Protein (CFP) in energy transfer to Yellow Fluorescent Protein (YFP), by plotting pre-exponential factors of individual lifetimes along the wavelength resulting in the Decay Associated Spectra (DAS). A change in sign of pre-exponential factors from positive to negative at the acceptor emission maxima confirmed FRET in the multiexponential lifetime analysis. This approach discriminated the intramolecular energy transfer dynamics between the tandem constructs which differed in spacer lengths down to eight amino acids. The results allowed to obtain a kinetic model for FRET occurring from multi-exponential CFP to monoexponential YFP, which was a basis for interpreting results using the same fluorophores in the context of various biological applications like protein folding and conformational changes.

Lymphocyte specific protein tyrosine kinase (Lck) is among the first proteins to be recruited to the immunological synapse, implicating its importance in T cell signalling. Results from FRET-FLIM studies suggested that in resting T-lymphocytes Lck exists in equilibrium between closed (passive) and open (active) conformations. The structural prediction from the FRET-FLIM studies was coherent with the existing hypothesis for the structure of Src kinases. In stimulated T-lymphocytes, Lck indicated a temporary reversible change in its conformation from the closed to an open state. These transient changes were in correlation with the reported kinase activity of Lck, where an initial increase in kinase activity was observed during the early moments of formation of an immunological synapse, which returned to the basal level in 20 min.

Membrane-associated guanylate kinases (MAGUKs) are multidomain molecules pivotal in the architecture of various cell-adhesion interfaces. Synapse-associated protein 97/Human Discs Large (SAP97/hDlg) interacts with the SH3 domain of Lck using the proline-rich region at the N-terminus of the protein. The exon encoding this proline-rich region is subject to alternative splicing. The absence of Lck as well as the expression of the protein lacking its proline-rich region was observed to affect the localisation of SAP97/hDlg to T cell-bead interfaces or mock immunological synapses. The changes of intramolecular FRET in the conserved SH3-HOOK-GUK unit at the C-terminus of different MAGUKs (SAP97/hDlg and SAP90/PSD95) in response to elevated calcium levels were investigated. The observed changes were ascribed to the formation of parallel or anti-parallel dimers, creating a rigid molecular framework of cytoplasmic scaffolds.

Thus, with a combination of advanced microscopic methods, cell biology and molecular modelling, activity-dependent structural regulation and intramolecular association of multidomain proteins were studied during the initial moments of cell recognition events. The transient conformational changes and activity-dependent distribution of Lck and MAGUKs could be central in signal transduction machineries, efficiently distributing signals within the immunological synapse, and at the same time involved in preparing a dynamic molecular platform for assembling near-membrane scaffolding molecules.

1 INTRODUCTION

1.1 Immune system

An immune system is a collection of mechanisms within an organism that protects against infection by identifying and killing pathogens and tumour cells. It detects a wide variety of pathogens, such as viruses and parasitic worms and distinguishes them from the organism's normal cells and tissues. The detection is complicated, as pathogens adapt and evolve new ways to successfully infect the host organism. To survive this challenge, several mechanisms have evolved to recognise and neutralise pathogens. The immune systems of humans consist of many types of proteins, cells, organs, and tissues, which interact in an elaborate and dynamic network. The immune system protects organisms from infection with layered defences of increasing specificity. Most simply, physical barriers prevent pathogens such as bacteria and viruses from entering the body. If a pathogen breaches these barriers, the innate immune system provides an immediate, but non-specific response. Innate immune systems are found in all plants and animals. However, if pathogens successfully evade the innate response, vertebrates possess a third layer of protection, the adaptive immune system. Here, the immune system adapts its response during an infection to improve its recognition of the pathogen. This improved response is then retained after the pathogen has been eliminated, in the form of an immunological memory, and allows the adaptive immune system to respond faster and stronger each time this pathogen is encountered (Abbas and Lichtman, 2003; Janeway et al., 2001).

1.2 Adaptive immune response

The adaptive immune response is antigen-specific and requires the recognition of specific “non-self” antigens during a process called antigen presentation. Antigen specificity allows generation of responses that are tailored to specific pathogens or pathogen-infected cells. The ability to mount these tailored responses is maintained in the body by "memory cells". White blood cells or leukocytes are cells of the immune system which defend an organism against both infectious diseases and foreign materials. Several different and diverse types of leukocytes exist, but they are all produced and derived from a pluripotent cell in the bone marrow known as a hematopoietic stem cell. Leukocytes are found throughout the body, including the blood and lymph system. Lymphocytes are a class of white blood cells in the vertebrate immune system. By their appearance under the light microscope, there are two broad categories of lymphocytes, namely the large granular lymphocytes and the small lymphocytes. Functionally distinct subsets of lymphocytes correlate with their appearance.

Most, but not all large granular lymphocytes are more commonly known as the natural killer cells (NK cells). The small lymphocytes are the T cells and B cells. Lymphocytes play an important and integral role in the body's defences. An average human body contains about 10^{12} lymphoid cells, and the lymphoid tissue as a whole represents about 2% of the total body weight (Abbas and Lichtman, 2003; Janeway et al., 2001).

1.3 T cells and B cells

T cells and B cells are the major cellular components of the adaptive immune system (Delon and Germain, 2000; Germain et al., 2006). T cells are involved in cell-mediated immunity, whereas B cells are primarily responsible for humoral immunity (related to antibodies). The function of T cells and B cells is to recognise specific “non-self” antigens, during a process known as antigen presentation. Once they have identified an invader, the cells generate specific responses that are tailored to eliminate specific pathogens or pathogen infected cells (McHeyzer-Williams, 2003; Santana and Esquivel-Guadarrama, 2006). B cells respond to pathogens by producing large quantities of antibodies, which neutralise foreign objects like bacteria and viruses. In response to pathogens, some T cells called “helper T cells” produce cytokines that direct the immune response, whilst other T cells called “cytotoxic T cells” produce toxic granules that induce the death of pathogen infected cells (Dustin and Colman, 2002; Vyas et al., 2002). Following activation, B cells and T cells leave a lasting legacy of the antigens they have encountered, in the form of memory cells. Throughout the lifetime of an organism, these memory cells will “remember” each specific pathogen encountered, and are able to mount a strong response if the pathogen is detected again (Grimbacher et al., 2003; Lanzavecchia and Sallusto, 2000).

1.4 Antigen presenting cells

Lymphocytes distinguish infected cells from normal and uninfected cells by recognising alterations in levels of a surface molecule called Major Histocompatibility Complex (MHC). Antigen presenting cells (APC) are cells that display foreign antigen complexed with MHC on its surface (Huppa and Davis, 2003). T cells recognise this complex using their T cell receptor (TCR). Dendritic cells, macrophages, and B cells are the main types of APCs which can present MHC class II molecules. Dendritic cells (DC) have the broadest range of antigen presentation, and are probably the most important APC (Inaba and Inaba, 2005). Activated DCs are specially potent helper T cell activators because, as part of their composition, they express co-stimulatory molecules (Sims and Dustin, 2002; Tseng and Dustin, 2002). B cells, which express an antibody, can very efficiently present the antigen to

which their antibody is directed, but are inefficient APC for most other antigens (McHeyzer-Williams, 2003). There are also specialised cells in particular organs (e.g., microglia in the brain, Kupffer cells in the liver) derived from macrophages that are effective APCs as well. After dendritic cells or macrophages swallow pathogens, they usually migrate to the lymph nodes where most T cells are. This migration is done chemotactically; chemokines that flow in the blood and lymph vessels "draw" the APCs to the lymph nodes. During this migration, DCs undergo a process of maturation. In essence, they lose most of their ability to further swallow pathogens, and they develop an increased ability to communicate with T cells. Enzymes within the cell digest the swallowed pathogen into smaller pieces containing epitopes, which are then presented to T cells using MHC (Delon et al., 2002; Germain and Jenkins, 2004).

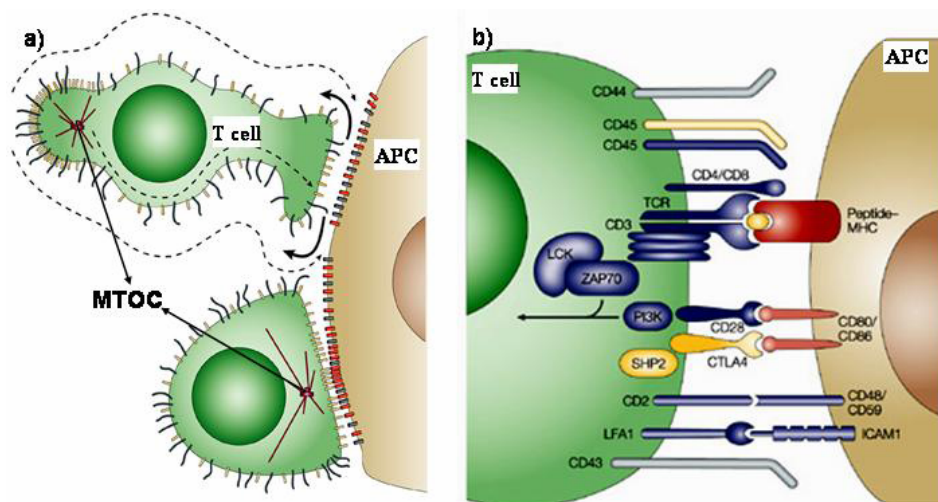


Figure 1.1) a) Morphological and cytoskeletal changes in the initial engagement and formation of a stable T-helper-cell synapse. After initial engagement of the T-cell receptor (TCR) with its cognate peptide-MHC complex, a T cell stops migrating and the microtubule organizing centre (MTOC) is reoriented beneath the immunological synapse. TCR molecules (yellow) are recruited into the synapse, and other cell-surface molecules (for example, CD43) are excluded. Stimulatory (red) and non-stimulatory (grey) peptide-MHC complexes are present at the synapse, as indicated. b) Overview of a mature T-cell synapse. A profile view showing a selection of the key ligand pairs and signalling molecules that are involved in T-cell recognition. The stimulatory peptide-MHC molecule is shown in red, activating/co-stimulatory molecules are in blue, inhibitory molecules are in yellow and molecules that are not contributing to signalling are in grey. The arrow indicates converging signals that lead to T-cell activation (Huppa and Davis, 2003).

1.5 Immunological synapse:-formation and molecular organisation

The word 'synapse' is derived from the Greek word meaning 'connection' or 'junction' between two similar entities (Oxford English Dictionary). It was first used to describe the junction between two chromosomes in the late 1800s, and shortly afterwards was used for neuronal connections. The term immune synapse was first chosen by M Norcross (Norcross, 1984) to describe T cell-antigen-presenting cell (APC) interactions, and also by W. Paul and colleagues (Paul and Seder, 1994). It is defined as any stable, flattened interface

between a lymphocyte or natural killer (NK) cell, and a cell or a surface that they are in the process of recognising (Figure 1.1.a). Conceptually, this term denotes the activation of these cells in the context of a highly organised and dynamic structure that can act as a platform for a bidirectional and cell-specific flow of information, which might offer additional layers of modulation to a cell's response (Delon and Germain, 2000; Huppa and Davis, 2003).

T cells are activated by recognition of foreign peptides displayed on the surface of Antigen presenting cells (APCs), an event that triggers an assembly of a complex microscale structure at the T cell–APC interface known as the immunological synapse (Figure 1.1). The first evidence of interference between receptor mediated signalling, cytoskeletal reorganisation and directed transport of cell-surface receptors originated from studies that used soluble antibodies to cross-link receptors and other cell-surface molecules for lymphocyte stimulation (Bromley et al., 2001; Dustin and Colman, 2002; Santana and Esquivel-Guadarrama, 2006). Using classical immunocytochemical analysis of fixed T cell–APC conjugates, Kupfer and colleagues first described the recruitment and distribution of molecules at the zone of T cell–APC contact. These investigators have reported that the TCR, the TCR-associated CD3- ϵ chain, CD4, LFA-1, the cytoskeletal protein Talin, as well as intracellular signalling molecules such as Src kinases like Lymphocyte specific protein tyrosine kinase (Lck) and Fyn, and protein kinase C (PKC)- θ are localised at the contact site (Kupfer and Singer, 1989a; Kupfer and Singer, 1989b; Kupfer et al., 1987; Kupfer et al., 1986; Monks et al., 1998; Monks et al., 1997). They also described the reorientation of the microtubule-organising centre and the Golgi apparatus to the vicinity of the synapse (Kupfer and Dennert, 1984). This phenomenon is described as capping, in which cell-surface receptors, filamentous actin and lipids such as gangliosides congregate towards one end of the cell (Figure 1.1) (Dustin, 2005; Huppa and Davis, 2003; Miletic et al., 2003). Immunofluorescence studies on fixed T cell–APC conjugates demonstrated the marked polarisation of the cell towards the APC (Manes and Viola, 2006; Montoya et al., 2002).

The major biochemical events taking place during the formation of an immunological synapse (Figure 1.2) can be considered as the T cell activation (Dustin, 2006; Huppa and Davis, 2003), followed by the activation of Src kinases (Palacios and Weiss, 2004; Roskoski, 2005), intracellular calcium changes (Donnadieu et al., 1994; Randriamampita and Trautmann, 2004) and subsequent cytoskeletal remodification (Meiri, 2005; Stradal et al., 2006). The key molecules involved in this chain of events include Src family tyrosine kinase like Lck and its interaction partner SAP97 (Hanada et al., 1997; Holdorf et al., 2002), a prominent member of the family of Membrane-associated guanylate kinases (MAGUKs)

which can interact with calcium sensing proteins. Recent evidences indicate the potential role of these proteins in the maintenance and stabilisation of immunological synapses (Patel et al., 2001; Round et al., 2007; Round et al., 2005).

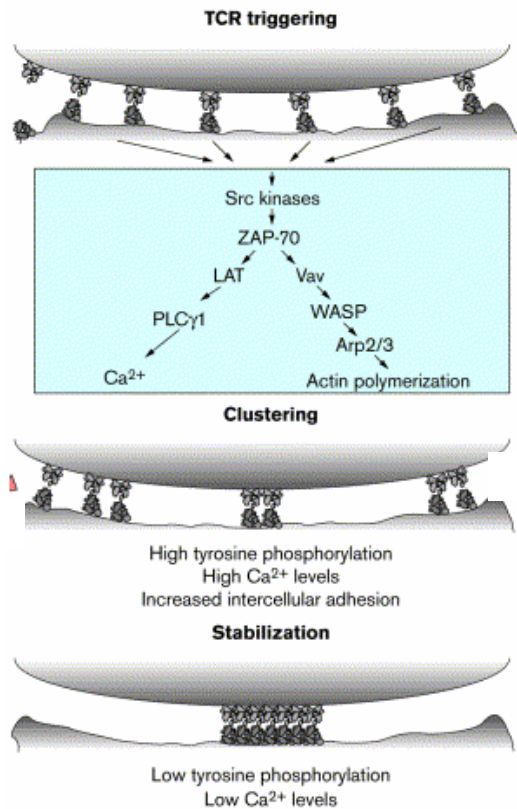


Figure 1.2 Schematic representation of different time phases of TCR: subcellular localisation and signalling. An initial period of approach of the two cells with a homogeneous distribution of TCR and peptide–MHC ligand is followed within seconds of contact by a step of TCR triggering, which results in an initiation of T cell intracellular signalling. After few minutes, receptor clustering and surface molecule redistribution is induced by the early and robust signalling resulting from this early TCR–ligand contact. When a T cell is triggered, it recruits Src Kinases which accounts for high tyrosine phosphorylation. The phosphorylation of tyrosine motifs results in elevated calcium levels and rapid cytoskeletal reorganisation. The fully mature state of the synapse is only observed after many minutes of contact when both tyrosine phosphorylation levels and calcium elevations are very low (Delon and Germain, 2000).

During T cell activation, the immunoreceptor tyrosine-based activation motif (ITAM) sequences in the TCR are phosphorylated by Src family tyrosine kinases (Horejsi et al., 2004). Lck and Fyn are spatially segregated in cell membranes, and may undergo sequential activation resulting in the phosphorylation of TCR complexes and many ITAM containing transmembrane proteins (Palacios and Weiss, 2004; Zamoyska et al., 2003). Lck is a key member involved in the formation of an immunological synapse (Dustin, 2003). Activation of Lck is thought to be regulated by the dephosphorylation of its COOH-terminal tyrosine Y505 by the activating phosphatase CD45 (Shaw et al., 1995). However, phosphopeptide-mapping experiments show that the majority of Lck in resting T cells is already dephosphorylated at Y505, and should therefore be in a partially active state. Based on these data, it has been suggested that the recruitment and not the activation of Lck may be the critical activation step (Holdorf et al., 2002). This would point to the highly dynamic structural changes which are essential for the formation of scaffolds in an immunological synapse. The enzymatic activity of Src family kinases can be further stimulated by

engagement of their SH3 domains. A proline-containing sequence in the cytoplasmic domain of CD28 can engage the SH3 domain of Lck in order to fully stimulate its kinase activity (Roskoski, 2004). This suggests that the recruitment and conformational changes of Lck at the immunological synapse may lead to the full stimulation of Lck kinase activity.

The changes in intracellular calcium levels during the formation of an immunological synapse are thought to trigger a variety of calcium-mediated processes (Randriamampita and Trautmann, 2004). The family of Membrane-associated guanylate kinases are a set of molecules which respond to the variation of intracellular calcium levels as well as cytoskeletal remodifications (Kim and Sheng, 2004; Montgomery et al., 2004). There is a growing set of evidences indicating the presence of these molecules in Hematopoietic cell lines and immunological synapses (Lue et al., 1994; Xavier et al., 2004). A proline-rich motif in the Synapse associated protein 97 (SAP97) is known to interact with the SH3 domain of Lck. It is however interesting, whether this interaction can stimulate the kinase activity of Lck similar to CD28 (Hanada et al., 1997). This would further indicate the importance of the localisation of SAP97 in the immunological synapse and its ability to be involved in calcium signalling which can further stabilise the signals, resulting in its eventual maturation.

1.6 Src kinases: structure and function

Src protein tyrosine kinases are regulatory proteins that play key roles in cell differentiation, motility, proliferation and survival (Palacios and Weiss, 2004; Zamoyska et al., 2003). These multidomain proteins contain an N-terminal 14 carbon myristoyl group, a unique segment, an SH3 domain, an SH2 domain, a protein tyrosine kinase domain and a C-terminal regulatory tail (Figure 1.3) (Roskoski, 2004).

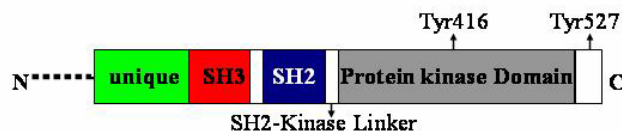


Figure 1.3) Domain organisation of the Src kinase; these domain structures are conserved throughout the other members of the family. SH domains indicate Src Homology domains. Tyr 527 indicates C-terminal tyrosine, and Ty416 is the tyrosine between the kinase domains. (Roskoski, 2004).

The chief phosphorylation sites in this family of proteins are tyrosines located between the lobes of the kinase domain (Figure 1.4 a) and at the C-terminal regulatory tail (Roskoski, 2005). X-ray crystallographic studies of the C-terminal part of the protein have shown a closed structure, where the SH3 and SH2 domains are engaged intramolecularly (Figure 1.4.a). The SH2 domain binds to the C-terminal regulatory tail of the protein, while the SH3

domain binds to the linker between the SH2 and kinase domains (Sicheri and Kuriyan, 1997; Sicheri et al., 1997). This closed conformation represents the static form of the Src family of proteins. Src kinase activity is strictly regulated since the equilibrium favours this inactive bound conformation (Figure 1.4). The inactive form of Src is destabilised by dephosphorylation of the C-terminal tyrosine residue, and by phosphorylation of an activation loop of tyrosine between the kinase domains (Xu et al., 1999; Yamaguchi and Hendrickson, 1996).

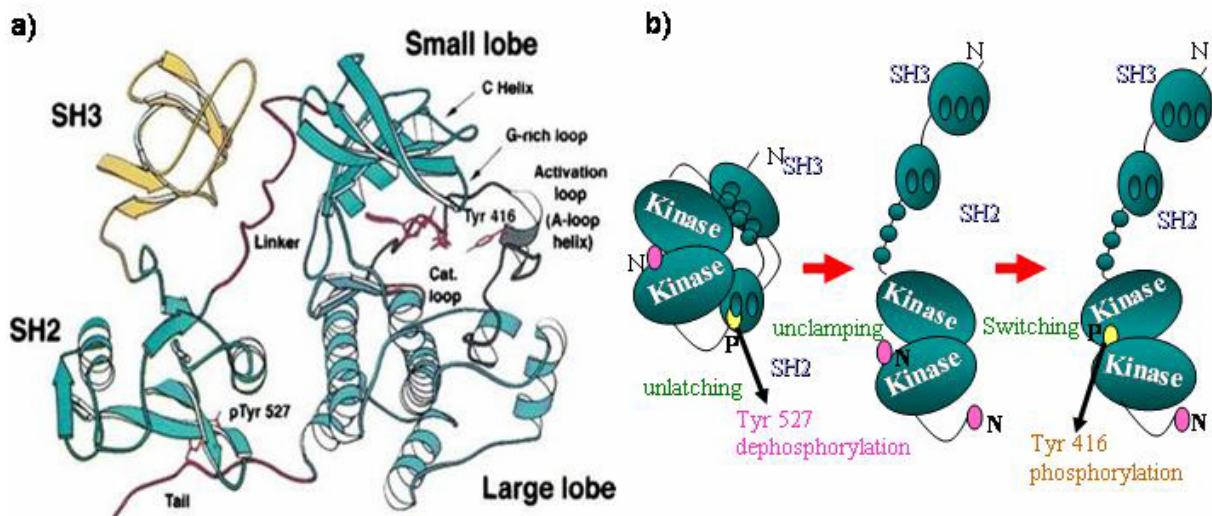


Figure 1.4) a) A ribbon diagram illustrating the C-terminal structure of human Src. A loop helix is located between the small and large lobes of the kinase, and sequesters Tyr416. SH domains denote Src Homology domains (Roskoski, 2004) b) Modes of activation for Src: unclamping, unswitching, and switching. The assembled state is unclamped by the dissociation of the C-terminal tail from the SH2 domain followed by the dephosphorylation of the exposed Tyr 527. Competing SH2 and SH3 ligands can unclamp the assembled regulatory apparatus of Src, and the kinase domain can then be switched into its active conformation by phosphorylation of a tyrosine in the activation loop. Linker phosphorylation further sets the switch in Src. N (pink) and P (yellow) denotes the nonphosphorylated and phosphorylated states of tyrosines (modified from Sicheri et al. 1997; Xu et al. 1997, Harrison 2003).

The apparatus controlling Src activation has three components which are described in the literature as the latch, clamp and the switch (Xu et al., 1999). The intramolecular interaction between the C-terminal regulatory tail of the kinase forms the latch (Figure 1.4.b). The latch, thus, stabilises the attachment of the SH2 domain to the large lobe of the kinase domain. The linker between SH2 and kinase domains contains proline residues that bind the SH3 domain to the small kinase lobes (Figure 1.4.a). This linker does not resemble classical SH3 binding consensus (P-X-X-P), but this stretch is readily folded into left-handed polyproline helix (Xu et al., 1999). The clamp is the assembly of SH2 and SH3 domains to the lobes behind the kinase domain. The clamp prevents the critical opening and closing of the conformation.

The switch is assumed to be the kinase activation loop; the activation loop can switch between the active and inactive conformations of the kinase (Figure 1.4). In the inactive state, tyrosine which occurs in the activation loop is sequestered and is not a substrate for phosphorylation by another kinase (Yamaguchi and Hendrickson, 1996). In the active conformation, phosphotyrosine at the C-terminal regulatory tail dissociates or is displaced from the SH2 binding pocket; the protein is unlatched and the clamp no longer locks the catalytic domain. The dissociation of the C-terminal tail may allow its dephosphorylation by enzymes, while the tyrosine between the kinase lobes can undergo autophosphorylation (Figure 1.4).

1.6.1 Lck

T- Lymphocyte specific protein tyrosine kinase (Lck) is among the most studied members in the family of Src kinases. Lck is one of the earliest molecules translocating to the newly formed immunological synapses (Holdorf et al., 2002), and a key molecule in several signal transduction events upon engaging T cell receptors with soluble antigens or Antigen presenting cells (Dustin, 2003; Kabouridis, 2006; Palacios and Weiss, 2004). Three-dimensional structures of SH2, SH3 and kinase domains of Lck (Eck et al., 1994; Eck et al., 1993; Yamaguchi and Hendrickson, 1996) are known. Activation requires displacement of intermolecular contacts by SH3/SH2 binding ligands, resulting in dissociation of the SH3 and SH2 domains from intramolecular interactions (Roskoski, 2004; Roskoski, 2005). In Lck, activating ligands do not induce communication between SH2 and SH3 domains. This can be attributed to the particular properties of the SH3-SH2 linker of Lck which was shown to be extremely flexible, thus effectively decoupling the SH3 and SH2 domains (Gonfloni et al., 1997). Measurements on the SH3-SH2 tandem construct of Lck have revealed a relative domain orientation, which is distinctly different from that of the SH3-SH2 crystal structure of Lck and other Src kinases (Hofmann et al., 2005). Lck (1–120 amino acids), comprising of unique and SH3 domains, has been structurally investigated by nuclear magnetic resonance spectroscopy (NMR). The unique domain, in contrast to the SH3 part, had no defined structural elements in the absence of ligands and membranes (Briese and Willbold, 2003).

Various studies have shown distinct spatial and temporal organisation of Lck in activated T cells (Holdorf et al., 2002). Lck is recruited to the interface between Antigen presenting cells and T-lymphocytes immediately after the formation of the initial contact. This is followed by the autophosphorylation of the tyrosine residue 394 (between the kinase domains), which has been shown to enhance the kinase activity of Lck (Holdorf et al., 2002).

Kinase activity of Lck has been shown to reach a peak in around 3-5 min from stimulation, which returns to the normal state in 10-20 min (Dustin, 2003; Holdorf et al., 2002).

1.7 Discs Large family of proteins and the generation of modular scaffolds

Discs Large (Dlg) family of proteins are considered pivotal in the molecular organisation of mammalian neurochemical synapses. Members of the Dlg family comprises of SAP97/hDlg, SAP90/PSD95, SAP102/NE-Dlg and PSD93/Chapsyn 110 (Fujita and Kurachi, 2000; Godreau et al., 2004; Montgomery et al., 2004). SAP97 and its human homologue of *Drosophila* protein Discs large (hDlg) are also present in epithelial cells and in Hematopoietic cells, where they are translocated to sites of cell-cell contacts (Funke et al., 2005; Lue et al., 1994). There is increasing evidence that Dlg family of proteins can play important roles in the formation and maintenance of immunological synapses (Round et al., 2005; Xavier et al., 2004). Five members of the Src kinase family (Lck, YES, LYN, FYN and Src) are known to interact with Dlg family proteins (Kalia and Salter, 2003; Tezuka et al., 1999). The recruitment of these proteins to the immunological synapses may be functionally relevant because of their interaction with the Src family kinases, thus orchestrating multiple signalling pathways similar to neuronal synapses (Kim and Sheng, 2004). YES, LYN, FYN and Src interact with SAP90/PSD95, and Lck is known to associate with SAP97/hDlg (Hanada et al., 1997; Kalia and Salter, 2003).

Dlg family of proteins are widely referred as MAGUKs (Membrane-associated guanylate kinases), and are composed of multiple protein-protein interaction domains i.e. three PDZ (PSD95/DLG/ZO1) domains, a Src homology 3 domain and a guanylate kinase domain. Best characterised is the PDZ domain, which binds with high affinity to the carboxyl terminal peptide motifs in a number of proteins, notably NR2 units of the NMDA receptor and the voltage gated inwardly rectifying K⁺ channels (Garner et al., 2000; Kim and Sheng, 2004). The guanylate kinase like (GUK) domain of the MAGUKs lacks key amino acid residues required for ATP/GMP binding, and it is assumed that instead of an enzymatic role it may have been modified for protein-protein interactions (McGee et al., 2001). Accordingly, a number of interactions have been mapped to this region including GKAP and SPAR (Kim and Sheng, 2004; Wu et al., 2000).

MAGUKs are modular scaffolds that organise signalling complexes at synapses and other cell junctions (El-Husseini et al., 2000; Hanada et al., 2000; Kim and Sheng, 2004). It has been shown that the SH3 domain of MAGUKs has a typical binding specificity to the GUK domain (Wu et al., 2000). The classical proline-rich SH3 binding (P-X-X-P) motifs are

absent from the GUK domain. A flexible linker known as the HOOK region separates the SH3 and GUK domains (Figure 1.5). The crystallographic structure of the SH3-HOOK-GUK unit, which is conserved in MAGUKs, shows a parallel arrangement of SH3 and GUK domain (Figure 1.5), which indicate the probability of a physical association between these domains (McGee et al., 2001). Although SH3 binding can occur in an intramolecular or intermolecular manner, it is assumed that the intramolecular mode is preferred. It is thus thought that the intramolecular interaction mode is supported by additional tertiary interactions when these domains are adjacent in the same polypeptide (McGee et al., 2001).

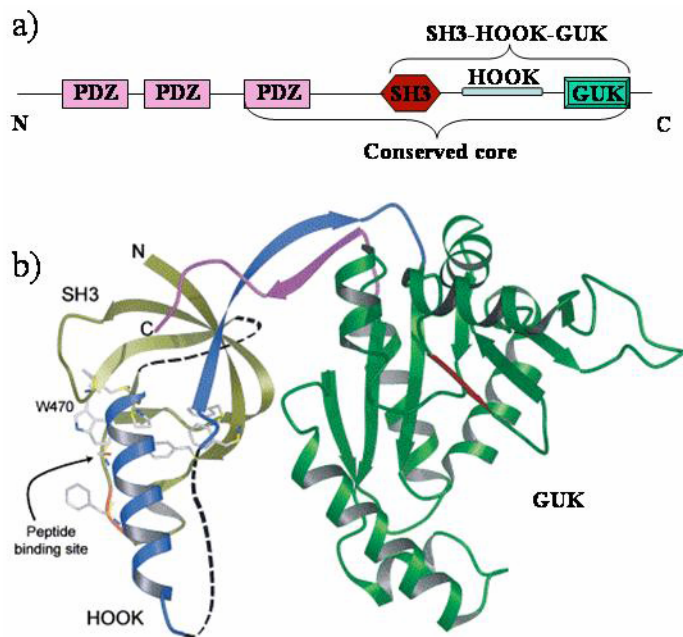


Figure 1.5) SAP domain organisation and overall architecture of SAP90/PSD-95 SH3-HOOK-GUK units, GK indicate the GUK domain (a) SAP domain organisation showing the conserved core of MAGUK proteins (SH3-HOOK-GUK). (b) SH3-HOOK-GUK model built using the GMP-bound structure and residues 439–445 and 502–508 from the apo form. The SH3 and HOOK domains are shown in gold and blue, respectively. GUK domain is depicted in green, and in magenta are the last 12 residues C-terminal to the GUK domain. The dashed lines represent the disordered parts of the molecule in both crystal forms. The residues represented in the SH3 domain constitute the proline-rich peptide binding site. The regions in the SH3 and GUK domains that participate in crystallographic contacts in both crystal forms are shown in red (reproduced from Tavarez et al, 2001).

1.7.1 SAP97/hDlg

SAP97/hDlg is a key member of the family of Dlg family of proteins, which is involved in the membrane scaffolds and activity-dependent changes in cell morphology (Lue et al., 1994). Several isoforms have been described (Figure 1.6), which may contribute to the differential expression and targeting of this protein to different subcellular regions (McLaughlin et al., 2002). An alternatively spliced proline-rich insertion called I1 is located between the N-terminal region of SAP97/hDlg and the first PDZ domain (Figure 1.6). The HOOK region, which could be highly flexible, has been characterised to contain two alternatively spliced insertions, I2 and I3 (McLaughlin et al., 2002; Wu et al., 2000). In the same region, a third alternatively spliced insertion has been described as a brain isoform of SAP97/hDlg. The region separating the insertion sites of I2/I3 and I4 is also alternatively spliced, and according to the nomenclature is known as I5 (McLaughlin et al., 2002).

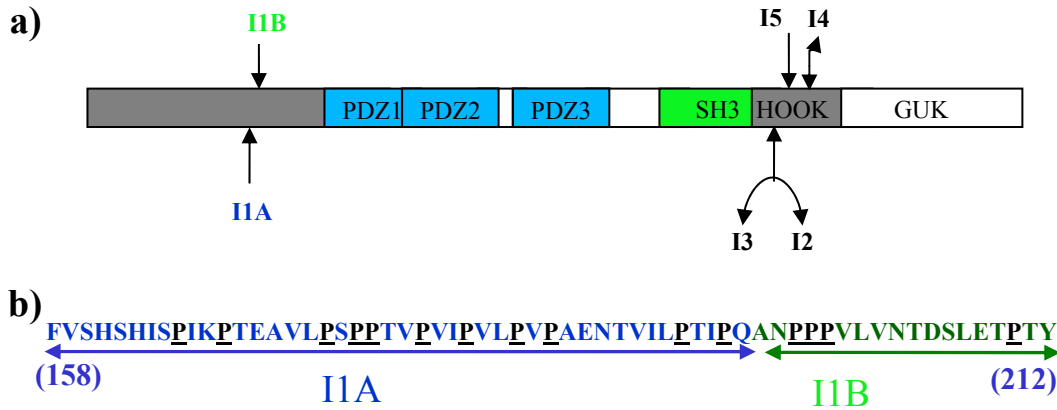


Figure 1.6) a) Diagram of hDlg coding sequence. hDlg contains three well characterised types of domains: the PDZ repeats (PDZ 1 to 3), an SH3 domain (SH3), and a domain homologous to the yeast guanylate kinase (GUK). The two regions of hDlg represented by grey boxes contain alternatively spliced exons I1A, I1B, I2, I3, I4, and I5. b) Identity of insertions I1A and I1B. I1A and I1B insertions form the proline-rich region in the N-terminal portion of hDlg. The boundaries of both insertions are bracketed above the protein sequence derived from the human tissue. I1A and I1B together will be denoted as I1. For this work, the fusion proteins containing combinations of I1 and I3 splicing (referred as I1-I3 SAP97/hDlg), I1 and I2 splicing (referred as I1-I2 SAP97/hDlg) and I3 alone (referred as I3-SAP97/hDlg) will be used.

The alternatively spliced insertion I3 is the only isoform, whose function has been investigated in detail (Rumbaugh et al., 2003). I3 and PDZ 1-2 regions of SAP97/hDlg show similar charged residues, both forming binding sites for 4.1-like proteins (Wu et al., 2000). These sites contribute to the hDlg localisation at sites of cell-cell contact. I3 is also known to be responsible for the localisation of the protein to the plasma membrane (Hanada et al., 2003; Rumbaugh et al., 2003). I2 is reported to be responsible for targeting hDlg to the nucleus (McLaughlin et al., 2002), though contradictory results have been documented (Hanada et al., 2003; Thomas et al., 2000). Interestingly, the majority of splicing has been reported to occur in the region between SH3 and GUK domains, highlighting its importance in scaffolding and signalling mechanisms (Figure 1.6). To date, I1 is the only known splicing outside the HOOK region. Two proline-rich alternatively spliced insertions, I1A and I1B, are predicted to form an extended helical domain comprising of two polyproline II helices at the N-terminal portion of SAP97/hDlg. This structural prediction based on the (P-X-X-P) consensus, together with the general hydrophobic character of the sequence supports the hypothesis that I1A and IB insertions maybe two SH3 binding sites (McLaughlin et al., 2002).

1.8 Aims

The ultimate aim of my PhD work was to achieve deeper insights into the roles of Lck and SAP97 in synaptic stabilisation. The subcellular distributions as well as conformational changes of these multidomain proteins have been found to be highly relevant in this context, as discussed in the previous sections. Therefore, tracking the real-time recruitment and

conformational changes of these proteins in living cells would in turn be the most suitable approach for addressing this issue.

The changes in macromolecules including their conformational changes, association, and dissociation of protein domains are below the limit of optical resolution to be tracked by conventional microscopy methods. It was thus important to rely on spectroscopic methods which provide resolution of the order of dimensions of macromolecules (1-10 nm). X-ray crystallography and Nuclear Magnetic Resonance (NMR) spectroscopy are widely used methods to study these changes at molecular and submolecular level. However, these powerful methods can neither be used to track real-time conformational changes nor for applications in living cells (Wu and Brand, 1994). Therefore, advanced imaging techniques including Fluorescence Lifetime Imaging Microscopy (FLIM) and Foersters/Fluorescence Resonance Energy Transfer (FRET) (Jares-Erijman and Jovin, 2003) were adopted for the purpose. A combination of these techniques allowed to study the submolecular changes in proteins at the nanometer scale at picosecond resolution in living cells.

The sensitivity of the present approach for monitoring subtle changes in macromolecular conformations was addressed using a chimeric construct, Clomeleon (Kuner and Augustine, 2000), comprising of GFP variants Cyan Fluorescent Protein (CFP) and Topaz (a variant of Yellow Fluorescent Protein / YFP), separated by an amino acid linker. The linker size was varied in steps of 8 amino acids to generate different tandem size variants of Clomeleon. The efficiency of energy transfer was compared between the different constructs. New approaches of simultaneous donor–acceptor detection and analysis of fluorescence decays, together with the study of the change of pre-exponential factors of individual lifetimes were utilised to address the foresaid aim.

1.8.1 Real-time conformational changes of Lck

The C-terminal part of Lck is assumed to form a compact regulatory structure, keeping it in an inactive form. It has been proposed that the presence of its unique domain is not relevant to the three-dimensional structure of the Lck, thus having no major role in the folding of the C-terminal part of the protein (Briese and Willbold, 2003). Eventhough there are several structural studies which have highlighted the differences and similarities of Lck with other Src kinases (Mendieta and Gago, 2004; Sicheri and Kuriyan, 1997), to date, no studies have addressed the folding of full-length Lck in living cells. This would be important, considering the enormous number of cell signalling pathways in which the Lck is involved (Palacios and Weiss, 2004; Zamoyska et al., 2003).

To date, structural studies have been done only on the inactive conformation of the Src kinase family of proteins. Biochemical reports suggest a conformational change for the protein in the active form (Roskoski, 2004; Roskoski, 2005). Eventhough this hypothesis has not been verified in vivo, it remains a potential mechanism regarding the response of these proteins to a stimulus. So far, there has been no confirmation for the hypothesis that the kinase activity is directly related to the open conformation of the protein (Holdorf et al., 2002). The current theories indicate four possible states for the regulatory tyrosines in the family of Src tyrosine kinases (Roskoski, 2004)

- a) nonphosphorylated
- b) Phosphorylation of the C-terminal tyrosine
- c) Phosphorylation of the tyrosine in the activation loop between the kinase domains
- d) Phosphorylation of both C-terminal tyrosine and the tyrosine in the activation loop

So far, only the structure of the C-terminal tyrosine phosphorylated form has been determined. The doubly phosphorylated enzyme is active; and it is assumed that the phosphorylation of the tyrosine in the activation loop may override C-terminal phosphorylation (Figure 1.4.b). The key structure where the tyrosine in the activation loop between the kinase domains alone is phosphorylated can only be reconstituted in natural conditions; thus the enzyme activity or structural data is not yet known.

Therefore, it was essential to study the structure of Src kinases in resting and stimulated T cells to achieve deeper insights into their structural regulation at different phases of cellular activity. In this work, differences in intramolecular FRET between CFP-YFP tagged molecules were used to investigate the folding of full-length Lck molecule in resting T-lymphocytes. The temporal changes in the structure of Lck were addressed using FRET. The spatial and temporal differences of FRET in real-time was investigated by presenting T-lymphocytes with soluble antibodies and Antigen presenting cells. The changes in intramolecular FRET were addressed by tagging the constructs with suitable GFP variants as donor-acceptor pairs.

1.8.2 Calicum-dependent conformational changes of SAP97 and PSD95

In MAGUKs like SAP97/hDlg and SAP90/PSD95, the SH3 and GUK domains form an integrated unit (McGee and Bredt, 1999; McGee et al., 2001; Shin et al., 2000; Wu et al., 2000). This C-terminal part is conserved in different MAGUKs, and the regulation of its intramolecular interactions may underlie a principal mechanism involved in the formation of membrane scaffolds. The crystal structure suggests that SH3 and GUK domains are arranged in parallel, and the HOOK region function as a linker separating these well formed domains

(McGee et al., 2001) (Figure 1.5). A model for oligomerisation of MAGUKs has been proposed, in which SH3 and GUK domains regulate their association by swapping these domains from an intra to an intermolecular association (McGee et al., 2001). This domain swapping may be relevant since it is dependent on the association of the ligands with the HOOK region, effectively decoupling the intramolecular involvement of SH3 and GUK domains. This model, though untested, provides a possible mechanism for ligand regulation of oligomerisation (McGee et al., 2001).

This model offers potential advantages as a scaffolding mechanism:

- a) Formation of intra or intermolecular association between SH3 and GUK domains facilitates oligomerisation without occluding sites on these domains that may associate to signalling proteins.
- b) Regulatory proteins with appropriate subcellular localisation could direct the correct temporal and spatial assembly of the interlocked MAGUK networks.
- c) Heterodimeric complexes of MAGUKs, directed by sets of regulatory proteins, could provide combinatorial scaffold diversity, which may specify differential protein recruitment.

This model is not verified to date, but goes along with the current observation of various functions of MAGUKs, and is among the potential mechanisms that participate in the assembly of supramolecular signaling complexes at cell junctions. In addition, previous works have shown that Calmodulin binds to the HOOK region of SAP97 and of SAP102 in a calcium-dependent manner (Masuko et al., 1999; Paarmann et al., 2002). It has been suggested that this binding could be a key mechanism responsible for opening of the conformation and enabling the intermolecular interaction between different MAGUKS. This clustering between MAGUKs is significant, since it can organise a rigid cytoplasmic scaffold spontaneously in response to a calcium signal (McGee et al., 2001; Montgomery et al., 2004). Thus, the calcium-dependent conformational changes of the SH3-HOOK-GUK unit of SAP97/hDlg and SAP90/PDS95 would be an interesting area of investigation.

In the current study, the calcium-dependent structural changes of MAGUKs were investigated using FRET-FLIM studies. The differences in intramolecular FRET of SAP97/hDlg and SAP90/PSD95 molecules were probed before and after the elevation of intracellular calcium levels. These changes in intramolecular FRET were used to understand how the SH3-HOOK-GUK modules of these proteins are regulated, and how the assembly and disassembly of these intramolecular interactions can facilitate stable near-membrane

scaffolds. These changes would be vital in understanding the scaffolding roles of MAGUKs in various cell-adhesion mechanisms, like the immunological synapse.

1.8.3 Role of Lck-SAP97 association in synaptic stabilisation

Biochemical data have suggested an interaction between SAP97/hDlg and the SH3 domain containing protein tyrosine kinase Lck in T-lymphocytes (Hanada et al., 1997; McLaughlin et al., 2002). It has been shown that Lck is recruited to immunological synapses after the initial cell recognition events (Holdorf et al., 2002). SAP97 is also shown to translocate to the immunological synapse (Xavier et al., 2004), cell-cell junctions (Hanada et al., 2003), and is known to influence transsynaptic signalling in neurons (Regalado et al., 2006). The proline-rich region of SAP97 has been biochemically shown to associate with Lck, implying the relevance of this interaction in possible organisation of near-membrane scaffolds (Hanada et al., 1997) at immunological synapses. Recent observations indicate the involvement of a multiprotein complex comprising of Lck and SAP97/hDlg, deciding the polarity and organisation of T cells in response to antigen presentation (Round et al., 2007; Round et al., 2005). The interaction between Dlg family proteins and Src family kinases could serve as a potential mechanism in the formation of MAGUK mediated transient scaffolds.

Therefore, it was essential to understand the localisation of SAP97/hDlg in the immunological synapse. SAP97/hDlg is known to have various spliced insertions (Lue et al., 1994; McLaughlin et al., 2002), and the role of such a proline-rich splicing at the N-terminus is thought to be critical in deciding the localisation of the protein. This role was investigated in detail with respect to the localisation of the protein in immunological synapses. The differential activity-dependent distribution of combination of multiple isoforms of SAP97/hDlg in T-lymphocytes was addressed using T cell-bead interfaces, mocking the formation of an immunological synapse. The influence of Lck on the translocation of SAP97/hDlg was investigated by comparing the recruitment of this protein in wild type and Lck deficient T cell lines.

Multidomain proteins like Lck and SAP97/hDlg are vital to the formation and stabilisation of transient scaffolds at immunological synapse. Here, advanced imaging techniques were used to provide insights into the localisation of these proteins and conformational changes associated with it. Understanding these mechanisms would significantly elevate the existing knowledge on the dynamic molecular organisation at the immunological synapse.

2 THEORETICAL FOUNDATIONS AND INSTRUMENTATION

2.1 Fluorescence of organic molecules

The important feature of the application of spectroscopy to biochemical problems is the ability to quantitatively assess and characterise the individual components in the mixture. Spectroscopic methods in recent times have been adapted to address the complex characterisation of the macromolecular association, conformations and complex environmental changes in the natural environment (Jares-Erijman and Jovin, 2003; Lippincott-Schwartz and Patterson, 2003). Fluorescence is the most common form of spectroscopy, which has aided biochemists to decipher the nature of different macromolecules in solutions and in living cells. Identical chromophores often exhibit spectral differences due to heterogeneity in their microenvironment. The best studied examples are the proteins containing multiple tryptophan residues (like immunophilin), where the environmental heterogeneity affects each tryptophan differently (Lakowicz, 1999).

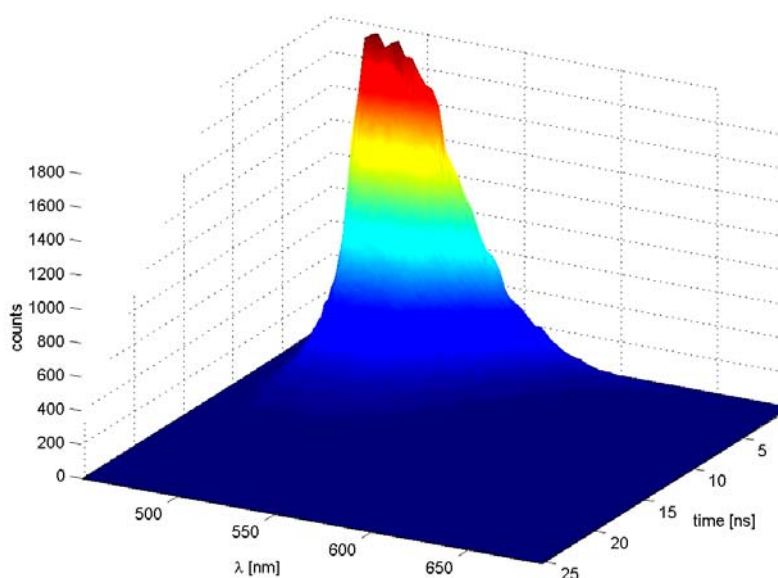


Figure 2.1) An example for a three dimensional emission contour of a fluorophore. Fluorescence emission is a function of wavelength (λ) and time. Statistical acquisition of emitted photons after a series of excitation flashes gives fluorescence decays along the wavelengths.

Fluorescence of organic molecules is characterised not only by their unique absorption or emission spectra (Figure 2.1), but also by signatory fluorescence decay times dependent on the immediate microenvironment (Lakowicz, 1999). Information from fluorescence decay times has been used to study the environmental heterogeneity in living cells (Lakowicz et al., 1992b; Lakowicz et al., 1992c). These studies showed that fluorescence decay times could be affected by subcellular changes in pH and ions. The foresaid technique which generates a lifetime map of a single chromophore on the cell-surface is broadly categorised as Fluorescence Lifetime Imaging Microscopy (FLIM) (Lakowicz et al., 1992a). FLIM provides

a qualitative assessment of intracellular environment but does not provide the needed distance information at the molecular scale in which macromolecules associate. Foersters/Fluorescence Resonance Energy Transfer (FRET) is widely used in studies of bimolecular structure and dynamics (Clegg, 1996; dos Remedios and Moens, 1995; Wu and Brand, 1994). Adapting FLIM to study FRET provides information on distances about 1-10 nm and is thus suitable to investigate spatial relationships of interest in biochemistry.

In cells, each subcellular compartment has a characteristic microenvironment which affects the covalently attached dyes and coupled fusion proteins differently (dos Remedios and Moens, 1995; Niggli and Egger, 2004; Wu and Brand, 1994). The results obtained have to be distinguished between the intrinsic effects expected of the chromophores or mere environmental heterogeneity (Knutson et al., 1982; Lakowicz et al., 1992b). The best example is the analysis of fluorescence decays of a chromophore in cells. The environmental heterogeneity (local changes in pH and ions, autofluorescence occurring from cellular metabolism, excited state reactions) can affect the fluorescence decay of the molecule. These different effects must be discriminated from the intrinsic behaviour of the fluorescing molecule to comprehend its photophysical behaviour in varying microenvironments.

Nanosecond spectral shifts may have their origin in ground state heterogeneity or microheterogeneity, which is revealed only in the emission of excited state (Knutson et al., 1982). In addition, spectral shifts may reflect excited state reactions, which occur on a nanosecond time scale. Advances in the instrumentation and analysis have enabled to obtain nanosecond Time Resolved Emission Spectra (TRES) and Decay Associated Spectra (DAS) to address these complex photophysical properties of the fluorophores involved (Davenport et al., 1986; Knutson et al., 1982). TRES represent fluorescence emission spectra obtained during discrete time intervals throughout fluorescence decay, while DAS represent the spectral distribution of individual emitting species that contributes to the total fluorescence. DAS are thus derived spectra, uniquely linked to decay functions. A plain explanation of DAS would be the spectra, the mixture will display, if one could somehow exclude all except one emitting species at a time. If this information is available regarding the nature of complex decay behaviour, the dimension of time can be utilised to qualitatively and quantitatively characterise the subcellular environmental heterogeneity that cannot be analysed by spectral resolution alone. This is achieved by identifying different decay functions uniquely associated with a species and then extracting the spectra associated with each decay time. These methods were successfully used to investigate the difference in microenvironments of tryptophan and tyrosine residues in proteins discriminating sources of individual heterogeneity in biochemical

samples (Beechem and Brand, 1986; Knutson et al., 1982). These methods have also been used to distinguish the heterogeneous fluorescence in binary systems (Lakowicz, 1999). However, the applications of these to assess macromolecular association directly from living cells were limited. With recent advances in Time correlated single photon counting and combination with microscopy, it is possible to obtain DAS from unperturbed biological systems. The theoretical background and instrumentation with which DAS was obtained and its implications to study macromolecular dynamics without disturbing the living state of the biological system is presented in the following sections.

2.2 Theory of spectral separation

Fluorescence emission intensity is a function of both wavelength (inverse of energy) and time after exciting the molecule (Figure 2.1). For a homogeneously emitting population, this total intensity can be separated into the product of a wavelength distribution ($\alpha(\lambda)$) with a time distribution ($d(t)$):

$$f(\lambda, t) = \alpha(\lambda)d(t) \quad (1)$$

The separation of variables is justified only for homogeneous components. Intrinsic heterogeneity in the excited state or ground state may result in similar spectra but different lifetimes in the intensity decay. In a heterogeneous system, where there is a mixture of fluorophores or the presence of excited state reactions, spectral shapes may be time dependent and intensity decays will be wavelength dependent, which will also be discussed. Normally, chromophores which are used for FLIM, the decay coefficient is a constant whose inverse is the lifetime τ of the excited state (Jares-Erijman and Jovin, 2003).

$$f(\lambda, t) = \alpha(\lambda)e^{-t/\tau} \quad (2)$$

In these fluorophores exponential decays are the most frequent, so with respect to *equation (1)*

$$d(t) = e^{-t/\tau} \quad (3)$$

Separation of Decay Associated Spectra does not depend on the functional shape of $d(t)$. This method can be extended to study multiexponential decays. A simple example of a multiexponential system will be a binary mixture of fluorophores leading to a time varying spectrum and wavelength dependent decay.

$$f(\lambda, t) = \alpha_1(\lambda)e^{-t/\tau_1} + \alpha_2(\lambda)e^{-t/\tau_2} = \sum_{i=1}^2 \alpha_i(\lambda)e^{-t/\tau_i} \quad (4)$$

The theoretical decay functions are known as impulse responses, i.e. the decay of intensity that follows an instantaneous excitation. This excitation is considered to be as short as possible and assumes the shape of a Diracs Delta function in the ideal case. But in practice the pulses used for pulse fluorimetry and lifetime measurements have an effective width, ranging from picoseconds to nanoseconds, measured as full width at half maximum (FWHM). Thus, the decay of intensity following an experimental excitation is more complex. The lamp function used for excitation can be divided into infinitesimally small pulses, each of which is assumed to generate a decay response. The sum of all of these responses results in the observed decay function “ $D(t)$ ”. At the limit of the continuous division, for assumed infinitesimally small pulses, is the modification of the impulse decay “ $d(t)$ ” by the lamp function “ $L(t)$ ”. This process of involvement of the excitation pulse in the experimental decay is called Convolution (Figure 2.2).

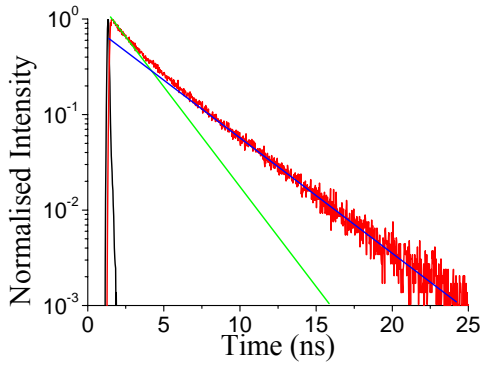


Figure 2.2) Procedure to determine the lifetimes from the observed decay (red) and the instrument response function/Lamp function (black). The components giving rise to the green and blue curves are convolved together by the lamp function resulting in an observed decay function. This can be re-identified by deconvolving the effect of the lamp function on the observed decay resulting in the correct values of green and blue curves.

$$D(t') = \int_0^{t'} L(t) d(t'-t) dt \quad (5)$$

Thus in the single exponential case, observed fluorescence “ F_{obsd} ” is function of wavelength dependent term and experimental decay function

$$F_{obsd}(\lambda, t') = \alpha(\lambda) \int_0^{t'} L(t) e^{-(t-t')/\tau} dt = \alpha(\lambda) D(t') \quad (6)$$

Interestingly the spectral features $\alpha(\lambda)$, the wavelength dependent term, is unaffected by convolution. Convolution acts on the decay function only. In case of heterogeneous samples the fluorescence “ F ” is

$$F(\lambda, t') = \sum_I \alpha_i(\lambda) \int_0^{t'} L(t) e^{-(t-t')/\tau_i} dt = \sum_i \alpha_i(\lambda) D_i(t') \quad (7)$$

At any time t' on the instrumental observation scale, the emission is a mixture of constituent emission spectra $\alpha_i(\lambda)$ with mixing co-efficient $D_i(t')$. If it is possible to observe the decays in a small wavelength slice, the time constituents in the convoluted impulse decay function can be obtained back by deconvolution of the obtained intensity decays by the lamp function. The deconvolution can be used to obtain the multiexponential terms comprising the impulse decay and contribution of these different lifetimes can be obtained at a specified wavelength. As described in *equations (2) and (4)*, the contribution of multiple lifetimes are wavelength dependent. It is assumed that the lifetime is a global quantity and in normal cases unaffected by the detection wavelength (Lakowicz, 1999). Simultaneous detection of intensity decays along the wavelength and subsequent deconvolution of these intensity decays result in the spectral contribution of a lifetime. This spectral contribution of lifetimes is known as the Decay Associated Spectrum (DAS). Thus DAS is an associative quantity, which sums up the spectral and lifetime information of fluorophores. This will be sufficient to describe the photophysical characteristics of the observed ensemble. In simple mathematical terms DAS for a decay constant k_i can be defined by

$$f(\lambda, t) = \sum DAS(\lambda, k_i) \exp(-k_i t) = \sum f_i(\lambda, t) \quad (8)$$

Where, $f(\lambda, t)$ is the total fluorescence intensity at wavelength λ at time t after excitation with an infinitesimally small pulse and $f_i(\lambda, t)$ is the intensity of the species i . k_i is the decay rate defined as $(\tau_i)^{-1}$ from *equations (2) and (4)*. The different excited state spectra is obtained as

$$\frac{\int_0^{\infty} f_i(\lambda, k_i) dt}{\int_0^{\infty} f(\lambda, k) dt} = \frac{DAS(\lambda, k_i) / K_i}{\sum DAS(\lambda, k_i) / K_i} \quad (9)$$

Equation (9) summarises the fluorescence dynamics of the system, if it is of ground state heterogeneity type or when the excited state reactions are extremely slow. This method is of prime importance when examining the biochemical fluorescence from living systems. The currently used fluorophores for live cell applications have high quantum yield to distinguish these interactions over the weak time resolved fluorescence noise generated by the living samples. This may not be sufficient to study the changes in intensity decays collected from a single wavelength slice in living cells since the technique of detection and analysis in these systems is based on pure signal to noise ratio of the probed molecules to the time

correlated noise (e.g. cellular autofluorescence resulting from metabolism). This level may vary from cell to cell because of the metabolic and developmental stages of the cells or purely from the environmental variation in different organelles, which provide differences in spectrum, and lifetimes, which is a common source to misinterpret the data. DAS, in contrary, provides the needed spectral information, to discriminate this mere heterogeneity. It can be used to understand whether the origin of fluorescence is the same fluorophore or different since DAS from a single fluorophore may follow identical spectral distribution. This is however significant since most of the probes used for biological applications tend to produce multiexponential decays. It is important to understand the origin of these decays to characterise the fluorophores during its association with a specific intracellular compartment achieved by genetic targeting. However, the foresaid equation to evaluate DAS breaks down in the presence of fast excited state reaction like energy transfer or charge transfer.

2.3 Fast excited state reactions

An excited state reaction generally means a molecular process, which changes the structure of the fluorophore, and which occurs subsequent to excitation. Such reactions are frequent in nature when the light absorption generally changes the electron distribution within a fluorophore, which in turn changes its chemical or physical properties. There are several phenomena, which are characterised as excited state reactions. These processes include proton and electron transfer, Foersters / Fluorescence resonance energy transfer, solvent relaxation, excimer and exciplex formation (Lakowicz, 1999). Theoretical framework for two state models could be used to understand the majority of excited state reactions studied using biochemical samples. A simple two state model is shown in (Figure 2.3).

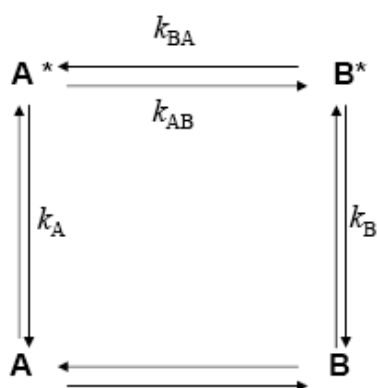


Figure 2.3) Kinetic scheme for reversible excited state reaction for two species A and B. The rate constants are explained in text. A* and B* are excited states of the two species.

‘A’ and ‘B’ refer to the ground states of two molecules A and B. Excited states of each of these molecules are denoted as ‘A*’ and ‘B*’. A* can relax back to the ground state by fluorescence (k_{FA}) or by quenching, which are designated by the combined rate constant k_A .

A* can also be involved in an excited state reaction populating the excited state of B denoted as B* with a rate constant k_{AB} . The excited molecule B* can fluoresce with a rate constant k_{FB} or undergo nonradiative conversion to B which will be indicated as the combined rate constant k_B , or it can however loose energy and be converted back to A* as indicated by the bimolecular rate constant k_{BA} .

The differential rate equations for the decay of A* and B* are indicated by the following equations

$$\begin{aligned} -d(A^*)/dt &= (k_A + k_{AB})[A^*] - k_{BA}[B^*] \\ -d(B^*)/dt &= (k_B + k_{BA})[B^*] - k_{AB}[A^*] \end{aligned} \quad (10)$$

The initial conditions are such that only A is directly excited, that is $[A^*] = [A_0^*]$ and $[B^*] = 0$, at $t=0$, yielding the fluorescence decay for A and B (I_A and I_B) at wavelength λ

$$\begin{aligned} I_A(\lambda, t) &= \alpha_1(\lambda)e^{-t/\tau_1} + \alpha_2(\lambda)e^{-t/\tau_2} \\ I_B(\lambda, t) &= \beta_1(\lambda)e^{-t/\tau_1} + \beta_2(\lambda)e^{-t/\tau_2} \end{aligned} \quad (11)$$

The decay times and amplitudes are related to the rate constants indicated in Figure 2.3 and *equation (11)* as shown in the equation below (Davenport et al., 1986).

$$\begin{aligned} \gamma_1, \gamma_2 &= \tau_1^{-1}, \tau_2^{-1} = 1/2 \left\{ (X + Y) \pm \left((Y - X)^2 + 4k_{BA}k_{AB} \right)^{1/2} \right\} \\ \alpha_1(\lambda) &= C_A \lambda [A_0^*] (X - \gamma_2) / (\gamma_1 - \gamma_2) \\ \alpha_2(\lambda) &= C_A \lambda [A_0^*] (\gamma_1 - X) / (\gamma_1 - \gamma_2) \\ -\beta_1(\lambda) &= \beta_2(\lambda) = \beta(\lambda) = C_B(\lambda) k_{AB} [A_0^*] k_{FB} / (\gamma_1 - \gamma_2) \end{aligned} \quad (12)$$

Where $X = k_A + k_{BA}$ and $Y = k_B + k_{AB}$, while $C_A(\lambda)$ and $C_B(\lambda)$ are spectral emission contours normalised to unit area of the species, respectively. k_{FB} is the rate constant of B* relaxing back to the ground state B. The multiple decay times present in these intensity decays are the same for both species and the amplitudes describing the decay of B* are identical in magnitude but opposite in sign. This change of sign in the amplitude of the B* species is the characteristics or proof of an energy transfer. This change in sign provides the most important parameter in time domain spectroscopic measurements, which describes the excited state reaction. Thus, *equation (11)* may be modified as

$$\begin{aligned} I_A(\lambda, t) &= \alpha_1(\lambda)e^{-t/\tau_1} + \alpha_2(\lambda)e^{-t/\tau_2} \\ I_B(\lambda, t) &= \beta_1(\lambda)e^{-t/\tau_1} - \beta_2(\lambda)e^{-t/\tau_2} \end{aligned} \quad (13)$$

Where $-\beta_1(\lambda) = \beta_2(\lambda) = \beta(\lambda)$. Thus for a two state system, deconvolution of intensity decays in the donor and intensity emission regions will provide identical lifetimes. If at the acceptor emission there is no emission from the donor, the amplitudes will be equal and opposite in sign indicating the rate at which B* is being populated by A*. Nevertheless, in the case of many excited state reactions the emission spectra of the donor and acceptor states are overlapping even though their emission peaks are well separated. In that case, the intensity decays obtained at a specific wavelength can be explained as a sum of *equations (13)*

$$I(\lambda, t) = (\alpha_1 + \beta_1)(\lambda)e^{-t/\tau_1} + (\alpha_2 - \beta_2)(\lambda)e^{-t/\tau_2} \quad (14)$$

Thus, the deconvolution of intensity decays along the wavelength channels will result in an increase, in one component $(\alpha_1 + \beta_1)$, along the wavelength with a maximum at the acceptor emission peak and the other component $(\alpha_2 - \beta_2)$ will show a negative contribution in the emission peak of the acceptor depending on the overlap of the donor emission spectrum with that of acceptor. If the contribution of the donor is less than that of the acceptor the term $(\alpha_2 - \beta_2)$ will always be negative. This negativity of the contribution even with overlapping emission spectra can be defined as a proof of energy transfer. Since Foerster's resonance energy transfer reaction is a special case of excited state reaction with no or minimal back reaction from B* species the *equation (14)* simplifies and it is much easier to understand the negativity of the contribution at the acceptor peak. Thus, in contrast to slow excited state reaction or ground state heterogeneity, DAS of a fast-excited state reaction will not be identical through out the spectrum. The multiexponential term related to an increase in population of acceptor excited state directly from donor will be different from the other components, indicating its involvement in energy transfer.

2.4 FRET

FRET is a fast excited state reaction, in which energy is transferred nonradiatively (via long-range dipole-dipole coupling) from a fluorophore in an electronic excited state serving as a donor, to another chromophore termed as acceptor (Gadella, 1999; Jares-Erijman and Jovin, 2003; Sekar and Periasamy, 2003; Tramier et al., 2003; Wouters and Bastiaens, 1999). The latter may, but need not be fluorescent. The fluorophore can relax back to the ground state radiatively with a rate k_f and nonradiatively k_{nr} . The lifetime of such a process can be explained as a reciprocal of the total rate involved in relaxation

$$\tau_0 = (k_d)^{-1} = (k_f + k_{nr})^{-1} \quad (15)$$

When involved in energy transfer the rate at which energy is transferred from donor to acceptor k_t varies inversely as the sixth power of the separation between involved fluorophores (Jares-Erijman and Jovin, 2003). Such distances are relevant for most biological molecules or their constituent domains engaged in a complex formations and conformational transitions. Additionally the transfer rate depends on three parameters 1) The overlap of donor emission and acceptor absorption spectrum (overlap integral), 2) Relative orientation of the donor absorption and acceptor transition dipole moments (κ^2), 3) The refractive index (n^4 , normal range 1/3-1/5)

The quantitative treatment of FRET originated with Theodore Foerster and is embodied in formulas for k_t , the Foerster constant/radius R_0 , and the transfer quantum yield generally discussed as energy transfer efficiency (E) (Jares-Erijman and Jovin, 2003).

$$k_t = \frac{1}{\tau_0} (R_0 / R)^6 \quad (16)$$

$$R_0^6 = C_0 \kappa^2 J n^{-4} Q_0 = C_0 \kappa^2 J n^{-4} k_t \tau_0 \quad (17)$$

$$E = k_t \tau = \frac{(R_0 / R)^6}{1 + (R_0 / R)^6} \quad (18)$$

$$\tau_0^{-1} = k_f + k_{nr}; \tau^{-1} = \tau_0^{-1} + k_t \quad (19)$$

Where, $C_0 = 8.8 \times 10^{-28}$ for R_0 in nm and $J = 10^{17} \int q_{d,\lambda} \epsilon_{a,\lambda} \lambda^4 d\lambda$ in $\text{nm}^6 \text{mol}^{-1}$ $q_{d,\lambda}$ is the normalised donor emission spectrum and $\epsilon_{a,\lambda}$ is the normalised acceptor absorption spectrum. The unperturbed lifetime of the donor, τ_0 , appears in both numerator (expression for R_0) and denominator. Thus upon cancelling the terms one is only left with radiative decay constants k_f in the numerator. This quantity reflects inherent properties of the fluorophores, including solvation and can be regarded as invariant under given experimental conditions. The equations for energy transfer efficiency can be written as

$$E = k_t \tau = \frac{(R_0)^6}{R_0^6 + R^6} = 1 - \frac{\tau_{FRET}}{\tau_0} = 1 - \frac{Q_{FRET}}{Q_0} \quad 20$$

R_0 , as explained earlier, is defined as the critical transfer distance also known as Foerster's radius, at which 50% of energy transfer occurs. τ_{FRET} is the lifetime of the donor in the presence of acceptor and τ_0 is the unperturbed lifetime of the donor. Q_{FRET} denotes the

reduction in the quantum yield of the donor molecule when involved in FRET and Q_0 the unperturbed quantum yield.

2.5 Fluorescence Lifetime Imaging Microscopy to probe FRET

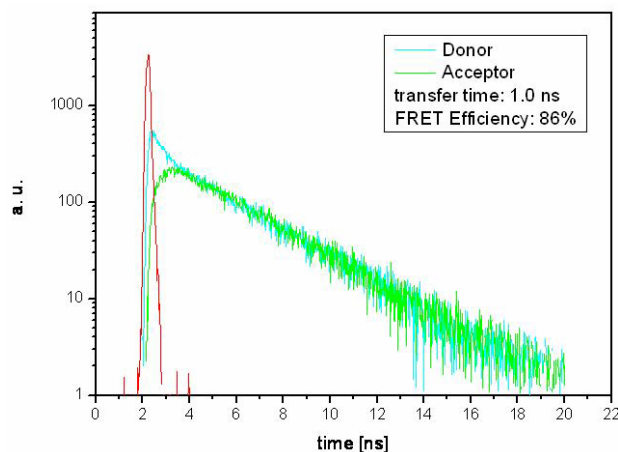


Figure 2.4) Simulation of a FRET pair with similar lifetime, different absorption, and emission spectra involved in energy transfer. The donor and acceptor are given in blue and green and both the molecules are assumed to be monoexponential with no overlap in the emission spectra. At the initial moments of the fluorescence decays when involved in FRET a sharp decrease (decay) in the donor and corresponding increase (rise) in the acceptor can be observed. These pre-exponential factors were fixed to be equal and opposite. When the transfer reaches an excited state equilibrium both the dyes decay back with same lifetime.

FLIM measurements of a microscopic object can be carried out with the help of advances in the field of single photon counting. Acquiring this lifetime map, corresponding to a microscopic object, is widely known as Fluorescence Lifetime Imaging Microscopy (FLIM). Conventional FLIM measurements are based on time domain or frequency domain measurements (Lakowicz, 1999). The time domain measurements utilise a pulsed excitation source in combination with time gated or statistical averaging detection technique. Frequency domain FLIM measures the modulation of excitation light by acousto optic modulators. Conventionally FLIM measures the donor fluorescence lifetime as a function of space. A cell expressing donor and acceptor dyes when imaged by FLIM will be detected as a lifetime map of the donor dye. The spatial differences in the lifetime of donor molecules in the presence of acceptor molecules at different subcellular areas are attributed to the occurrence of FRET. However, this method can not discriminate whether these reduction in the lifetimes are due to cellular artefacts like autofluorescence, changes in subcellular environment or concentration dependent oligomerisation, which reduces the lifetime of the donor. In order to circumvent these artefacts, the fluorescence emission of donor and acceptor were detected simultaneously with the analysis for the fast excited state reactions. FRET is a fast excited state reaction and causes an enhancement in acceptor intensity. In a time resolved process, this is observed as an increase in the excited state population of the acceptor. In the multiexponential analysis this will be distinguished as an exponential growth function (Figure 2.4) in contrast to an excited state decay function as observed for other environmental heterogeneities. In order to model donor and acceptor decays as fast excited state reaction as discussed in the previous section,

time and space correlated single photon counting detectors were implemented in a microscopy system to collect intensity decays of the samples along the wavelength resulting in simultaneous detection of donor and acceptor fluorophores. It was necessary because of the lack of commercially available systems to study all required parameters needed for the foresaid approach. Global analysis was performed to comprehend the characteristics of multiexponential decays at different wavelength channels.

2.6 FLIM-FLMS

Abbreviations frequently used in this section

TCSPC: Time correlated single photon counting

TSCSPC: Time and space correlated single photon counting

FLIM: Fluorescence lifetime imaging microscopy

FLMS: Fluorescence lifetime microspectroscopy

DL: Delay Line detector or Point detector

QA: Quadrant Anode detector or Imaging detector

OCFD: Optical constant fraction discriminator

L: Lens

M: Mirror

ND: Neutral density filters

CCD: Charge coupled device

2.6.1 Time and Space Correlated Single Photon Counting (TSCSPC)

Time correlated single photon counting detection (TCSPC) is a key method to record the impulse response functions of an ensemble. Every TCSPC measurement relies on the concept that the probability distribution for the emission of a single photon after an excitation event yield the actual intensity against time distribution of all the photons emitted. By sampling the single photon emission following a large number of excitation flashes, the experiment builds up the probability distribution (O'Connor and Phillips., 1984). In conventional life time imaging detection, a single beam or multiple beams are scanned through out the sample in order to reconstruct the spatial and corresponding temporal profile of the fluorescent object. In the experimental setup discussed in the thesis, nonscanning wide field detectors were used to statistically acquire the spatial and the corresponding temporal profiles of the sample. This method is named Time and Space Correlated Single Photon Counting (TSCSPC) (Kemnitz et al., 1997; Kemnitz et al., 1995). Here, a brief description of the detectors and their implementation in the FLIM-FLMS setup is presented.

2.6.2 Detectors

One dimensional imaging by the delay line (DL) (Europhoton GmbH, Berlin, Germany) (referred from now on as point detector) was used to statistically analyse a very small area of the sample (5-10 μm Diameter) and to resolve spectrally the corresponding fluorescent decays using a polychromator, placed in front of the point detector. The spectrally

resolved decays were collected by the detector as an electron cloud generated by a photocathode and amplified by two multichannel plates. The amplified electron cloud falls on a Delay Line disc producing current pulses in mutually opposite direction. The position of the single photon is traced one dimensionally from the travel time difference of the foresaid current pulses generated by the electron cloud falling on the detector. Time correlation was measured between the current pulse generated from the second multichannel plate and a signal from an Optical constant fraction discriminator (OCFD 401, Becker and Hickl, Berlin, Germany) triggered by the excitation laser beam. Thus, the acquisition with the point detector translates time and space coordinates into intensity dependent colour contour with 256 space channels and 1024 time channels.

The two dimensional QA detector (Europhoton GmbH) (from now on referred as imaging detector) was used to image the fluorescent decays within the whole illuminated region simultaneously. An incident single photon is converted into a cone shaped cloud of electrons by a photocathode and two microchannel plates in series. The electron cloud falls on four independent detector areas and from the ratio of charges developed in each of these single areas, initial (x-y) position of the photon is traced back into two dimensional spaces. For time correlation, a time to amplitude converter was used between the signal coming from the second multichannel plate and the signal from the optical constant fraction discriminator. Space and time correlated data are recorded as a 3D matrix of 512 x 512 space channels and 4096 time channels.

2.6.3 Instrumentation

The simplified scheme of experimental setup is shown in Figure 2.5. A femtosecond Titanium sapphire laser (Tsunami Model 3955, 690-1080 nm, 80 MHz, Spectra Physics, Mountain View, CA), pumped by a continuous wave visible diode laser (Millennia Vs, 5W, TEM₀₀ 532 nm, Spectra Physics) was tuned and frequency doubled using a frequency doubler/pulse selector (Model 3986, Spectra Physics) to a wavelength of 420 nm with a pulse repetition rate of 8 MHz. This wavelength was optimal to excite the donor CFP to at least 80% and the acceptor YFP to less than 5% (Lippincott-Schwartz and Patterson, 2003). Since the fluorescence decays of the fluorophores used (CFP, YFP) are in the range of 1-5 ns the repetition rate of the excitation pulses (125 ns) provided the fluorophores enough time to relax back to the ground state before they are excited by the next pulse. About 10% of the laser output from the frequency doubler/pulse picker was used to trigger the OCFD to determine the stop pulse of the excitation beam to the electronics of the detectors. The laser beam was guided by mirror M1 to two circular variable neutral density filters ND1 and ND2 (Thorlabs,

Karlsfeld, Germany), which were arranged in series to control the power of the laser beam. The laser beam was coupled alternatively via two optical fibres mounted on a three dimensional micrometer stage (Thorlabs) to different ports of an inverted microscope (IX81, Olympus, Hamburg, Germany) to illuminate the sample either for the point detector or the imaging detector. Manual switching between the different excitation paths to the microscope were performed using the mirror M2.

The collimated beam from the optical fibres passed the beamsplitter 450 DCLP (AHF Analysentechnik, Tuebingen, Germany) and illuminated the back focal plane of an oil immersion 100x objective (Plan Apo 100x/1.45 oil, TIRFM, Olympus). The fluorescence was collected via the objective and was reflected to the side port of the microscope after passing an emission filter HQ 460 LP. A manually switchable mirror M4 was used to alternate between the illumination ports of the point and imaging detector. The detectors were used alternatively in combination with optics suited for each detector.

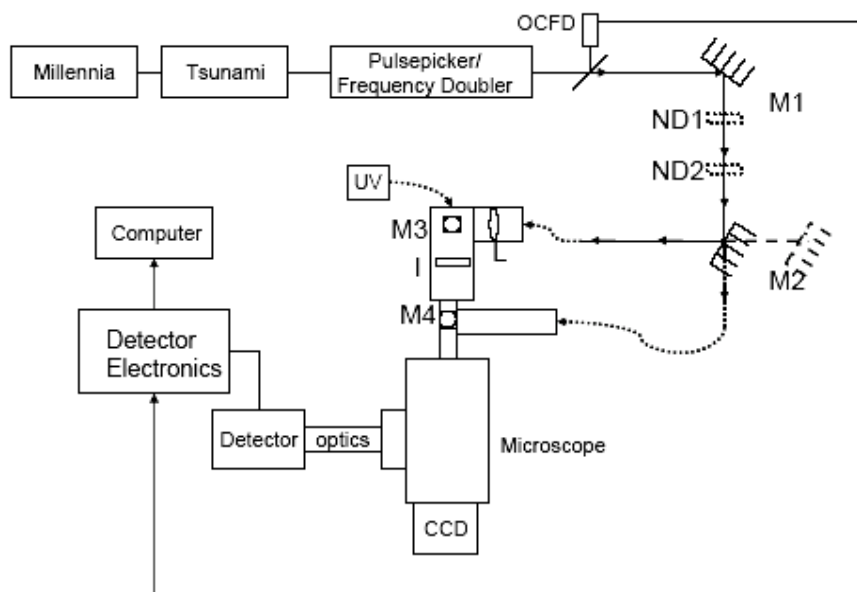


Figure 2.5) Picosecond FLIM setup for simultaneous detection of donor and acceptor lifetimes using both point and imaging detectors. OCFD: Optical constant fraction discriminator triggered by laser pulse, M: mirrors, ND: neutral density filters, UV: UV lamp for steady state imaging. L: planar convex lens, I: iris to control the area of excitation of the sample and CCD: charge coupled device for steady state imaging.

The point detector needs a very small excitation area so that it can selectively collect photons from a small defined region within the cell. In this case, the laser beam from the fibre output was focused by a convex lens, L, ($f=+150$ mm) (Edmund Optics, Karlsruhe, Germany) decreasing the area of illumination for the excitation beam. The region of interest was selected by closing an iris (I) within the excitation path around the beam to limit the area of excitation. The laser beam was finally focussed onto the sample. The fluorescence emission from the tiny selected area passed the emission filter HQ 460 ALP (AHF Analysentechnik) and the slit (11

mm x 0.10 mm) of the polychromator fixed in front of the sensitive area of the point detector to translate the spectrally resolved intensity decays on the detector.

The collimated beam from the optical fibre was used to provide whole field illumination for the imaging detector. In front of the imaging detector, a Dual Image (Europhoton GmbH) was mounted to split the fluorescent light into two specific cut off wavelength bands via a beamsplitter (dichroic 505 DCXR). Two bandpass filters define the width of the wavelength bands of the donor (CFP: D 480/40 M) and the acceptor (YFP: 540/40 ALP). These two fluorescence bands can illuminate two different areas of the imaging detector collecting the dynamics of donor and acceptor simultaneously. The QA capture software (Europhoton GmbH) was used to control the data acquisition of the imaging detector. Measurements were performed by continuously acquiring the photons for a certain time (15-25 min) to achieve a good signal to noise ratio. The imaging detector was cooled throughout the measurements between 14°C - 16°C to avoid over heating. The count rate on the detector was adjusted to be between 30,000 and 35,000 counts per second.

2.6.4 Steady state imaging

To perform steady state imaging the microscope was equipped with a charge coupled device (CCD) camera (F-View, SIS Imaging Systems GmbH, Duesseldorf, Germany) connected to the top port of the microscope (Figure 2.5). Mirror M3 was used to alter between excitation from a Mercury lamp coupled by an optical fibre and the laser illumination. The CFP and YFP signals were collected by filter settings (all filters from AHF Analysentechnik) of D436/20 excitation filter, 455 DCLP dichroic beam splitter, and D 480/40 emission filter for CFP and the YFP signal was imaged by HQ 500/20 excitation filter, Q 515 LP dichroic beam splitter, and HQ 535/30 excitation filter. Cells showing moderate expression levels of the transfected constructs were selected for imaging and FLIM-FLMS.

2.6.5 Calibration of the setup

Using the point detector the pulse width of the instrument response function (reflection of the pulsed excitation source from a mirror used as the microscopic sample) was reduced to a minimum of 150 ± 25 ps measured at full width half maximum by adjusting the threshold and zero control of the OCFD. A further reduction of the pulse width was not possible due to the rapid fall of counts caused by very low excitation intensity. The excitation intensity at the sample was reduced to $100 \mu\text{W}/\text{cm}^2$ (measured by a laser power meter, PD-300-3W, Ophir Optonics GmbH, Rohrsen, Germany) to minimise phototoxicity for long period observation of living cells.

The wavelength calibration of the point detector was performed using a Xenon lamp (6035 Hg (Ar), Oriel Instruments, Stratford, CT) as a microscopic sample and the illumination intensity was controlled using neutral density filters inserted between the objective and detector. The defined emitted lines of the lamp were compared to those lines observed in the spectral window of the detector and thereby the wavelength channels were optimised. The wavelength sensitivity of the system was characterised to be 1.02 nm/channel (Figure 2.6). The time calibration of the point detector was performed by measuring the instrument response function at different known delays and thereby calculating the sensitivity of time channel from the shift in the decay along the time channels for the corresponding delays. The time channel resolution of the point detector was calculated to be 24.81 ps/channel (Figure 2.6).

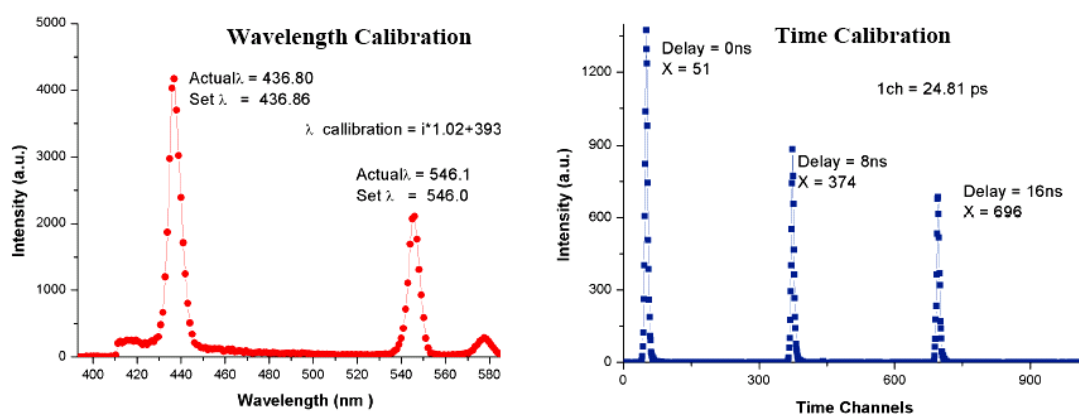


Figure 2.6) Wavelength and time calibration for the point detector. The known wavelength emission lines of a Xenon lamp were used as a reference to calibrate the spectral sensitivity of the wavelength channels of the point detector. The calibrated wavelength channels were compared to the emission lines to check the accuracy of the calibrated wavelength channels. Time calibration was performed by using known delays 0, 8 and 16 ns to introduce a shift in the instrument response function along the time channels. This shift introduced with delays was used to calibrate the time channel sensitivity of point detector.

The pulse width of the instrument response function in the imaging detector was reduced to a minimum of 200 ± 20 ps at full width half maximum, similar to the point detector. The space calibration of the imaging detector was performed using fluorescent beads of 1 μm and 0.17 μm diameters (Ps-Speck™, Molecular Probes INC, Eugene). The detector was optimised to result in the best focussed image of the bead in the image plane, which corresponds to its minimum diameter. Time calibration of the imaging detector was performed similar to the calibration of the point detector by changing the delay and calculating the shift along the time channels. The time channel resolution of the imaging detector was calculated to be 9.72 ps/channel (Figure 2.7).

The FLIM-FLMS set up was calibrated with a magic angle measurement of the monoexponential dye coumarin6 in ethylene glycol, excited at 420 nm and observed in a band

of 515 ± 15 nm (HQ 515/30, AHF Analysentechnik) observed with the point and the imaging detector respectively. This was performed as an independent control before every set of measurements.

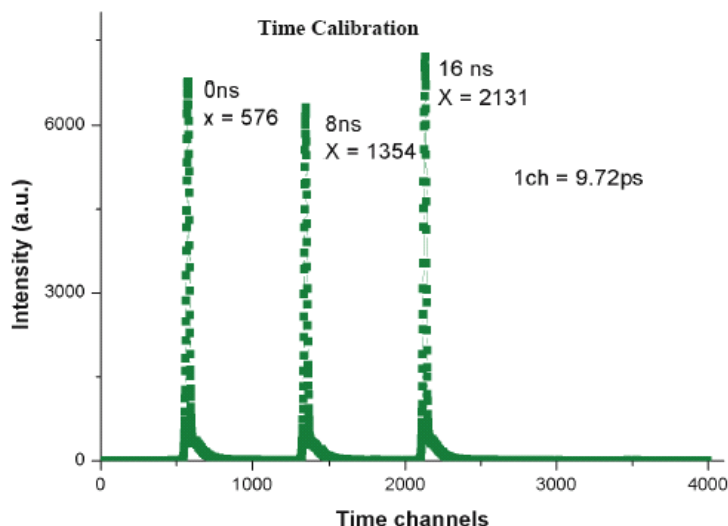


Figure 2.7) Time calibration for the imaging detector. Time calibration was performed by using known delays 0, 8 and 16 ns to introduce a shift in the instrument response function along the time channels. This was used to calibrate the time channel sensitivity of point detector.

2.6.6 Data analysis

To obtain lifetimes from fluorescence decays, the measurements were modelled by the convolution product of a multi-exponential theoretical model with the instrument response function (IRF): $i(t) = \text{IRF}(t) \otimes \sum \alpha_i e^{-t/\tau_i}$. α_i is the relative contribution of the fluorescent species, characterised by the fluorescence lifetime τ_i and IRF is the measurement of the pulsed excitation obtained by acquiring the reflection of the laser beam to the detector. Data were analysed by a Levenberg-Marquardt non-linear least-squares algorithm using the Globals Unlimited software package (Version 1.20) developed at the Laboratory for Fluorescence Dynamics at the University of Illinois at Urbana-Champaign (Beechem, 1992).

Data obtained from the point detector were fit with linked lifetimes along different decays corresponding to different emission wavelengths. The decays were obtained by gathering data over a fixed number of continuous wavelength channels via addition of blocks of wavelength channels equivalent to 6.12 nm. The contribution of the lifetimes in the intensity decays were obtained from pre-exponential factors. The pre-exponential factors of lifetimes were plotted at different wavelengths to obtain the Decay Associated Spectrum (DAS). The comparison of DAS of different multiexponential components allowed to

discriminate the fluorescent species involved in a fluorescence emission of different excited state processes.

Data obtained by the imaging detector were analysed by selecting corresponding regions of interests for the CFP and YFP channels as defined by the filter settings of the Dual Image. The data sets of individual channels were exported to the Globals Unlimited software format. The donor and acceptor decays were analysed with linked lifetimes. The quality criterion of the global fit was defined as $\chi^2 < 1.3$ for all analysed decays. The criterion for improvement of χ^2 on addition of multiexponential components were set to a value of $\Delta\chi^2$, the ratio between the χ^2 of the previous model and the current model with the addition of a single lifetime component, to be greater than $\Delta\chi^2 > 1.05$. The values of χ^2 were checked by using the linked multiexponential model and the unlinked model and the data were discarded if the ratio of the χ^2 was greater than 1.05 indicating a random error originating from the data acquisition. The intensity decays of coumarin6 at magic angle were observed to be monoexponential with lifetimes of 2.30 ns for the point detector and 2.29 ns for the imaging detector which was in agreement with the published value of 2.30 ns (Kapusta et al., 2003).

FRET efficiencies can be calculated as a ratio of the rate of energy transfer from donor to acceptor k_T to the total decay rate of the donor

$$E = k_T / (\tau_D^{-1} + k_T) \quad (21)$$

Where, τ_D is the mean lifetime of the donor in the unperturbed environment in the absence of excited state reactions. In the time domain the energy transfer efficiency is calculated by

$$E = 1 - \tau_{DA} / \tau_D \quad (22)$$

Where, τ_{DA} is the mean lifetime of the donor in the presence of an acceptor. The mean lifetime τ_{mean} of a multiexponential fluorophore is calculated by

$$\tau_{\text{mean}} = \sum \alpha_i \tau_i / \sum \alpha_i \quad (23)$$

Where, τ_i is the lifetime and α_i is the corresponding pre-exponential factor. α_i and τ_i are calculated by global analysis. The pre-exponential factor α_i of intensity decay is positive except in the case of excited state reactions where the amplitude of the individual pre-exponential factors changes to a negative sign, as discussed in Section 2.3 (Lakowicz, 1999). α_i was plotted along the wavelength to obtain the DAS. The fractional contributions of different lifetimes in the intensity decay were calculated from the pre-exponential factors of the multiexponential model. The fractional contribution was calculated by $\alpha_i / \sum \alpha_i$ for the

different exponentials in the model. DAS can also be used to calculate the fractional contribution along the wavelength. Using fluorophores with multiexponential decays the decay rate of the donor due to FRET is defined as

$$k_T = \sum k_i \quad (24)$$

Where, the value of i can range from 0 to n depending on the number of conformations which are involved in FRET. The FRET efficiency was also calculated using the multiexponential lifetimes involved in the energy transfer as

$$E_i = 1 - \tau_{DAi} / \tau_{Di} \quad (25)$$

Where, τ_{Di} is the unperturbed lifetime of the donor and τ_{DAi} is the donor lifetime in the presence of the acceptor.

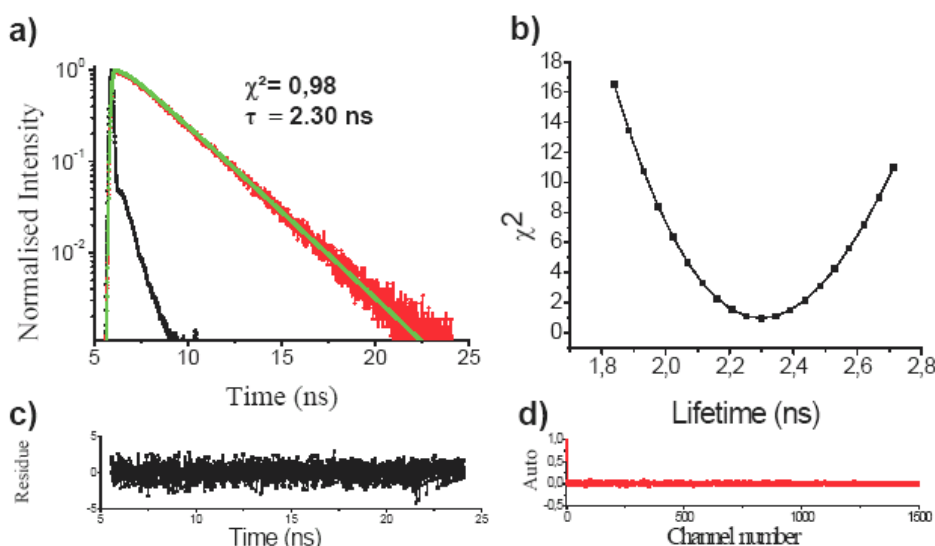


Figure 2.8) Example of a coumarin6 measurement at magic angle a) deconvolution of raw data (red) by the instrument response function (black) gives the resulting intensity decay (green). The intensity decay was monoexponential with a lifetime of 2.3 ns. b) Rigorous error analysis of the lifetime obtained from global analysis. The 2.3 ns lifetime was varied between 1.8 ns and 2.8 ns in 20 intervals to obtain the realistic variation of χ^2 . The minimum χ^2 of 0.98 was obtained with the lifetime of 2.3 ns well in agreement with the previous global analysis indicating that global minimum gives the best lifetime. c) The residue and d) autocorrelation of the fit data are given, indicating the goodness of the fit.

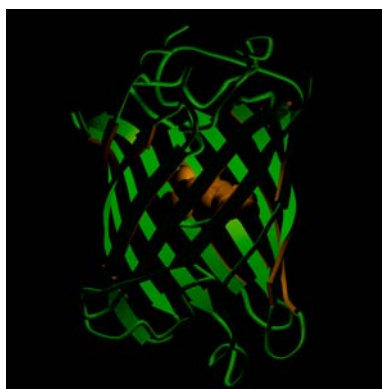
Rigorous error analysis using the global analysis program was performed to obtain a realistic estimation of the variation of χ^2 associated with each lifetime. The global analysis programme employs a completely rigorous error estimation procedure. Within the error analysis segment, a set of intervals was defined for each lifetime in the model performing a complete set of analysis. The examined parameter was fixed at the current trial value, but all other parameters were allowed to vary to minimise the value of χ^2 . A plot of the change of χ^2 with the change in lifetimes was obtained. Comparison of these results with the obtained multiexponential model was used to judge the quality of lifetimes in the fit. An example is

illustrated in Figure 2.8, which depicts the quality of fit which could be seen by residue and autocorrelation. The obtained lifetime was also checked by rigorous analysis.

2.7 Fluorescence tags to image macromolecular dynamics

Imaging macromolecular association with microscopic approaches requires that the molecules of interest are fluorescently labelled (Tsien, 1998; Zhang et al., 2002). The chemiluminescent protein from jellyfish *Aequorea Victoria* was purified and DNA was modified to fluoresce intrinsically upon expressing in different cell types. This is called Green Fluorescent Protein (GFP). The GFP DNA can be fused to the cDNA of interest, the recombinant DNA of which can be introduced into a cell. GFP functions as an efficient marker of this protein of interest, when expressed in the cell. In optimal cases, GFP does not interfere with the functions of the fused protein and can be used to study the subcellular localisation and macromolecular association in living cells. However, this has to be assessed individually for each constructs.

Figure 2.9) Structure of GFP (green) monomer to show internal chromophore. The chromophore is depicted in orange. GFP is 11-stranded β -cans with a central α -helix, on which lies an autocatalytically created chromophore. (from tsienlab.ucsd.edu/Images.htm)



At present GFP or its Stokes shifted variants are most often used to fluorescently tag a protein. GFP, comprised of 238 amino acids (26.9 kDa), displays a barrel like structure and in centre the fluorophore is formed by three amino acids (Figure 2.9). The fluorophore consists of residues 65-67 (Serine – *dehydro* Tyrosine - Glycine) of the protein. The cyclised backbone of these residues forms the imidazolidone ring. These cylindrical barrels are very stable structures, which protect the central fluorophore from drastic environmental effects. By site directed mutagenesis, several colour variants of GFPs are available. GFPs are not only used for biological purposes but they themselves are the source of providing insights into a variety of photophysical and photochemical properties of macromolecules. The GFP colour variants are suitably combined to study FRET since the Stokes shifted fluorescence spectra enable them to be used as donor acceptor pairs tagged to the same or different proteins (Ellenberg et al., 1999; Emptage, 2001; Jares-Erijman and Jovin, 2003; Shaner et al., 2005). One of the most commonly used FRET pair is Cyan Fluorescent Protein (CFP) in

combination with Yellow Fluorescent Protein (YFP) (Chan et al., 2001; Dye et al., 2005; Evans and Yue, 2003; Karpova et al., 2003; Zal and Gascoigne, 2004). In this work a photostable variant of YFP called Topaz was used as the acceptor. Eventhough Topaz is brighter its anionic sensitivity is enhanced with respect to that of YFP. However Topaz showed similar excitation and emission characteristics of the YFP. FRET studies exploit the advances in genetically targetable fluorescence proteins (Gadella, 1999; Harpur et al., 2001; Pepperkok et al., 1999) for monitoring the interaction of macromolecules (Chan et al., 2001; Day et al., 2001; Harpur et al., 2001) conformational changes of macromolecules (Nakanishi et al., 2006; Zheng et al., 2004) and ratiometric sensing of intracellular environments (Kuner and Augustine, 2000; Truong et al., 2001). Time resolved spectroscopy of these proteins has revealed the complex transient nature of the fluorescence of these GFPs in cells and in solutions (Chattoraj et al., 1996; Habuchi et al., 2002; Suhling et al., 2002; Tramier et al., 2004). To interpret how these fluorophores can be involved in different excited state processes like FRET in living cells, it is very important to understand the basic photophysical properties at high temporal resolution.

2.8 Photophysics of GFP based FRET

Though CFP and YFP are among the common FRET pairs used, the mechanisms of energy transfer in these constructs remain unclear. In order to comprehend the photophysical mechanism of FRET in these fluorescent proteins, different genetically encoded constructs were used where CFP and Topaz are separated by varying spacer lengths. This information of FRET when CFP and YFP are placed in single constructs will be used to verify the folding of macromolecules (folding of Lck) and activity-dependent conformational changes in macromolecules (Lck, SAP97/hDlg and SAP90/PSD95) in living cells. The changes in intramolecular FRET in constructs will be probed, and the changes in FRET efficiencies will be used as a basis to interpret the biological phenomena of interest. The photophysical framework was based on the DAS where the spectrally resolved decays were used to comprehend the wavelength dependence of FRET. The negative pre-exponential factor in the acceptor emission region will be the fundamental criterion for identifying FRET. This negative pre-exponential factor in YFP emission region is regarded as the true proof of FRET since artefacts like cellular autofluorescence, changes in intracellular environment and oligomerisation of proteins cannot mimic this. Addressing how the CFP and YFP undergo FRET is essential in formulating a kinetic model for the FRET system and interpreting the biologically relevant questions of resting state and activity-dependent protein folding.

3 MATERIALS AND METHODS

3.1 Materials

3.1.1 Chemicals

All chemicals used were of analytical grade and from the companies Calbiochem, Invitrogen, Merck, Roche, Roth, Serva and Sigma-Aldrich. Special chemicals and solutions used are described in the corresponding method descriptions. Solutions were prepared with water purified on a Milli-Q® System, Millipore.

3.1.2 Bacteria and mammalian cell culture media and antibiotics

Name	Composition/Company
LB medium	20 g LB broth base powder (Invitrogen) in 1 l H ₂ O.
S.O.C. medium ⁽¹⁾	20 g/l SELECT peptone 140 (Invitrogen); 5 g/l SELECT yeast extract (Invitrogen), 10 mM NaCl, 2.5 mM KCl, 10 mM MgCl ₂ , 10 mM MgSO ₄ , 20 mM glucose.
LB agar	15 g select agar (Invitrogen) in 1 l LB medium.
DMEM(+)	Dulbecos Modified Eagle's Medium (Invitrogen), 10% (vol/vol) fetal calf serum, 2 mM L-glutamine and 100 U/ml penicillin and 100 µg/ml streptomycin
Neurobasal (+)	Neurobasal without Phenol red (Invitrogen), 2% (vol/vol) B27 (Invitrogen), 2mM L-Glutamine and 100 U/ml penicillin and 100 µg/ml streptomycin
Optimem	Optimem without Phenol red. (Invitrogen)
RPMI 1640(+)	RPMI 1640 medium (Biochrome AG, Berlin, Germany) containing 10% (V/V) FCS and 1% (V/V) penicillin streptomycin (Biochrome AG)
Ampicillin	Stock: 50 mg/ml ampicillin sodium salt in H ₂ O. Final concentration: 100 µg/ml in LB or 2-YT medium.
Kanamycin	25 mg/ml kanamycin disodium salt in H ₂ O. Final concentration: 25 µg/ml in LB medium.

Table 3.1 Media and antibiotics used for growth of bacteria or mammalian cell cultures. ⁽¹⁾ (Hanahan, 1983))

3.1.3 Buffers

Name	Composition /Company
PBS	2.7 mM KCl, 1.5 mM KH ₂ PO ₄ , 137 mM NaCl, 8 mM Na ₂ HPO ₄ , pH 7.4
PBS / Ca / Mg	0.5 mM CaCl ₂ , 0.5 mM MgCl ₂ in PBS, pH 7.4
1×KD ⁽¹⁾	pH 7.4, 129mM NaCl, 5 mM KCl, 2 mM CaCl ₂ 2H ₂ O, 1 mM MgCl ₂ 6H ₂ O, 20 mM Hepes, 30 mM Glucose
Electrophoresis Buffer	250 mM Tris, 1.92 mM glycine, 1% (wt/vol) SDS
1×TAE	40 mM Tris, 0.2 mM acetic acid, 1 mM EDTA, pH 7.6
1×TBE	40 mM Tris, 0.2 mM boric acid, 1 mM EDTA, pH 7.6
HBSS	Hans Bank's Salt Solution (Invitrogen)

Table 3.2 Frequently used buffers and their composition. ⁽¹⁾ (Deisseroth et al., 1998))

3.1.4 Cell strains

Bacteria	E. coli XL10 gold heat shock competent cells (Stratgene)
	E coli XL1 blue chemical competent cells (Stratgene)

Mammalian Cells	COS-7, African Green Monkey
	Jurkat E 6.1, T-Lymphocytes
	JCaM E 1.6, T-Lymphocytes
	Raji cells, B-Lymphocytes

Table 3.3 Cell strains used.

3.1.5 Antibodies

Primary antibodies	Company / Reference	Dilution
		IF
Mouse anti-Bassoon ⁽¹⁾	Map7f (Stressgen*)	1:1000
Rabbit anti-Bassoon ⁽¹⁾	Sap7f (Wilko Altmock*)	1:500
Rabbit anti-SAP90/PSD95	Synaptic Systems	1:200
Rabbit anti-SAP97/hDlg	Acris	1:1000
Mouse anti-Lck	BD transduction Laboratories	1:250
Rabbit anti-Lck	Biosource International	1:200
Mouse anti-GFP	Synaptic Systems	1:200
Rabbit anti-GFP	Synaptic Systems	1:200

Table 3.4 Primary antibodies used for immuno cytochemistry. IF denote immunofluorescence.* indicate those obtained from Institute for Neurobiology, Magdeburg, ⁽¹⁾ (tom Dieck et al., 1998)

Secondary antibodies	Company	Dilution
peroxidase-conjugated goat anti-mouse IgG	Dianova	1:10,000
Alexa Fluor [®] 488 goat anti-mouse/rabbit IgG F(ab')	Molecular Probes	1:200
Alexa Fluor [®] 568 goat anti-mouse/rabbit IgG F(ab')	Molecular Probes	1:200
Alexa Fluor [®] 594 goat anti-mouse /rabbit IgG F(ab')	Molecular Probes	1:200
Cy3 goat anti-mouse/rabbit IgG	Dianova	1:100
Cy5 goat anti-mouse/rabbit IgG	Dianova	1:100

Table 3.5 Secondary antibodies used.

3.1.6 GFP fusion constructs

Construct (Name)	Gen	Source	Details
pECFP	CFP	Clontech	GFP variant
pEYFP	YFP	Clontech	GFP variant
pEGFP	GFP	Clontech	GFP variant
Clomeleon C8T	Clomeleon	T Kuner (Heidelberg)	CFP-8AA-Topaz ⁽¹⁾
Clomeleon C16T	Clomeleon	T Kuner (Heidelberg)	CFP-16AA-Topaz ⁽¹⁾
Clomeleon C24T	Clomeleon	T Kuner (Heidelberg)	CFP-24AA-Topaz ⁽²⁾
pECerulean	Cerulean	D Piston (Tennessee)	GFP variant ⁽³⁾
W51	Lck	H Stockinger (Vienna)#	N-term-unique-CFP-SH3-SH2-kinase-Cterm-YFP
W52	Lck	H Stockinger (Vienna)#	N-term-unique- SH3-CFP-SH2-kinase-Cterm-YFP
W53	Lck	H Stockinger (Vienna)#	N-term-unique- SH3- SH2- CFP-kinase-Cterm-YFP
W54	Lck	H Stockinger (Vienna)#	N-term-unique- SH3- SH2- kinase-Cterm-YFP
W55	Lck	H Stockinger (Vienna)#	N-term-unique-CFP-SH3-SH2-kinase-Cterm

CFP SAP90/PSD 95	SAP90/PSD95	M Kreutz/ F Nagel*	CFP-SH3-HOOK-GUK
FRET SAP90/PSD 95	SAP90/PSD95	M Kreutz/ F Nagel*	CFP-SH3-HOOK-GUK-YFP
FRET SAP97/hDlg	SAP97/hDlg	M Kreutz/ F Nagel*	CFP-SH3-HOOK-GUK-YFP
GFPI1-I2-SAP97/hDlg	SAP97/hDlg	A. Chishti/T. Hanada*	GFP-I1-I2 SAP97/hDlg ⁽⁴⁾
GFPI1-I3-SAP97/hDlg	SAP97/hDlg	A. Chishti/T. Hanada*	GFP-I1-I3 SAP97/hDlg ⁽⁴⁾
GFP I3-SAP97/hDlg	SAP97/hDlg	A. Chishti/T. Hanada*	GFP-I3 SAP97/hDlg ⁽⁴⁾

Table 3.6 Vectors and expressing GFP constructs used in the present study. * indicate the constructs obtained in collaboration with neurochemistry department, IFN, Magdeburg. # indicates the constructs obtained from Department of Immunology, Magdeburg.

⁽¹⁾ (Nair et al., 2006), ⁽²⁾ (Kuner and Augustine, 2000), ⁽³⁾ (Rizzo et al., 2004), ⁽⁴⁾ (Hanada et al., 2003)

3.1.7 Primers

Name	Primer sense	Sequence(5'→ 3')	Gene bank acc. no.
hDlg_Nterm_rev1	R	CATCTCCAATGTGTGGGTTGTC *	U13896
hDlg_Nterm_rev2	R	CTGTGCCAT TAACGTAAGTTGG *	U13896
hDlg_Nterm_fw1	F	CAGAGAGCATTGCACCTT TTGG *	U13896
M13	F	GTAAAACGACGGCCAG #	
M13	R	CAGGAAACAGCTATGAC #	

Table 3.7 Primers involved in the cloning of different N-terminal spliced insertions of SAP97/hDlg. F=Forward, R=Reverse. * and # indicate primers obtained from Biomers or Invitrogen

3.1.8 Animals

Rats (*Rattus Rattus norvegicus*) from the strain Wistar, bred by the Leibniz Institute for Neurobiology animal facility, were used for the preparation of primary neuronal cultures.

3.2 Methods

3.2.1 Biochemical methods

3.2.1.1 Transformation of chemical competent cells

To transform E.coli XL1 blue cells, 0.5 µg DNA were added to cells thawed on ice and, after an incubation period of 15 min on ice, they were resuspended in S.O.C. medium (Section 3.1.2, (Hanahan, 1983)). Cells were incubated for 1 h at 37° C and plated on LB agar plates containing the appropriate antibiotics. Single colonies were isolated for the purification of transformed plasmid

3.2.1.2 Transformation of heat-shock competent cells

To transform XL 10 gold heat-shock competent cells, 0.4 µg DNA were added to cells thawed on ice. Subsequently, the mixture was incubated 5 min on ice, 45 sec at 42° C and 2 min again on ice. After the heat shock, cells were resuspended in S.O.C. medium, incubated 1 h at 37° C and plated on LB agar plates containing the appropriate antibiotics. Single colonies were isolated for the purification of transformed plasmid

3.2.1.3 Preparation of plasmid DNA from *E. coli*

For the purification of plasmids, the method of alkaline lysis was used. 2-4 ml of overnight cultures were pelleted down and then resuspended in 0.2 ml of buffer 1 (10 mM EDTA, 50 mM Tris/HCl pH 8.0, 100 µg/ml RNase). This was followed by the addition of 0.2 ml of buffer 2 (0.2 M NaOH, 1% (wt/vol) SDS) to the samples to disrupt the cell membrane, denature proteins and DNA, and hydrolyse RNA. This suspension was neutralised with 0.2 ml of buffer 3 (3 M potassium acetate, pH 5.5), which caused the precipitation of the denatured proteins along with the chromosomal DNA and most of the SDS detergent. The precipitates were removed by centrifugation and the plasmid-containing supernatant was further purified by isopropanol precipitation. 0.35 ml isopropanol were added to the plasmid-containing supernatant, the mixture was incubated 10 min on ice and finally the DNA was pelleted at 20,000 g for 10 min. Pelleted DNA was washed twice with 70% (vol/vol) ethanol, resuspended in 10 mM Tris/HCl (pH 8.0) and stored at -20°C. To transfect mammalian cells, plasmids were prepared using the Endo free Plasmid purification Midiprep Kit (Quiagen) or the Endo free Plasmid Purification Maxiprep Kit (Quiagen).

3.2.1.4 Restriction reaction of plasmid DNA

Restriction endonucleases are enzymes that cleave DNA double strands after recognising specific nucleotide sequences. To clone or subclone cDNA fragments into a vector, or to check the purified plasmids, they were submitted to a restriction reaction using the appropriated restriction endonucleases, buffers, reaction temperatures and time conditions (normally 60-90 min at 37° C) recommended by the manufacturer (New England Biolabs or Fermentas). Since double digests are rarely 100% efficient, vectors were dephosphorylated with alkaline phosphatase (Roche) to prevent the re-ligation of the cohesive ends.

3.2.1.5 Agarose gel electrophoresis

The DNA fragments obtained after a restriction reaction were separated horizontally, according to their size, by agarose gel electrophoresis. 0.5-1.5% (wt/vol) agarose was melted in TAE /TBE buffer. To detect the DNA under UV light, 0.1 µg/ml ethidium bromide was added to the agarose gel solution and was poured into a chamber. 6 x loading buffer (30% (vol/vol) glycerol, 50 mM EDTA, 0.25% (wt/vol) bromphenol blue, 0.25% (wt/vol) xylene cyanol) was added to the samples before loading them into the agarose gel. SmartLadder (Eurogentec) or 100 bp DNA Ladder (New England Biolabs) were used as reference standards. The gels were run at 65V in TAE buffer and were documented with the gel documentation system Gel Doc (BioRad). After separation of the DNA fragments by electrophoresis, the agarose gel was placed on a transilluminator (Stratagene) to visualise the

localisation of the DNA of interest. If required for cloning, the DNA-containing area was cut out and isolated from the gel using an UltraClean 15 purification kit (MoBio Laboratories Inc), following the instructions of the manufacturer.

3.2.1.6 Reverse transcription polymerase chain reaction (RT-PCR)

The reverse transcription polymerase chain reaction is a common method used to construct a DNA fragment of interest from the total RNA template. The DNA fragment constructed was amplified, using a pair of oligonucleotide primers. These primers act complementary to one end of the DNA target sequence. The final PCR products were obtained from the RNA template using Superscript One-Step™ RT-PCR system. In order to detect the N-terminal splicing of SAP97/hDlg in T-lymphocytes RT-PCR reactions were performed on the total mRNA of Jurkat E6.1 cells. The reaction conditions used were:

Assembling reaction	
2X reaction mixture	25 µl
Sense primer	1 µl
Antisense primer	1 µl
RNA template	2 µl
Enzyme mixture	1 µl
Distilled Water	20 µl
Final Volume	50 µl
Thermal Cycling	
cDNA synthesis and pre-denaturation	
1 cycle	
45°C-55°C for 30 min	
94°C for 2 min	
PCR	
40 cycles	
Denature: 94°C for 15sec	
Anneal : 50°C-65°C for 30sec	
Extend : 68°C-72°C for 1 min/kb	
Final extension : 72°C for 5-10 min	
Transcriptase and Polymerase	
Superscript II reverse transcriptase*	
Taq DNA polymerase*	

*obtained from Life Technologies

3.2.1.7 Cloning of a DNA fragment into a vector

2 µl of PCR products were mixed with 1 µl of salt solution and 2.5 µl water and incubated for 15 min with 0.5 µl TOPO TA vector (Invitrogen). This mixture was used to transform “XL10 gold heat shock competent” bacteria. Plasmids were prepared from single colonies and were sequenced (SEQLAB Sequence Laboratories Göttingen GmbH) or submitted to restriction analysis to confirm the correct insertion of the cloned or subcloned DNA.

3.2.2 Cell biological methods

3.2.2.1 Mammalian cell cultures

3.2.2.1.1 Culturing of Jurkat T cells

Jurkat T cells were grown at a density of 2×10^5 /ml in RPMI 1640 (+) medium in a humid incubator with 5% CO₂ at 37⁰ C.

3.2.2.1.2 Culturing of COS7 cells

COS 7 cells were cultured in media DMEM (+), at 37° C, with 5% CO₂ and 95% humidity.

3.2.2.2 Transfection of mammalian cells

3.2.2.2.1 Transfection of Jurkat T cells

Cells were transfected with 20 µg of cDNA of different constructs of interest using an electroporation system gene pulser[®] II (BioRad, Hercules, CA) set at a capacitance of 950 µF and a charging pulse of 230V and an electroporation cuvette (Model 640, GAP 4 mm, BTX, Holliston MA). Cells were recovered overnight, washed twice in Phenol red free RPMI 1640 medium (Gibco BRL, Invitrogen, Carlsbad, CA); transferred to poly-D-lysine coated glass-bottom dishes (MaTek, Ashland, MA) and measured.

3.2.2.2.2 Transfection of COS7 cells

COS7 cells were transfected with cDNA of interest with Polyfect transfection reagent (Life Technologies)

3.2.2.3 Stimulation of Cells

3.2.2.3.1 Stimulation of T cells

The cells taken in poly-D-lysine coated glass bottom dishes were stimulated by 50 µl CD3 antibody (OKT3) (1µg/µl) for T-cell stimulation. The cells were also presented with CD4/CD28 cross-linked Dyna beads of 4.5 µm diameter or Sepharose beads of 10 µm diameter (Bangs Laboratories). Raji cells incubated overnight with SEE (20µm/ml) and washed 2 times with 1×PBS were used as Antigen presenting cells for Jurkat T cells.

3.2.2.3.2 Stimulation of COS7 cells

COS7 cells transfected with different constructs of interest were stimulated using 50µM Thapsigargin (Sigma-Aldrich) in 1×KD (Section 3.1.3, (Deisseroth et al., 1998)) for depleting intracellular calcium stores. Intracellular activity of the calcium binding protein calmodulin was blocked using W7 (Sigma-Aldrich), a drug which inhibits calmodulin

activity. Cells incubated with 20 μ M W7 in 1 \times KD, prior to the stimulation, were used as negative control.

3.2.2.4 Immunocytochemistry

2 \times 10⁷ cells were centrifuged for 30 sec at 6000 RPM with or without antibody coated beads, and resuspended using wide pore tips in 2 ml of 1 \times PBS (Invitrogen). 200 μ l of resuspended cells were carefully placed on poly-D-lysine-coated coverslips in 24-well plates. These cells were fixed for 10 min with 1% (wt/vol) paraformaldehyde (in PBS) at time points of 0, 5, 10, 15, 20, and 30 min after incubation with beads. The fixed cells were washed carefully 3 times using 1 \times PBS with 10 min between each washing step. Cells were blocked and permeabilised using blocking solution (10% (vol/vol) horse serum, 5% (wt/vol) BSA and 0.2 mg/ml Tritonx-100 in PBS) for 10 min. Samples were then incubated with the primary antibodies overnight at 4^o C, washed three times with blocking solution and incubated with the secondary antibodies for 1 h. Finally, they were washed with blocking solution, PBS and water and then embedded in Mowiol (10% (wt/vol) Mowiol (4-88), 25% (wt/vol) glycerol, 100 mM Tris/HCl, pH 8.5). All steps were carried out at room temperature unless otherwise stated.

3.2.2.5 Imaging

3.2.2.5.1 Fluorescence microscopy

Confocal laser-scanning microscopy was performed with a Leica TCS-SP2-AOBS laserscanning confocal microscope (Leica Microsystems, Mannheim) using the Leica TCS software package. Images were acquired using sequential scans in order to avoid cross talks for multiple staining. Images were processed using ImageJ (NIH) or Adobe Photoshop software (Adobe Photoshop CS, Adobe).

3.2.2.5.2 Live cell translocation studies

The cells were stimulated with antibody coated beads or Antigen presenting cells. The subsequent changes in cell morphology and the changes in the fluorescence intensity were observed. An inverted epifluorescence microscope (Leica, DM IRE2) was equipped with an EMCCD (Cascade 512) controlled by Metavue software package for the purpose. The images were acquired in an interval of 20 sec after the stimulation continuously for a time period of 30 min. Images were processed using ImageJ or Adobe Photoshop software.

3.2.2.5.3 Time resolved Imaging

Fluorescence lifetime imaging and energy transfer studies of cells expressing fusion constructs were performed using the newly assembled FRET-FLIM system (chapter 2).

3.2.3 Structural modelling of Lck

Several structures of the autophosphorylated Lck kinase domain have been solved by crystallography. The compact intramolecular complex of the kinase, SH2, and SH3 domains were solved for Hck (hemopoietic cell kinase), another member of the Src kinase family. The sequences of Lck and Hck are highly conserved (71% identical, 86% similar), and the kinase fold is nearly identical in both proteins. Therefore, Hck protein data bank (PDB) was used as entry 1qcf as structural template for the homology modelling of Lck. The structure of the N-terminal unique domain (residues 1–120) is unknown, except for a cysteine zinc complex comprising a partial folded peptide of the unique domain and a target peptide from CD8, studied by NMR model. Building of the complete unique domain was done by using the method of threading, as homology modelling failed due to the lack of a required sequence homology to known structures in the PDB Protein threading methods. Threader (Jones et al., 1992), GTD (McGuffin and Jones, 2003), Rosetta (Bystroff et al., 2000), and Phyre (Kelley et al., 2006) were applied on the unique Lck sequence. All failed to predict a qualified fold, but Phyre gave a hint by diphtheria toxin fold, which was finally used to model a globular structure of the unique domain.

A hydrophobic binding pocket built by two beta turns characterises the unique domain. One exposes the two cysteines of the Zn binding site (20-CENC-23). The binding pocket allows further quality restrictions to the selection of target peptides containing the C-X-C motif. Beside that compact multidomain Hck fold, intermediate conformations were modelled towards an elongated Lck structure. In this elongated structure all domains were considered to be dissociated from each other. The fluorescent fusion proteins were inserted into the inactive tyr-505 phosphorylated compact, the tyr-394 autophosphorylated active compact and into the active elongated Lck structure. The ECFP and EYFP sequences used in the experiments were modelled using coordinates of PDB entries 1CV7 and 1YFP, respectively. ECFP differs to 1CV7 by corresponding mutations K27R and N165H, while both EYFPs are identical. The orientation of the fluorescent barrel domains were optimised by rigid-body positional refinement using X-PLOR (Brunger, 1988). All structures were modelled using SwissModel Server (Guex and Peitsch, 1997) and visualised using X11 version of PyMol (DeLano, 2002). Final coordinates were validated using procheck (Laskowski et al., 1996).

(*) This structural model of Lck was done by Carsten Reissner to supplement the result of FLIM measurements of Lck FRET constructs (section 4.2).

4 RESULTS

4.1 Photophysics of FRET between CFP and YFP in living cells

The sensitivity of the imaging approaches utilising FRET and FLMS for studying conformational changes of molecules (Section 2.8) was addressed using the different size variants of Clomeleon (Kuner and Augustine, 2000). Clomeleon is a chimeric protein comprising of CFP and Topaz separated by a spacer. Topaz is an anionic sensitive variant of YFP with similar absorption and emission spectra as YFP. The FRET dynamics were compared between tandem constructs of Clomeleon with varying spacers of 8 aa, 16 aa, and 24 aa, which will be referred as C8T, C16T, and C24T, respectively. Investigating the photophysics of CFP in cells expressing CFP alone or the tandem constructs allowed to discriminate the FRET dynamics between these constructs, as discussed below.

4.1.1 Fluorescence dynamics of ECFP in Jurkat T cells

Living Jurkat T cells expressing ECFP ($n=6$) at moderate levels were measured. The fluorescence emission spectrum of ECFP was normalised at its emission maximum and plotted along the wavelength (Figure 4.1 a). The emission maximum of ECFP was measured in the range of 486.4 ± 1.02 nm and the lifetimes of ECFP were analysed along the wavelength between 468 nm and 590 nm. For this purpose, the spectrum was divided into 20 bands of 6.12 nm each. Deconvolution of intensity decays of ECFP yielded two lifetimes 3.37 ± 0.03 ns and 1.06 ± 0.03 ns. In the band corresponding to the ECFP emission maximum (483.8 ± 3.06 nm) (Figure 4.1 b), the long and short lifetime component contributed to $59.6 \pm 2.1\%$ and $40.4 \pm 2.2\%$, respectively. This resulted in a mean lifetime of 2.44 ± 0.08 ns for ECFP (Table 4.1). The pre-exponential factors obtained for each lifetime and the corresponding contributions were plotted along the wavelength (Figure 4.1 c), resulting in the DAS of ECFP. The percentage of contribution of the two ECFP lifetimes along the wavelength was calculated. A slight reduction in the contribution of the long lifetime component along with corresponding increase in the short lifetime component was observed towards the longer wavelength region of the emission spectrum (Figure 4.1 d). The resulting mean lifetimes of ECFP were calculated for the different wavelength channels, and a slight decrease was observed towards the longer wavelength region of the spectrum (Figure 4.1 e). This can be attributed to the changes in the contributions of the long and short lifetime components along the wavelength, resulting in such changes in the mean lifetimes. Due to the absence of excited state reactions, the pre-exponential factors of different components in the intensity decays remained positive.

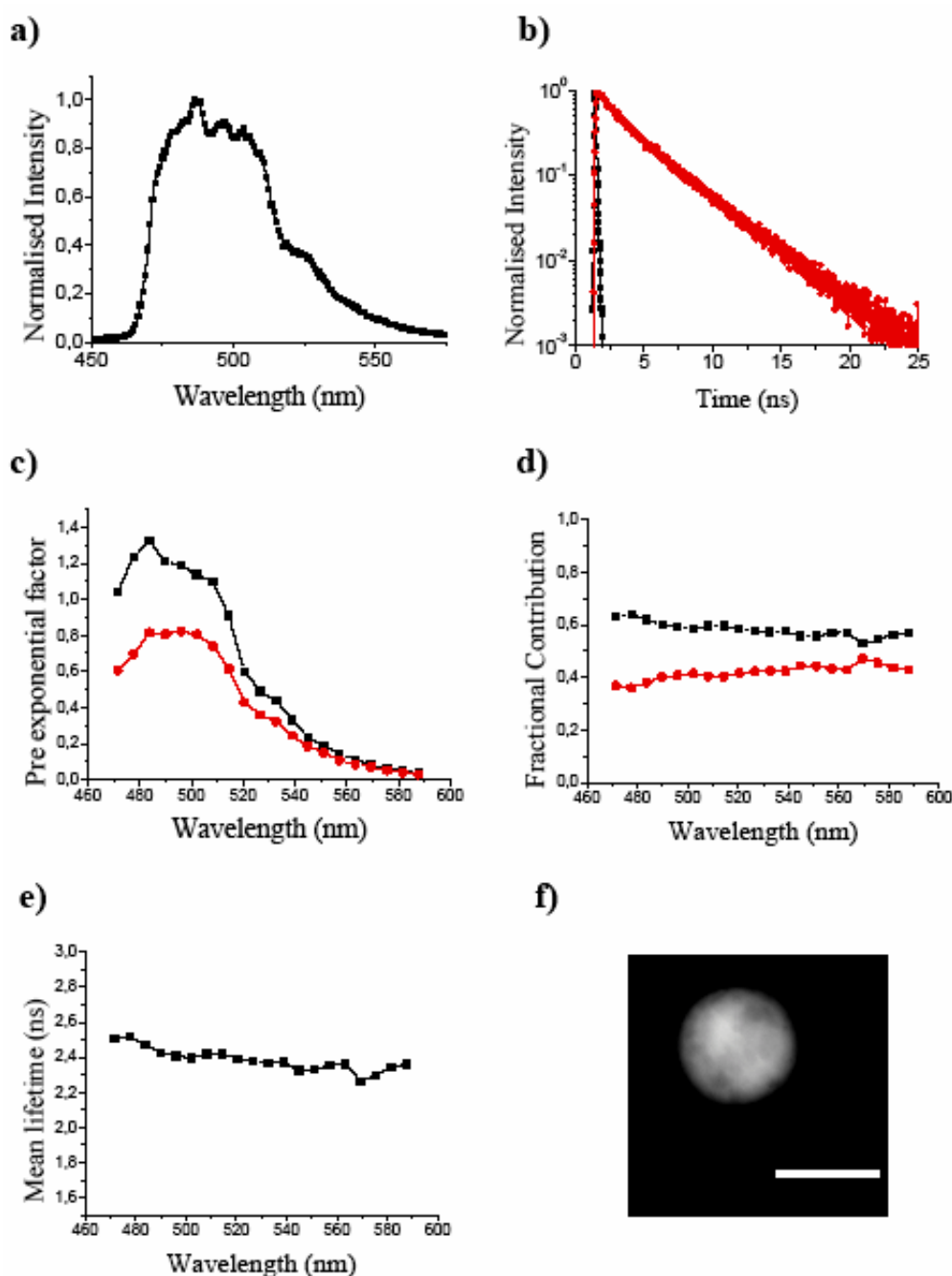


Figure 4.1) a) Fluorescence emission dynamics of ECFP in Jurkat T cells. The excitation peak was 420 ± 1.02 nm. b) Intensity decay of CFP (red) deconvoluted with IRF (black) at its emission maximum in a band of 483.8 ± 3.06 nm. The decays were fit with a biexponential model with lifetimes of 3.37 ± 0.03 ns and 1.06 ± 0.03 ns c) DAS of ECFP. Intensity decays of all measurements were analysed in 20 emission bands from 470 nm to 590 nm, and the pre-exponential factors of lifetimes 3.37 ± 0.03 ns (black) and 1.06 ± 0.03 ns (red) were plotted along the wavelength. (d) The contribution of both the lifetimes 3.37 ± 0.03 ns (black) and 1.06 ± 0.03 ns (red) were calculated, and plotted as normalised fractional contributions along the wavelength. (e) Mean lifetimes of intensity decays were plotted along the wavelength. (f) CCD image of Jurkat T-cell expressing ECFP (bar: 10 μ m).

4.1.2 Fluorescence emission dynamics of size variants of Clomeleon

Global analysis was performed on data sets acquired by the point and the imaging detectors. The fluorescence dynamics of the FRET constructs were studied and compared with those of control ECFP. Complete characterisation of their spectra, multiple lifetimes,

pre-exponential factors of individual decays, DAS, fractional contributions of lifetimes, and the mean lifetimes of intensity decays were done for the purpose. Changes in the amplitude of pre-exponential factors at the acceptor emission maximum were used as an evidence for the presence of FRET.

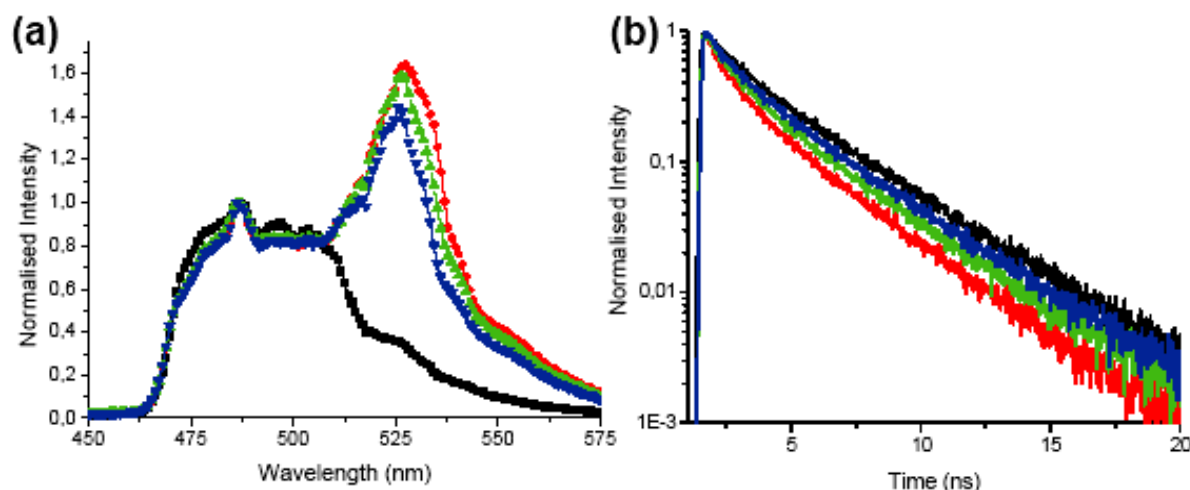


Figure 4.2) (a) Comparison of representative fluorescence emission spectra of ECFP (black) with size variants of tandem constructs, C8T (red), C16T (green) and C24T (blue). (b) Comparison of fluorescence intensity decays of ECFP and the size variants of tandem constructs at the emission maximum of CFP at a band of 483.8 ± 3.06 nm. The intensity decays of FRET variants C8T (red), C16T (green) and C24T (blue) were faster compared to ECFP (black). The fastest decay was detected in the case of C8T, indicating best FRET efficiency. The intensity were ensured to have 10^4 counts at the donor emission maximum with $\chi^2 < 1.3$.

4.1.3 Fluorescence emission spectra of size variants of Clomeleon

The spectra of different Clomeleon constructs were plotted after normalising them at the CFP peak (Figure 4.2 a). The ratios of intensity (R) at the Topaz emission peak (527.3 ± 1.02 nm) to the CFP emission peak (486.4 ± 1.02 nm) were calculated for the different constructs, and the constructs were characterised using their R values. C8T and C24T displayed the highest and lowest R values among the constructs of 1.69 ± 0.35 and 1.49 ± 0.20 , respectively (Table 4.1). C16T showed an intermediate value of 1.56 ± 0.25 . These values were calculated from independent measurements of different Clomeleon transfected cells ($n=9$) showing similar expression levels. The results indicated the maximum FRET efficiency for C8T and the minimum for C24T. From the measurements of R values of different size variants, it was concluded that C24T shows minimum variability within a cell culture, compared to the other constructs (Table 4.1).

4.1.4 Modelling of intensity decays

The two conformational states of CFP were considered to be independent donors (Borst et al., 2005). Since these conformers can independently be involved in FRET, four lifetimes were expected from the donor CFP in the FRET variants. The intensity decays of all the FRET constructs were modelled with 3 exponentials, since modelling with 4 exponentials

did not show a significant improvement in χ^2 and fit. The lifetime analysis was done analogous to section 4.1.1. All measurements were performed using the point detector, unless otherwise stated. The percentage of contribution of different lifetimes and the mean lifetimes were calculated for intensity decays of different wavelength bands along the spectrum (Table 4.1).

Table 4.1. Multiple lifetimes and the percentage of contribution of each lifetime for ECFP and CFP of size variants of Clomeleon expressed in Jurkat T cells.

Construct	τ_1 [ns]	τ_1 [%]	τ_2 [ns]	τ_2 [%]	τ_3 [ns]	τ_3 [%]	τ_{mean} [ns]	R
ECFP	3.37±0.03	59.6±2.1	1.06±0.03	40.4±2.2	*	*	2.44±0.08	*
C8T	3.39±0.03	23.7±4.7	1.31±0.07	30.3±1.2	0.16±0.02	46±4.1	1.27±0.12	1.69±0.35
C16T	3.41±0.04	26.6±3.3	1.32±0.04	32.6±1	0.16±0.02	40.8±3.9	1.41±0.12	1.56±0.25
C24T	3.42±0.02	30.6±2.5	1.35±0.04	34.7±1.6	0.19±0.02	34.7±3.3	1.59±0.09	1.49±0.20

The multiple lifetimes and their contributions were calculated by the global analysis software. The mean lifetimes were calculated as described in the data analysis section. The construct which has the smallest linker showed the shortest mean lifetimes and the highest R values, indicating it to be the best FRET construct. R values were calculated from the ratios of YFP to CFP peaks in the emission spectra of different Clomeleon constructs.

4.1.5 Fluorescence lifetime dynamics of size variants of Clomeleon

In living Jurkat T cells (n=5) expressing C8T, the obtained lifetimes were 3.39±0.03 ns, 1.31±0.07 ns and 0.16±0.02 ns (Table 4.1). The intensity decay at the emission maximum of CFP (483.8±3.06 nm) was faster compared to the control sample (Figure 4.3 b). The percentage of contributions of the three lifetimes at the bands corresponding to the emission maximum of CFP and Topaz (527.3±3.06 nm) were calculated. The contribution at the donor maximum was 23.7±4.7% for the long lifetime and 30.3±1.2% and 46±4.1% for the two short lifetimes, respectively. DAS revealed negative pre-exponential factors for the two short lifetime components of 1.31±0.07 ns and 0.16±0.02 ns in the wavelength channels near the emission maximum of Topaz (Figure 4.3 d). An increase in the contribution of the long lifetime component with a subsequent reduction in the contributions of the two short lifetimes near the emission maximum of the acceptor was observed (Figure 4.3 e).

At the acceptor emission maximum, the contributions of the lifetimes were 86.1±3.5%, 7.8±4.9% and 6.1±5.3% respectively. The change in sign of the pre-exponential factors from positive to negative was due to the occurrence of FRET from CFP to Topaz. This negative amplitude in the intensity decays of acceptor is regarded as a characteristic of excited state reaction when measured in the time domain. Due to energy transfer, the mean lifetime of the intensity decay at the donor maximum increased from 1.27±0.12 ns to 3.03±0.11 ns at the

acceptor emission maximum (Figure 4.3 f). The change in sign of the pre-exponential factors associated with the lifetimes along with the changes in mean lifetimes confirmed the presence of FRET in C8T (Figure 4.3).

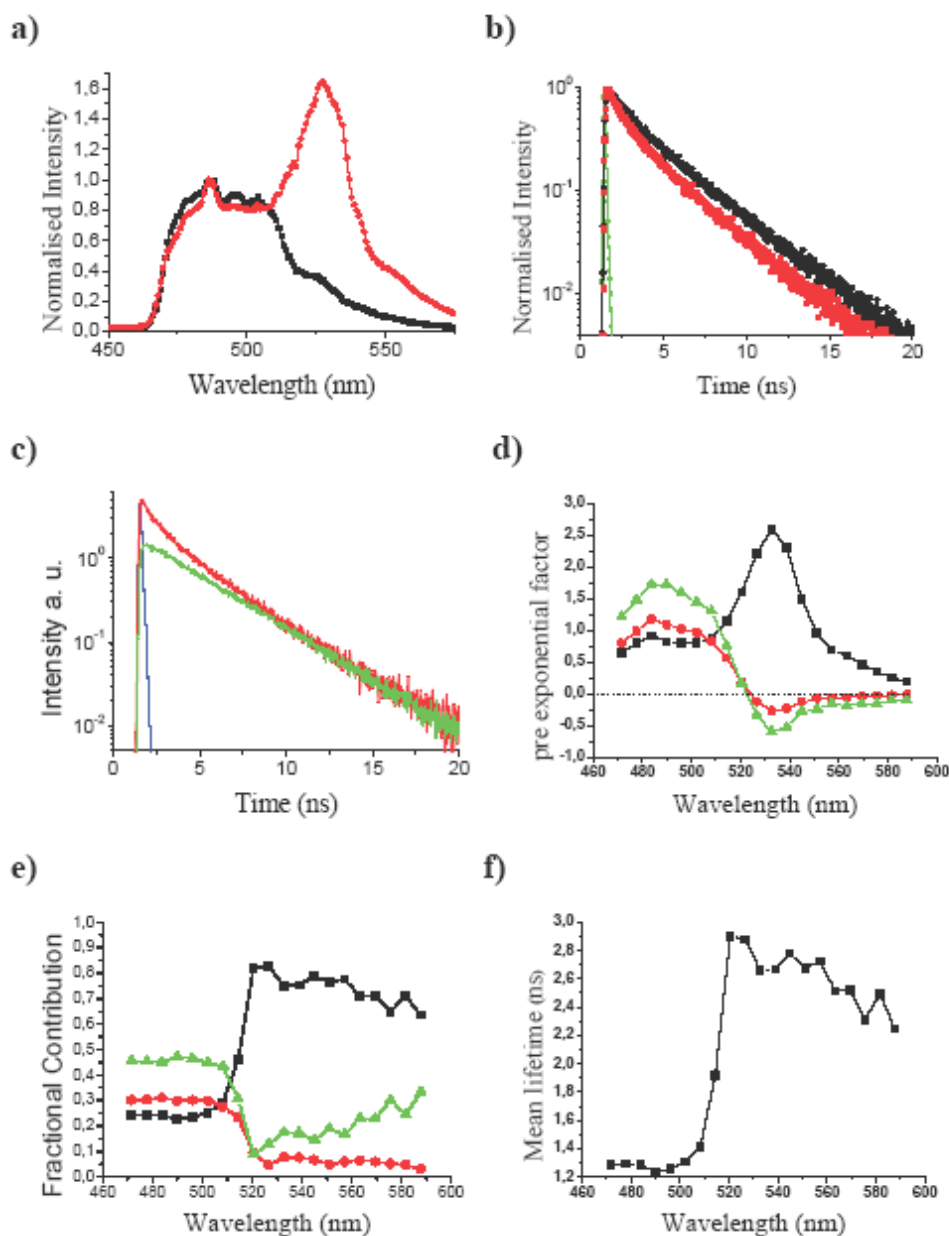


Figure 4.3) a) Comparison of fluorescence emission spectra of ECFP (black) and C8T (red) in Jurkat T cells. The excitation peak was $420 \pm 1.02 \text{ nm}$. b) Intensity decays of CFP control (black) and C8T (red) at the emission maximum in a band of $483.8 \pm 3.06 \text{ nm}$. The mean lifetime of CFP of $2.44 \pm 0.08 \text{ ns}$ was reduced to $1.27 \pm 0.12 \text{ ns}$ for the FRET sample (c) Decay and rise of CFP and Topaz in C8T. The intensity decay of CFP (red) at a band of $483.8 \pm 3.06 \text{ nm}$ and the intensity decay at Topaz (green) emission maximum in a band of $527.3 \pm 3.06 \text{ nm}$. (d) DAS of C8T. The decays were fit by a three exponential model with lifetimes of $3.39 \pm 0.03 \text{ ns}$ (black), $1.31 \pm 0.07 \text{ ns}$ (red) and $0.16 \pm 0.02 \text{ ns}$ (green). Intensity decays of all measurements were analysed in 20 emission bands from 470 nm to 590 nm . At the emission maximum of Topaz (between 520 and 540 nm), the amplitude of the pre-exponential factors of the two short lifetimes were negative, indicating an excited state reaction. e) The contributions of lifetimes in intensity decays were calculated and plotted as normalised fractional contributions along the wavelength. (f) Mean lifetimes of intensity decays were calculated along the emission bands and were plotted along the wavelength. There was a sharp increase in the mean lifetimes at the emission maximum of Topaz. The intensity decays had 10^4 counts at the maximum with global analysis $\chi^2 < 1.3$.

The lifetime dynamics of C8T in living T cells ($n=4$) were additionally studied using the imaging detector (Figure 4.4), which provided a better time resolution of 9.72 ps/channel compared to the point detector (24.81 ps/channel). These decays were fit with a three exponential model analogous to the results from the point detector, and the lifetimes obtained were 3.25 ± 0.03 ns 1.29 ± 0.06 ns and 0.22 ± 0.03 ns (Figure 4.4 b). The percentage of contributions of these lifetimes was similar to the data obtained from the point detector. Within the donor band, the long lifetime component contributed to $23.3 \pm 2.6\%$, and the shorter lifetimes to $33.5 \pm 0.5\%$ and $43.2 \pm 2.9\%$. The contributions of the individual lifetimes in the acceptor band were $83.3 \pm 3.4\%$, $6.4 \pm 2.7\%$ and $10.3 \pm 6.1\%$. This resulted in mean lifetimes of 1.28 ± 0.08 ns and 2.82 ± 0.15 ns in the donor and acceptor bands, respectively.

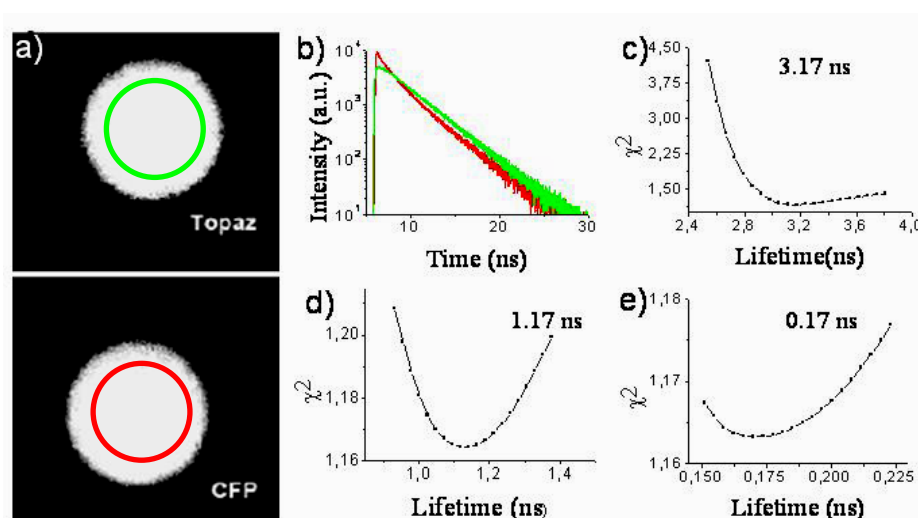


Figure 4.4) (a) Two channel visualisation of a Jurkat T-cell expressing C8T by the imaging detector. The wide field fluorescence emission signal was split into two wavelength bands of CFP and Topaz with the Dual Image to detect simultaneously the time resolved images of donor and acceptor. (b) Simultaneous analysis of donor and acceptor namely, CFP (red) and Topaz (green) from regions of interests marked in (a): Analysis resulted in three lifetimes 3.23 ns, 1.24 ns and 0.21 ns. The pre-exponential factor of 0.21 ns showed the negative amplitudes in the acceptor channel for C8T. Rigorous error analysis was performed for different lifetime components obtained for the intensity decay of the donor namely, 3.2 ns (c), 1.17 ns (d) and 0.17 ns (e). The changes in χ^2 over the changes in lifetimes were plotted to check the quality of the lifetimes obtained from global analysis. The minimum of the curve was detected to be comparable to the values obtained from the multiexponential analysis.

Using the imaging detector, the negative pre-exponential factor was observed only for the shortest lifetime component in contrast to the point detector, which showed negative contributions for both the shorter lifetimes. This was because the imaging detector utilised emission filters with bandwidths of 40 nm to detect the donor and the acceptor emission, while the point detector combined a long pass filter and a polychromator for a wavelength resolution of continuous bands of 6.12 nm. Therefore, the effects were averaged out in the imaging detector, due to the larger wavelength detection band. The lifetimes obtained with both detectors were similar at the level of multiexponential decays, as well as in the percentage of the contributions of these lifetimes at the donor (480 ± 40 nm) and the acceptor

(540±40 nm) bands. The mean lifetime within the donor band was also similar to that obtained from the point detector. Rigorous error analysis was used to investigate the realistic spread of χ^2 associated with each lifetime obtained from the Global Analysis (Figures 4.4 c, 4.4 d, 4.4 e). Since the point detector provided better wavelength resolution of 6.12 nm compared to the wavelength bands of the band pass filters (40 nm) of the imaging detector, the studies of the other size variants of Clomeleon were based on the measurements with the point detector, as discussed below.

The lifetimes obtained for C16T in living Jurkat T cells (n=5) were 3.41±0.04 ns, 1.32±0.04 ns and 0.16±0.02 ns. The individual lifetimes obtained for C16T were comparable to those of C8T (Table 4.1). The DAS of the individual lifetimes indicated that in the case of C16T, the two shorter components showed a change of sign in the pre-exponential factors from positive to negative at the acceptor maximum similar to the results of C8T (Figure 4.5 b). Analyzing the percentage of contribution of the lifetimes at the donor emission maximum, the long lifetime contributed to 26.6±3.3% and the two shorter lifetimes with 32.6±1% and 40.8±3.9% respectively. The contributions of the lifetimes along the acceptor channels changed to 88±1.7%, 7.3±3.4% and 4.73±4.12% (Figure 4.5 e). Although the lifetimes of C8T and C16T were similar, the fractional contributions of the individual lifetimes were changed significantly as shown in Table 4.1. As the spacer length increased, the τ_3 was decreased in its contribution while both τ_1 and τ_2 have increased in their contribution. This resulted in an increase of the mean lifetime of the C16T construct to 1.41±0.12 ns at the donor and 3.11±0.09 ns at the acceptor maximum. When plotting the mean lifetime along the wavelength, the results of C16T were similar to the results of C8T, indicating an increase in the mean lifetime at the acceptor emission region within the spectrum.

The global fit of the data obtained from T cells expressing C24T (n=5) yielded three lifetimes of 3.42±0.02 ns, 1.35±0.04 ns and 0.19±0.02 ns. These lifetimes obtained from C24T are slightly different from the shorter constructs (Table 4.1). When the contributions of these lifetimes were compared at the CFP emission maximum the contribution from the two long lifetimes were increased to 30.6±2.5% and 34.7±1.6% meanwhile the contribution of the shortest lifetime decreased to 34.7±3.3% (Table 4.1). At the acceptor emission maximum the contribution of these lifetimes were 88.2±2.3%, 7.8±3.2% and 4.01±4%. This has resulted in an overall increase in the mean lifetime at the donor emission maximum to 1.59±0.09 ns and at the acceptor emission maximum to 3.14±0.08 ns. The plots of the mean lifetime along the wavelength, DAS (Figure 4.5 c) and contribution of lifetimes (Figure 4.5 f) were similar to the other size variants of Clomeleon. In the plot of DAS of C24T, the two shorter lifetimes

showed negative amplitude for the pre-exponential factors near the Topaz emission maximum. The plot of the mean lifetime along the wavelength showed a sharp increase in the mean lifetime at the acceptor emission region.

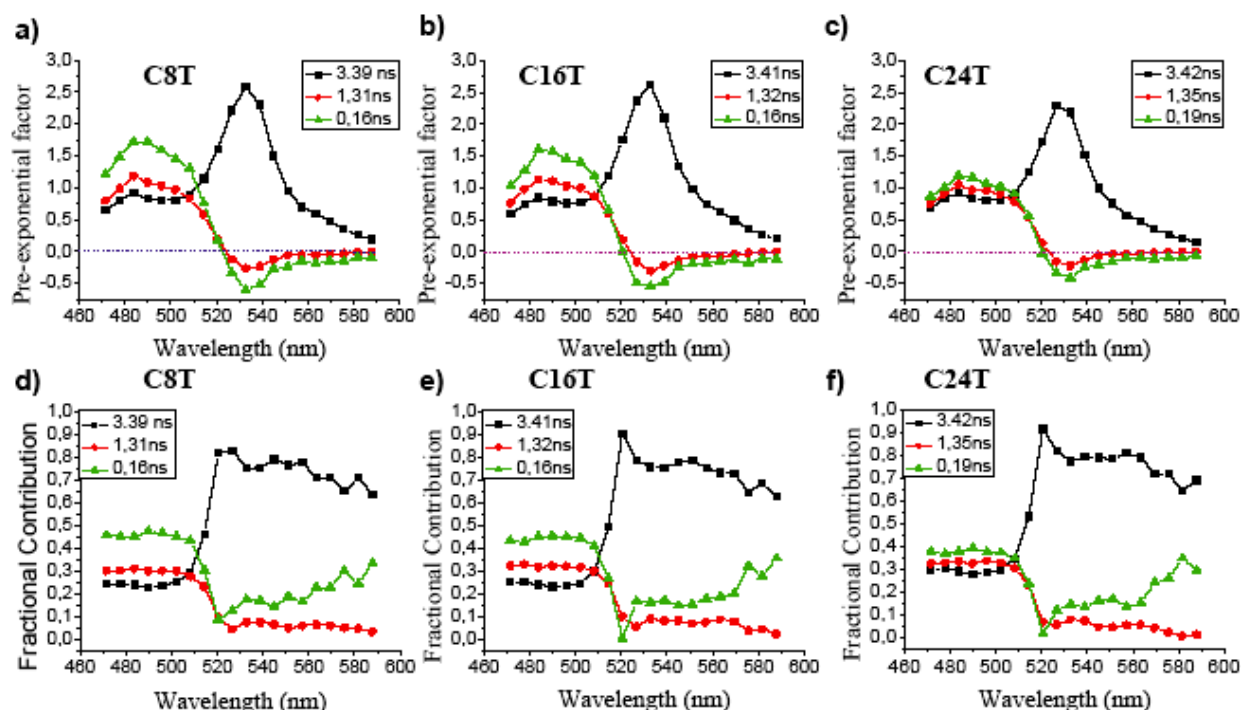


Figure 4.5) Comparison of DAS for different tandem constructs shows a significant increase in the contribution of longer lifetimes and a corresponding reduction in the contribution of short lifetimes with increase in spacer length. Intensity decays of all measurements were analysed in 20 emission bands from 470 nm to 590 nm. (a) Plot of DAS for C8T. (b) Plot of DAS for C16T. (c) Plot of DAS for C24T (d) Plot of fractional contribution for lifetimes obtained for C8T. (e) Plot of fractional contribution for lifetimes obtained for C16T. (f) Plot of the fractional contribution of the lifetimes obtained for C24T.

Modelling with multiexponential analysis revealed that the difference between the obtained lifetime components for different constructs were very similar (Table 4.1). The control ECFP was modelled with 2 exponentials whereas the CFP in the FRET constructs had to be modelled with 3 exponentials (Table 4.1). It was observed that the long lifetime component observed in the control was very similar to the long lifetime observed in FRET constructs indicating that to be from the fraction of CFPs, which may not be involved in energy transfer. τ_2 from all the FRET constructs were longer than the short component of the unperturbed donor. Thus, τ_2 in FRET constructs can be a mix of the second conformation of CFP not taking part in FRET with the long lifetime component of CFP involved in FRET. The energy transfer efficiency was calculated with this approach from multiexponential lifetimes and mean lifetimes. For τ_2 from the FRET constructs τ_1 in the control CFP was taken as the unperturbed donor lifetime to calculate $E \tau_2$ (Table 4.2). For τ_3 of the FRET constructs τ_2 of the ECFP single transfection was taken as unperturbed donor lifetime to calculate $E \tau_3$ (Table 4.2). C8T with the shortest spacer between the fluorophores showed the fastest decay

(Figure 4.2 b) among the constructs hinting the possibility of better energy transfer efficiency within the constructs (Table 4.2).

Table 4.2. Efficiency of energy transfer occurring from multiple conformations of CFP of different size variants of Clomeleon

Construct	E τ_2 [%]	E τ_3 [%]	E τ_{mean} [%]
C8T	61.1 \pm 5.4	84.9 \pm 12.8	47.9 \pm 10.0
C16T	60.8 \pm 3.2	84.9 \pm 12.8	42.2 \pm 9.1
C24T	59.9 \pm 3.1	82.1 \pm 10.9	34.8 \pm 6.5

Based on the assumptions that the lifetimes showing negative pre-exponential factors are FRET lifetimes originating from both the conformations of CFP involved in energy transfer. FRET efficiencies are calculated with respect to the unperturbed multiexponential donor lifetimes acting as control. FRET efficiencies of energy transfer are also calculated from mean lifetime of each construct, which is in direct relationship with R value calculated from the ratio of YFP to CFP peaks in the emission spectra of different Clomeleon constructs.

The involvement of multiple lifetimes in FRET was identified by plotting their pre-exponential factors along the wavelength resulting in the DAS. Comparison of DAS of each of the different Clomeleon constructs (Figures 4.5 a, 4.5 b and 4.5 c) revealed that the amplitude of the pre-exponential factors of τ_2 and τ_3 changed from positive to negative at the emission maximum of the acceptor. The negative amplitudes of the pre-exponential factor at the Topaz emission maximum indicated that the energy transfer caused the excitation of the Topaz from CFP rather than the direct excitation by the laser pulse. The relative contributions of the lifetimes were calculated as fractional contributions of the intensity decays along the wavelength to compare different Clomeleon constructs (Figures 4.5 d, 4.5 e and 4.5 f). The shortest construct C8T showed maximum contribution of the shortest lifetime. As the number of amino acids in the spacer was increased in steps of 8, a reduction was observed in the contribution of the shortest lifetime and a subsequent increase in the contribution of the longer lifetimes (Table 4.1). This is indicative to the differences in energy transfer within the FRET constructs showing that the efficiency of energy transfer is increasing with a decrease in spacer length.

4.2 Activity-dependent conformational changes of Lck in living cells

The dynamic nature of the folding of the non-receptor tyrosine kinase Lck was addressed by tagging ECFP and EYFP at different regions of the protein. The multiexponential analysis along with Decay Associated Spectra allowed to distinguish the variability of intramolecular FRET, and verified the structure of full-length Lck in living cells. To understand structural regulation of Lck, T cells expressing Lck FRET constructs were stimulated either by Antigen presenting cells or soluble antibodies. This allowed to track the real-time changes in the conformation of Lck in response to a physiological stimulus.

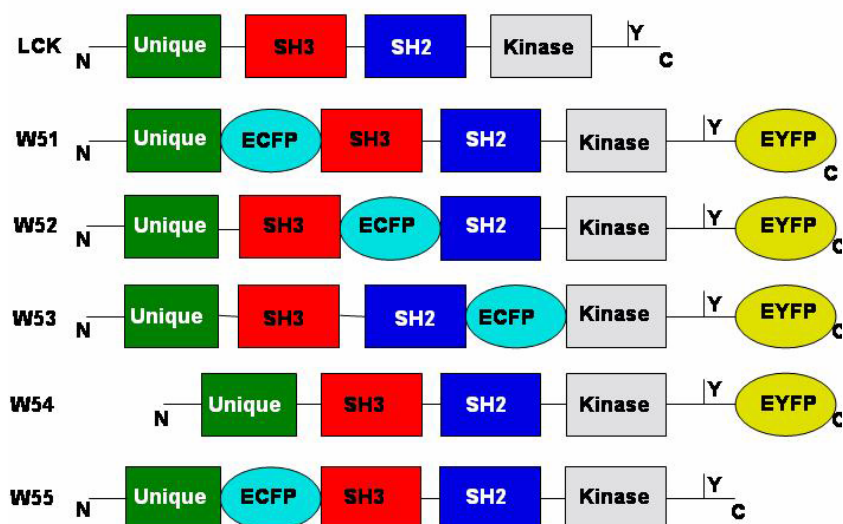


Figure 4.6) Schematic representation of the protein domain architecture of Lck. It shows the position of ECFP and EYFP in different variants of Lck used for FRET-FLIM studies. The tyrosine residue at the C-terminus of Lck (Y-505) is marked as Y in the scheme.

4.2.1 Domain organisation of Lck fusion constructs

To verify the folding of the multidomain protein Lck, the protein was tagged with ECFP and EYFP at different regions (Figure 4.6). The position of EYFP was kept constant at the C-terminus while the position of ECFP was altered within the construct. The variation in intramolecular FRET between the constructs was used to comprehend the final folded structure of the protein. The construct where EYFP was tagged at the C-terminus of the protein will be referred to as W54. The position of ECFP was between the unique and SH3 domains (W51), between SH3 and SH2 domains (W52) and SH2 and kinase domains (W53). The protein expressing ECFP between the unique and SH3 domains with no EYFP was used as the FRET control (W55) (Figure 4.6).

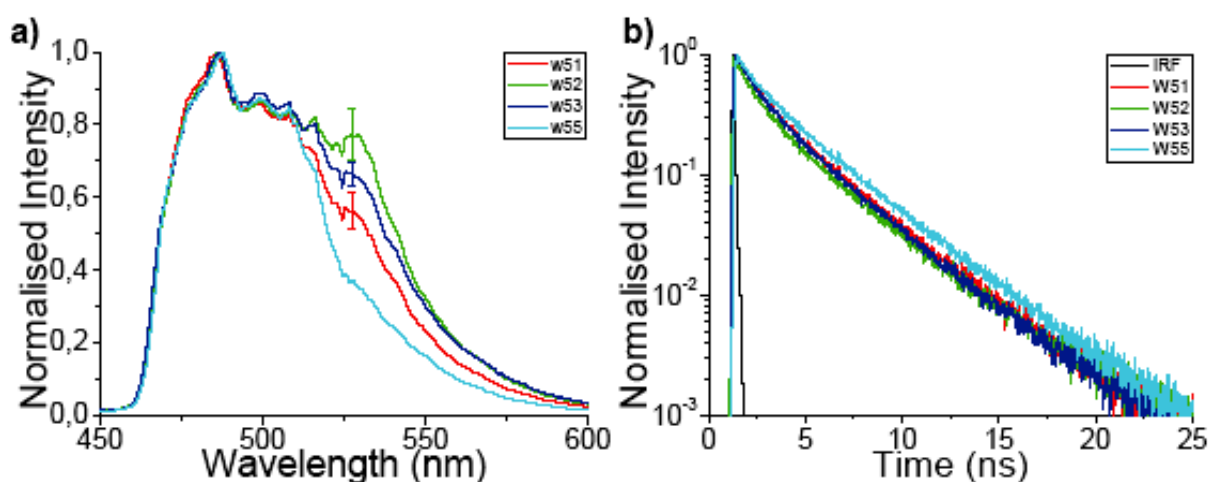


Figure 4.7) (a) Comparison of representative fluorescence emission spectra of W55 (cyan) with the FRET variants of Lck namely, W51 (red), W52 (green) and W53 (blue). The error bar for each curve at the EYFP emission maxima denotes the spread of fluorescence emission spectra for different constructs. For W55, it was less than 0.01. (b) Comparison of fluorescence intensity decays of control W55 (cyan) with the FRET variants W51 (red), W52 (green) and W53 (blue). The intensity decays of FRET variants were faster compared to ECFP. The fastest decay was detected in the case of W52, indicating best FRET efficiency. Intensity decays from W53 and W51 were similar, indicating a comparable FRET efficiency. Instrument Response function (IRF) is depicted in black.

4.2.2 Fluorescence dynamics of Lck FRET-control

In order to evaluate the fluorescence dynamics of ECFP fused to Lck as a donor, living Jurkat T cells expressing W55 construct (n=7) were measured. The fluorescence emission spectra yielded an emission maximum at 486 ± 1.02 nm (Figure 4.7 a) and the lifetime analysis, performed analogous to section 4.1, yielded two lifetimes of 3.37 ± 0.01 ns and 1.01 ± 0.03 ns (Figure 4.7 b). At the emission maximum of ECFP, the τ_1 and τ_2 showed contributions of $61\pm1\%$ and $39\pm1\%$ respectively, which resulted in a mean lifetime of 2.44 ± 0.02 ns (Table 4.3). The pre-exponential factors obtained for individual lifetimes were plotted along the wavelength to yield the DAS of ECFP. Comparison of the normalised DAS for both the lifetime components showed a similar pattern indicating that these originated from the same fluorophore (Figure 4.8 a). The fluorescence dynamics of CFP fused with Lck were corroborative with previous results in section 4.1 (Jose et al., 2007; Nair et al., 2006).

4.2.3 Fluorescence emission spectrum of Lck FRET variants

The different fusion constructs of Lck namely, W51, W52 and W53 (Figure 4.6), were used to study the intramolecular FRET. The emission spectra of the different constructs were plotted after normalising them at the ECFP peak (Figure 4.7 a). The ratios of intensity (R) at the EYFP emission peak (527.3 ± 1.02 nm) to the ECFP emission peak (486.4 ± 1.02 nm) were calculated for the different constructs. W52 showed highest R value of 0.76 ± 0.07 , whereas lowest R value of 0.58 ± 0.05 was observed for W51. Intermediate R value of 0.67 ± 0.03 was found for W53. These values were calculated from independent measurements not less than 6 transfected cells.

Table 4.3: Lifetimes and the percentage of contributions of each lifetime at ECFP emission maximum for different Lck variants expressed in Jurkat T cells

Construct	τ_1 [ns]	τ_1 [%]	τ_2 [ns]	τ_2 [%]	τ_3 [ns]	τ_3 [%]	τ_{mean} [ns]	n ^a
W51	3.43 ± 0.05	37 ± 5	1.32 ± 0.09	37 ± 2	0.22 ± 0.10	26 ± 3	1.82 ± 0.18	7
W52	3.42 ± 0.03	30 ± 3	1.24 ± 0.04	36 ± 3	0.14 ± 0.04	34 ± 5	1.53 ± 0.12	8
W53	3.38 ± 0.03	35 ± 2	1.40 ± 0.04	41 ± 2	0.21 ± 0.04	23 ± 3	1.83 ± 0.09	6
W54+W55	3.34 ± 0.04	59 ± 2	0.95 ± 0.08	41 ± 2	*	*	2.37 ± 0.05	6
W55	3.34 ± 0.01	61 ± 1	1.01 ± 0.03	39 ± 1	*	*	2.44 ± 0.02	7

^a number of independent measurements are denoted as n. The changes observed in the τ_{mean} of the FRET constructs were correlative with the proximity of CFP to the YFP molecule. The distance distribution between the fluorophores in W51 and W53 were similar. CFP in W52 was closer to YFP, compared to the other FRET constructs. The results suggested the folding of full-length Lck molecules to be such that the CFP in W52 is brought closer to the YFP, compared to W51 and W53.

4.2.4 Fluorescence lifetime dynamics of Lck FRET variants

The fluorescence lifetime analysis of Lck FRET variants were performed similar to the control CFP tagged Lck constructs analogous to section 4.2.1 (Figure 4.8). The different

lifetimes obtained and their corresponding contributions at the donor emission maximum are summarised in Table 4.3. An additional short lifetime τ_3 was observed in all the FRET constructs compared to the control W55. The fluorescence decays from living Jurkat T cells expressing the different FRET variants were fit with a three exponential model (as discussed previously in section 4.1.4). The lifetimes and their individual contributions at the donor emission maxima differed between the constructs (Table 4.3). Among the constructs, the maximum contribution of the τ_1 was observed for W51, with W52 showing the least. In addition, τ_3 contributed to a maximum for W52 in contrast to W51. τ_2 showed comparable contributions for the constructs. The multiple lifetimes for W53 were closer to W51, with respect to W52. This resulted in increased mean lifetimes for W51 and W53 compared to W52 (Table 4.3). The difference was also clear from the plots of the overall donor fluorescence decays of the different constructs (Figure 4.7 b). The fluorescence decays of all the FRET constructs at the donor emission maxima (483.8 ± 3.06 nm) were shorter compared to control W55, with W52 showing the shortest among them (Figure 4.7 b).

The acceptor decays of the FRET constructs were completely different from their corresponding donor dynamics. DAS showed small negative pre-exponential factors for the τ_2 in W52 and W53 near the emission maximum of EYFP (Figure 4.8 c and d). DAS of W51 at acceptor emission maximum displayed a minimum for the short lifetime components, indicating FRET (Figure 4.8 b). An increase in the contribution of the long lifetime component, τ_1 , and a subsequent reduction in the contribution of the two short lifetime components near the emission maximum of the acceptor were observed. Though W51 did not show negative pre-exponential factors at the acceptor emission maximum (Figure 4.8 b), the modelling of intensity decays with three exponentials were necessary, similar to W52 and W53. However, all the lifetimes showed a similar pattern in the donor emission region of the DAS which differed at the acceptor emission region, indicating an excited state reaction.

In section 2.3, with the aid of *equation (14)* it has been shown that the detection of the negative pre-exponential factors is dependent on the energy transfer efficiency and overlap of donor emission with that of acceptor emission. When the energy transfer efficiency is decreased or when there are more free donors, the possibility for obtaining negative contributions for lifetimes is decreased due to the overlap between ECFP and EYFP emission spectra. Even in the presence of the foresaid factors, analysis of DAS of FRET constructs revealed negative pre-exponential factors for lifetimes participating in FRET (τ_2 and τ_3) at the acceptor emission maximum.

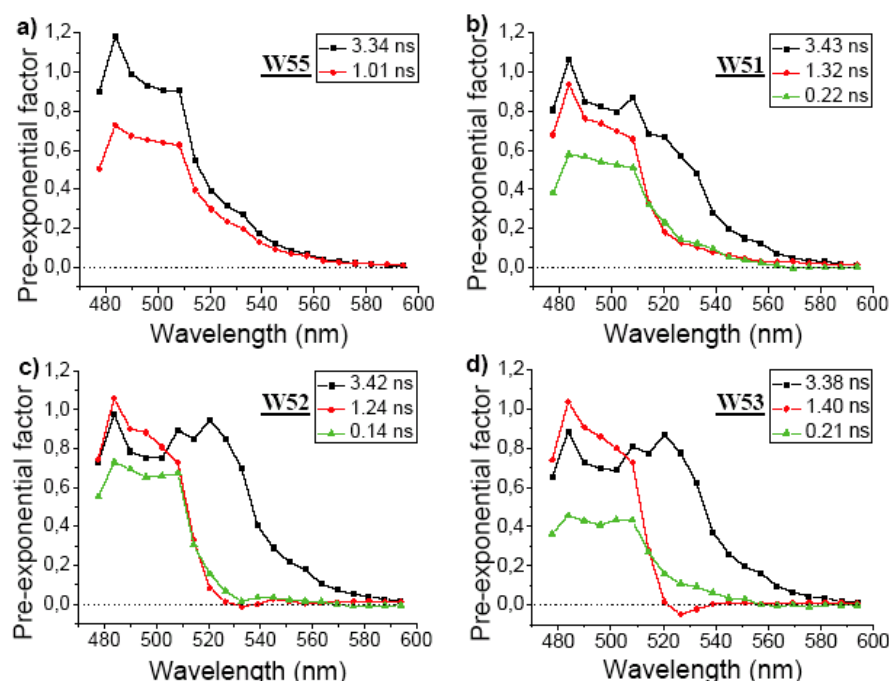


Figure 4.8) Comparison of Decay Associated Spectra of cells expressing different Lck variants with ECFP alone and with EYFP. (a) Decay Associated Spectrum of W55. (b-d) DAS for different FRET variants of Lck namely, W51 (b), W52 (c) and W53 (d) were different from that of W55. W52 and W53 showed small negative contributions for τ_2 of 2% and 10%, respectively at the acceptor emission maximum.

4.2.5 Intermolecular FRET in Lck

In order to confirm that the FRET observed was intramolecular and not intermolecular cells co-expressing Lck variants W54 and W55 were measured. The fluorescence emission spectra yielded an emission maximum at 486 ± 1.02 nm (Figure 4.9 a) and the lifetime analysis was performed similar to the W55 expressing cells. The deconvolution of intensity decays of co-expressing cells yielded two lifetimes of 3.34 ± 0.04 ns and 0.95 ± 0.08 ns (Table 4.3). At the emission maximum of ECFP, τ_1 and τ_2 showed contributions of $59 \pm 2\%$ and $41 \pm 2\%$, respectively, resulting in a mean lifetime of 2.37 ± 0.05 ns. Comparison of the DAS for both the lifetime components showed a similar pattern to the W55 expressing cells.

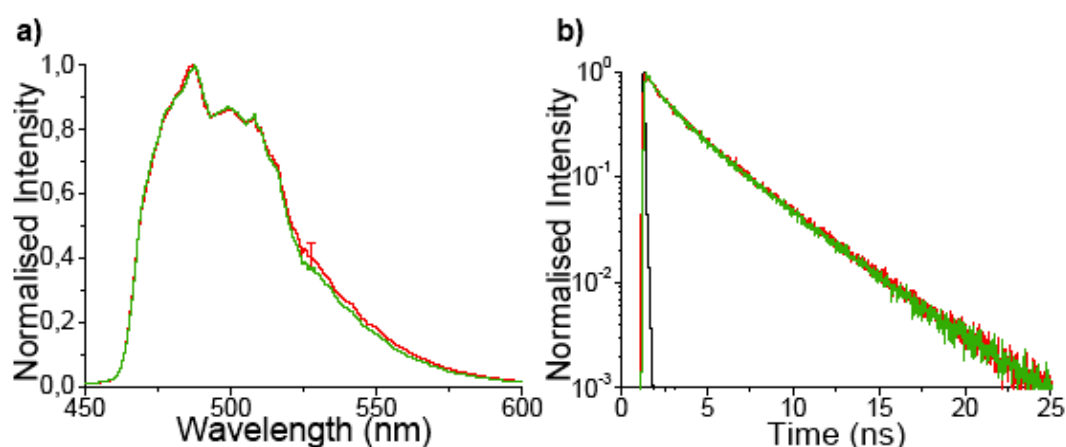


Figure 4.9) (a) Comparison of representative fluorescence emission spectra of W55 (green) and the cells co-expressing Lck W54 and W55 (red). The error bar for each curve at the EYFP emission maxima denotes the spread of fluorescence emission spectra for different constructs. For W55 it was less than 0.01 (b) Comparison of fluorescence intensity decays of W55 (green) and the cells co-expressing W54 and W55 (red) at the emission maximum of ECFP in a band of 483.8 ± 3.06 nm. Not much difference was found in the emission spectra or intensity decays denoting no or small FRET in the cells co-expressing W54 and W55.

Due to the absence of excited state reactions in cells co-expressing W54 and W55, the pre-exponential factors of all the lifetime components in the intensity decays remained positive. The co-expressing cells were modelled with two exponentials similar to the control, in contrast to the Lck FRET constructs, which had to be modelled with three exponentials (Table 4.3). The normalised emission spectra of cells co-expressing the donor and the acceptor revealed R values of 0.42 ± 0.04 , similar to W55 expressing cells of 0.37. The results confirmed the absence of FRET in cells co-expressing the variants of Lck fused with donor or acceptor alone, verifying the FRET in Lck constructs containing both donor and acceptor probes to be purely intramolecular.

The slight variability in lifetimes between the constructs (Table 4.3) indicated small intrinsic difference in the transfer rates, depending on the placement of the fluorophores in different constructs. The contribution of the pre-exponential factors at the donor emission maxima also differed between the constructs. Comparison of DAS of different constructs revealed the maximum contribution for τ_3 in W52, resulting in the lowest mean lifetime for the construct (Table 4.3). This would indicate a compact folding of the protein bringing the CFP placed between the SH2 and SH3 domain to the closest approach of YFP at the C-terminus, resulting in maximum FRET efficiency for this construct. This was in agreement with the FRET efficiencies calculated from the mean lifetimes of 37% for W52, which reduced to 25% for W51 and W53 as shown in Table 4.4.

Table 4.4: Energy transfer efficiency of different constructs of Lck^a

Construct	E τ_{mean} [%]	R
W51	25 \pm 5	0.58 \pm 0.05
W52	37 \pm 5	0.76 \pm 0.07
W53	25 \pm 2	0.67 \pm 0.03
W54+W55	3	0.42 \pm 0.04
W55	*	0.37

^a FRET efficiencies (E) were calculated from mean lifetimes of each construct, which were in direct relationship with R value calculated from the ratio of EYFP to ECFP peaks in the emission spectra of different tandem constructs. This confirms that CFP and YFP in W52 have better energy transfer efficiency compared to other constructs. W53 and W51 have similar FRET efficiency and the coexpressed sample the FRET is almost absent. This indicates that the FRET observed in Lck FRET constructs was purely intramolecular.

4.2.6 Real-time conformational changes of Lck upon T-cell receptor stimulation

Since W52 showed the highest FRET efficiency (Table 4.4), this construct was chosen to investigate real-time conformational changes of Lck upon T cell receptor stimulation. T cells expressing the FRET sample W52 (n=4) as well as the control w55 (n=3) were imaged continuously before (6 min) and after stimulation (20 min). Stimulation was done using

OKT3, an antibody for stimulating T-cell receptors (CD3). The data were split into periods (time frames), with each period corresponding to a real-time interval of 2 min. The data were analysed to detect any temporal changes in mean lifetimes at donor emission maxima, corresponding to differences in the conformation of the protein (Figure 4.10). The unstimulated cells exhibited no differences in the distribution of mean lifetimes (Figures 4.10 a and c). After CD3 stimulation, W55 containing ECFP alone showed only random fluctuations occurring due to continuous acquisition from a highly dynamic cell (Figure 4.10 b)

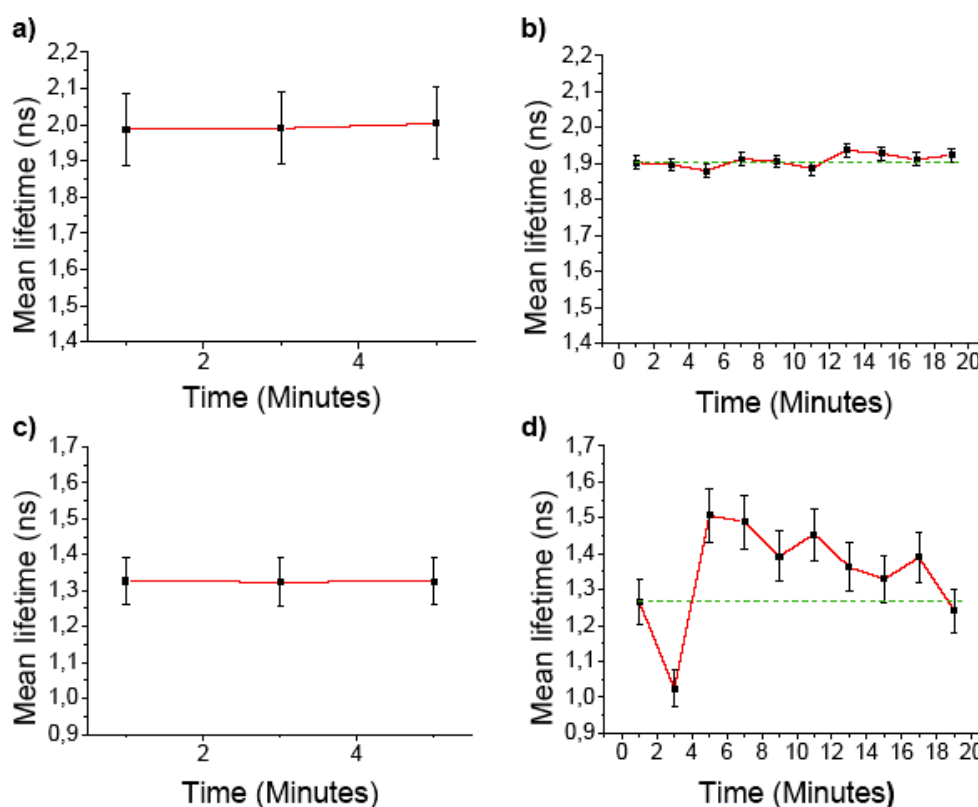


Figure 4.10). Real-time changes in the mean lifetime of different Lck constructs before and after T-cell receptor activation acquired by imaging detector. (a) Mean lifetime of a resting T-cell expressing W55. The data were acquired for 6 min and then analysed in frames of 2 min each. (b) Mean lifetime of a stimulated T-cell expressing W55. The green line indicates the basal lifetime. Mean lifetimes showed only random fluctuations upon stimulation. The cells were measured continuously for 20 min, each time frame corresponding to 2 min (c) The mean lifetime of resting T cells expressing W52 analysed in continuous frames of 2 min each (d) The mean lifetime of an activated T cell expressing W52 in response to soluble antigens. The green line indicates the basal lifetime. The mean lifetime of the stimulated cell increased in 5-7 min and returned to the basal lifetime in 17-20, min denoting a retrieval of FRET. The data acquisition and analysis were done similar to W55.

However, cells expressing the Lck FRET construct W52 displayed a significant increase in their mean lifetimes after antibody stimulation (Figure 4.10 d). This increase in mean lifetimes indicated a decrease in FRET efficiency in W52 during the first 5-7 min. The cells returned to basal FRET level in 17-20 min after the stimulation. The reduction in FRET during the initial time frames indicated a change in conformation of Lck bringing the

fluorophores apart, which returned to similar conformations as in unstimulated cells after 20 min.

4.2.7 Real-time conformational distribution of Lck upon contact with APC

To achieve deeper insights into the conformational changes of Lck, T cells expressing the Lck FRET construct W52 were presented with supra-antigen (SEE) presenting Raji cells. Real-time FLIM studies revealed changes in the fluorescence intensities as well as in the donor mean lifetimes of W52 at the contact sites between Jurkat T cells and SEE loaded Antigen presenting cells, indicating immunological synapses. The increase in donor mean lifetimes during the initial time frames of contact of T cells with APC (Figure 4.11, 4 min) indicated an opening up of conformation of Lck, during the initial moments of synapse formation.

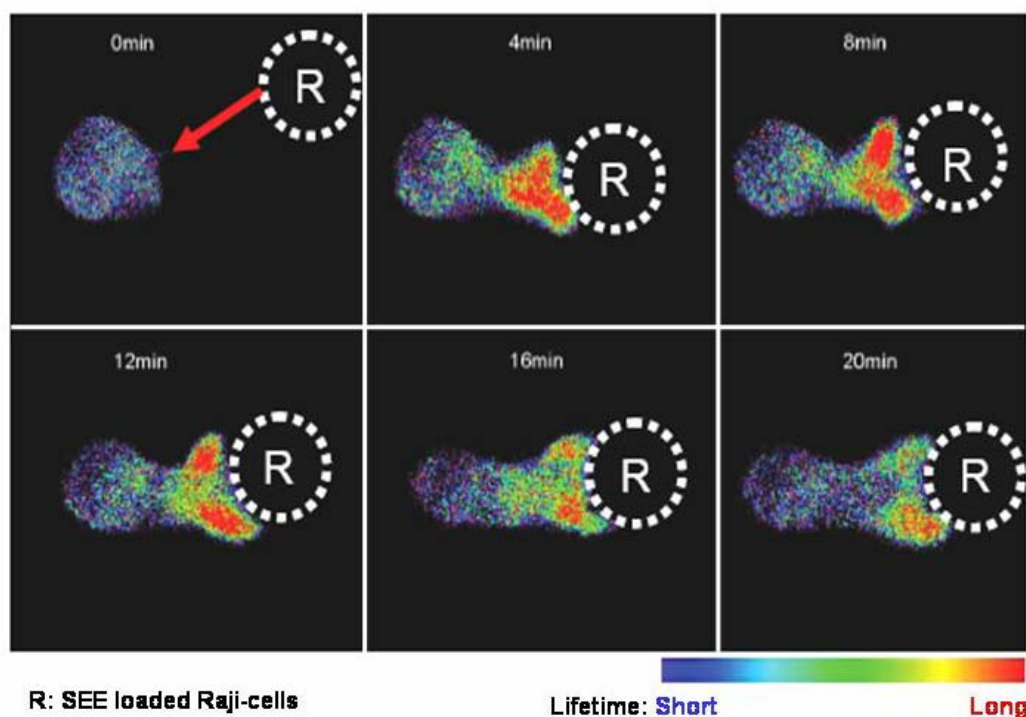


Figure 4.11) Pseudocolour images of real-time lifetime profiles of a W52 expressing cells upon contact with SEE presenting Raji cells (R). The data were acquired continuously by the imaging detector and split into six equal time frames. The images were colour coded with increase in mean lifetimes from blue to red. The longer lifetimes (red) indicated an open conformation for Lck, in contrast to the short lifetimes (blue) indicating a closed conformation.

At later time frames, Lck molecules in the possible open conformation resulting in longer donor mean lifetimes or reduced FRET efficiencies, were observed to concentrate on both sides of the cell-cell contact (Figure 4.1; 4, 8, 12 min). The results were in agreement with the existing hypothesis which describe the active form of Lck to be localised to the boundary of immunological synapses, at later time points of synapse formation (Dustin, 2003;

Holdorf et al., 2002). Similar to the stimulation with soluble antibodies, 20 min after the formation of the initial T cell-APC contact, short donor lifetimes of W52 were observed (Figure 4.11, 20 min). This suggested a closed conformation of Lck or a resulting low kinase activity of the protein at later stages of immunological synapse formation. Thus, it was possible to confirm the existing hypothesis that upon stimulation, the spatial and temporal changes in the kinase activity of Lck is closely linked to the structural changes of the protein.

4.3 Conformational dynamics of SH3-HOOK-GUK units of MAGUKs in COS7 cells

Conformational dynamics of the SH3-HOOK-GUK units of SAP90/PSD95 and SAP97/hDlg is regarded as a key mechanism regulating the near-membrane scaffolds during various cell-adhesion events, like formation of an immunological synapse. These conformational changes are supposed to be mediated by calcium-binding proteins like calmodulin which, could bind to the HOOK region of MAGUKs in response to the elevation of intracellular calcium (Masuko et al., 1999; Paarmann et al., 2002). Since the changes in intracellular calcium is very important biochemical event in the formation of immunological synapse, it was essential to gain precise knowledge on the calcium-dependent structural regulation of MAGUKs. The changes in fluorescence dynamics of the FRET variants of SH3-HOOK-GUK units were compared before and the elevation of intracellular calcium to address the foresaid aim.

4.3.1 Organisation of GFPs in SH3-HOOK-GUK module

SH3-HOOK-GUK unit of different MAGUKs was fused with CFP at the N-terminus and YFP at the C-terminus (CFP-SH3-HOOK-GUK-YFP). Living COS7 cells expressing these constructs were stimulated by Thapsigargin to permanently elevate the intracellular calcium levels. An inhibitor of calmodulin, W7 (will be referred as inhibitor^{W7}) was used to disrupt the possible association between calmodulin and MAGUKs in stimulated cells. As a FRET control, a construct that express CFP alone at the N-terminus (CFP-SH3-HOOK-GUK) was used. In this study, the vectors containing SH3-HOOK-GUK units of SAP97/hDlg and SAP90/PSD95 were referred to as SAP97^{FRET} and PSD95^{FRET}, respectively. For the FRET control, only the SAP90/PSD95 was used and was referred to as PSD95^{FRET control}. Fluorescence dynamics of this constructs were collected by using the point detector. The changes in spectra, lifetimes, and DAS were compared between the constructs.

4.3.2 Fluorescence dynamics of the PSD95^{FRET control}

Fluorescence dynamics of CFP fused to SH3-HOOK-GUK unit of MAGUKs were measured from living COS7 cells expressing PSD95^{FRET control} (n=6) The fluorescence

emission spectra yielded an emission maximum at 486 ± 1.02 nm and lifetime analysis was performed analogous to the section 4.1.1. The results are summarised in Table 4.5. These results were consistent with previous reports of CFP expressed in living cells (Jose et al., 2007; Nair et al., 2006) and CFP fused to Lck(W55). This confirms that the ECFP in the PSD95^{FRET control} was not perturbed due to the characteristics of the fusion protein.

4.3.3 Fluorescence dynamics of the FRET constructs in COS7 cells

The FRET variants of the MAGUKs, PSD95^{FRET} (n=6) and SAP97^{FRET} (n=6) were used to study the variability of intramolecular FRET in unstimulated and stimulated cells expressing these constructs. The emission spectra of the different constructs were plotted after normalising them at the CFP peak. The ratios of intensity (R) at the YFP emission peak (527.3 ± 1.02 nm) to the ECFP emission peak (486.4 ± 1.02 nm) were calculated for the different constructs (Figure 4.12 and 4.13)

Table 4.5: Lifetimes and the percentage of contributions of each lifetime at ECFP emission maximum for different SH3-HOOK-GUK fusion constructs expressed in COS7 cells

Construct	τ_1 [ns]	τ_1 [%]	τ_2 [ns]	τ_2 [%]	τ_3 [ns]	τ_3 [%]	τ_{mean} [ns]	n
FRET control	3.26 ± 0.02	58 ± 2	0.99 ± 0.04	42 ± 2	*	*	2.32 ± 0.02	6
SAP90/PDS95								
unstimulated	3.24 ± 0.01	41 ± 1	1.36 ± 0.05	36 ± 1	0.44 ± 0.06	24 ± 1	1.90 ± 0.02	6 [#]
Stimulated	3.15 ± 0.02	35 ± 1	1.37 ± 0.08	40 ± 1	0.41 ± 0.09	24 ± 1	1.76 ± 0.05	
SAP97/hDlg								
unstimulated	3.25 ± 0.01	42 ± 1	1.23 ± 0.07	33 ± 3	0.28 ± 0.05	24 ± 4	1.86 ± 0.02	6 [#]
Stimulated	3.15 ± 0.01	40 ± 2	1.19 ± 0.02	36 ± 1	0.27 ± 0.01	24 ± 2	1.75 ± 0.06	

[#]) indicates that the fluorescence dynamics of the same cells were compared before and after stimulation. After stimulation with Thapsigargin mean lifetimes of the constructs seemed to decrease indicating a calcium-dependent change in the conformation of the SH3-HOOK-GUK units of SAP97 and PSD95. The mean lifetimes, multiexponential lifetimes, and their contributions suggest that FRET has increased with elevation of intracellular calcium.

4.3.4 Fluorescence dynamics of PSD95^{FRET}

The lifetime analysis was consistent with the analysis presented in the previous sections (sections 4.1 and 4.2). The intensity decays of CFP from unstimulated cells expressing PSD95^{FRET} were modelled with three lifetimes compared to FRET control indicating FRET. The decay at the CFP emission maximum of PSD95^{FRET} was observed to be faster after stimulation with Thapsigargin denoting an increase in FRET efficiency. The lifetimes and their contribution at the CFP emission maximum are summarised in Table 4.5 before and after stimulation. An example of the data acquired from a single cell is presented in Figure 4.12. These results revealed a calcium-dependent conformational change for PSD95^{FRET}.

Table 4.6: Efficiency of energy transfer occurring from ECFP of different FRET constructs

Construct	$E \tau_{\text{mean}}$ [%] unstimulated	$E \tau_{\text{mean}}$ [%] Stimulated	$\Delta E \tau_{\text{mean}}$ [%]	R_{initial} unstimulated	R_{final} Stimulated	ΔR [%]
SAP90/PSD95	18±2	24±2	33±2	0.66±0.08	0.83±0.11	27±5
SAP97/hDlg	20±1	25±3	25±2	0.62±0.05	0.80±0.09	26±5

The increase of FRET efficiencies (E) were calculated from mean lifetimes of each construct which were in direct relationship with R value calculated from the ratio of YFP to CFP peaks in the emission spectra of different tandem constructs. $\Delta E \tau_{\text{mean}}$ is the percentage of increase of efficiency of energy transfer calculated as $\Delta E \tau_{\text{mean}} = [E \tau_{\text{mean}}(\text{Stimulated}) - E \tau_{\text{mean}}(\text{Unstimulated})] * 100 / E \tau_{\text{mean}}(\text{Unstimulated})$. ΔR is the percentage of increase of YFP enhancement calculated as $\Delta R = [R_{\text{final}}(\text{Stimulated}) - R_{\text{Initial}}(\text{Unstimulated})] * 100 / R_{\text{Initial}}(\text{Unstimulated})$.

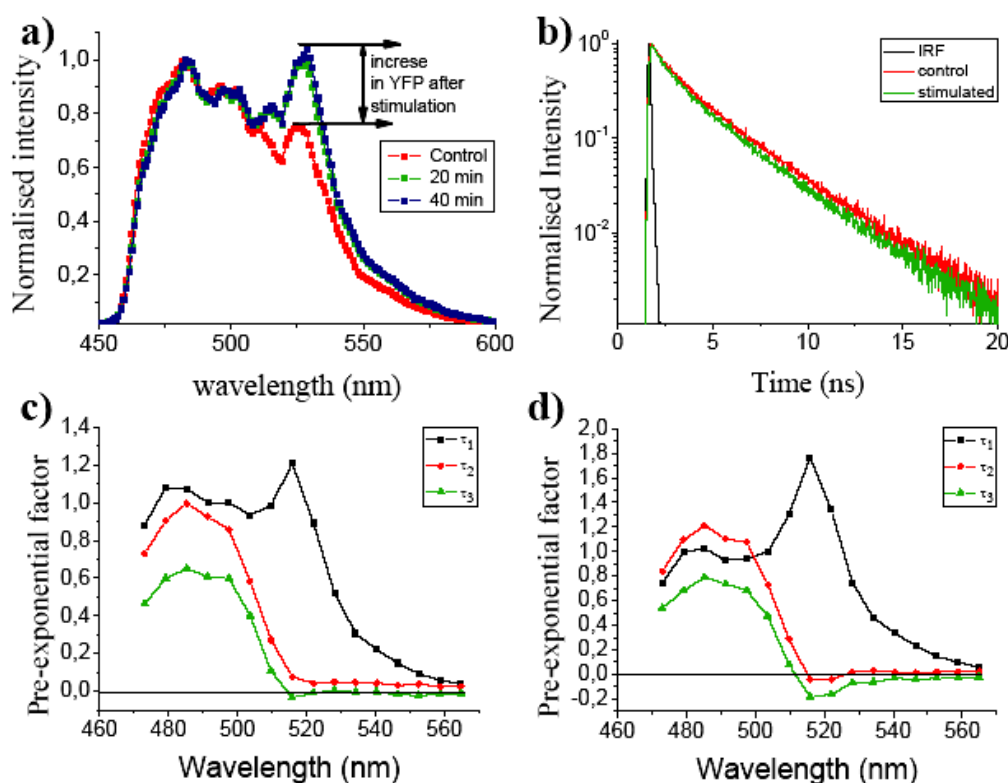


Figure 4.12) a) Comparison of fluorescence emission spectra of PSD95^{FRET} construct expressing COS7 cell. The emission spectra of the resting cell (red) and stimulated cell at time points of 20 min (green) and 40 min (blue). The increase in YFP was saturated by 20 min with no further increase in time. b) The intensity decays of PSD95^{FRET} construct at the CFP emission maximum before (red) and after (green) the stimulation. Instrument response function is depicted in black. The intensity decay after the stimulation was observed to be faster indicating better FRET c) DAS of the PSD95^{FRET} construct from unstimulated cell d) DAS of PSD95^{FRET} construct after stimulation. After stimulation at the acceptor emission peak pre-exponential factors τ_2 and τ_3 were negative indicating an increase in FRET after stimulation. τ_1 τ_2 τ_3 of PSD95^{FRET} before and after stimulation is summarised in Table 4.5.

The fluorescence emission spectra of the unstimulated cells expressing the PSD95^{FRET} in COS7 cells showed an R value of 0.66±0.08. Incubation with Thapsigargin resulted in an increase of R value to 0.83±0.11 indicating an increase in FRET after the elevation of intracellular calcium. An increase of 27±5% in YFP emission was observed, which could be due to increase in FRET efficiency (Table 4.6). No drastic change in fluorescence dynamics of the FRET construct was observed, on incubation with inhibitor^{w7}, before and after

stimulation indicating that the changes in PSD95^{FRET} construct was a calcium-regulated process (Figure 4.14 a and b).

4.3.5 Fluorescence dynamics of SAP97^{FRET}

Similar to PSD95^{FRET}, intensity decays of SAP97^{FRET} were faster than FRET control. The decays were modelled with three lifetimes indicating the presence of an energy transfer. The lifetimes and their contribution at the CFP emission maximum before and after stimulation are summarised in Table 4.5. These results indicated a calcium-dependent conformational change for the SAP97^{FRET} construct similar to the PSD95^{FRET} construct. An example of the data acquired from a single cell is presented in Figure 4.13.

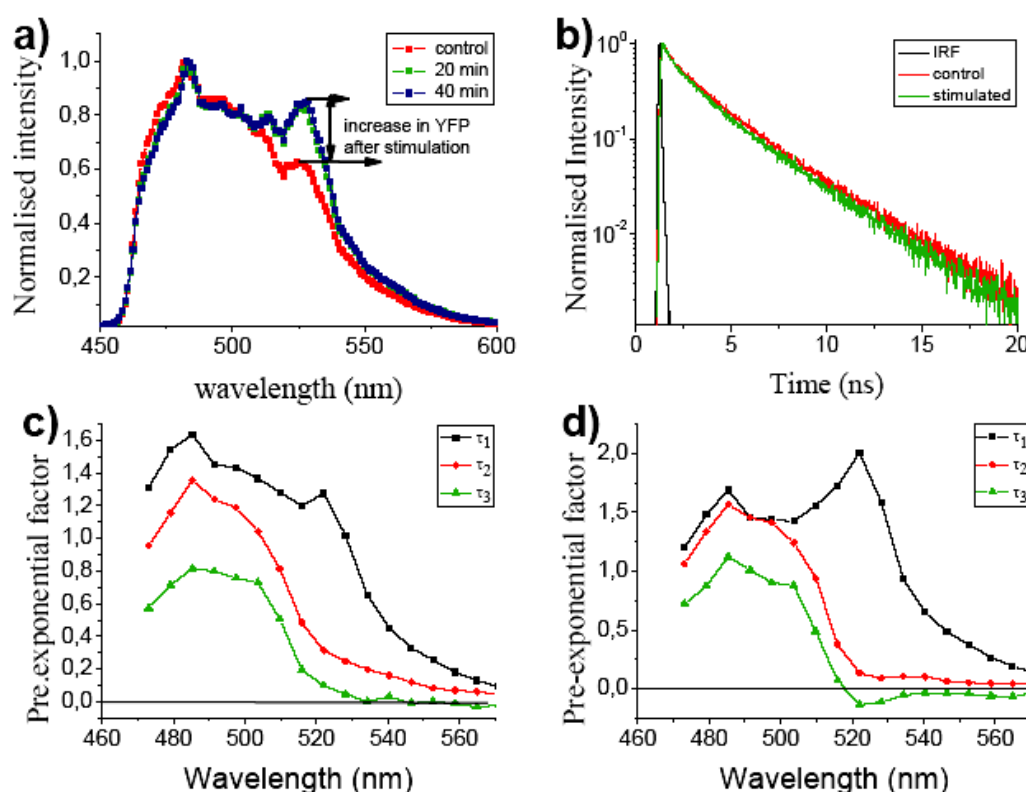


Figure 4.13) a) Comparison of fluorescence emission spectra of SAP97^{FRET} construct in unstimulated and stimulated cell. The emission spectra of the resting cell (red) and stimulated cell at time points of 20 min (green) and 40 min (blue). The increase in YFP was saturated by 20 min. b) The intensity decays of SAP97^{FRET} construct at the CFP emission maximum before (red) and after (green) the stimulation. Instrument response function is depicted in black. Intensity decay after the stimulation was observed to be faster indicating better FRET (c) DAS of the SAP97^{FRET} constructs d) DAS of SAP97^{FRET} constructs after stimulation. After stimulation at the acceptor emission peak pre-exponential factors of τ_3 was observed to be negative indicating an increase in FRET after stimulation. τ_1 τ_2 τ_3 of SAP97^{FRET} before and after stimulation is summarised in Table 4.5.

In contrast to the case without inhibitor^{W7}, a change in fluorescence dynamics of the SAP97^{FRET} construct was not observed before and after stimulation indicating that, the conformational change observed was a calcium-regulated process (Figure 4.14 c and d). These studies confirm that conformational changes in SAP97/hDlg are calcium and calmodulin dependent.

The fluorescence emission dynamics of SAP97^{FRET} constructs were investigated similar to the PSD95^{FRET} constructs (Figure 4.13). The fluorescence emission spectra of the resting COS7 cells expressing the SAP97^{FRET} construct showed an R value of 0.62 ± 0.05 . Incubation with Thapsigargin resulted in an increase of R value to 0.80 ± 0.09 indicating an increase in FRET efficiencies after the elevation of intracellular calcium (Table 4.6). This resulted in an increase of R value by $26 \pm 5\%$ similar to PSD95^{FRET}.

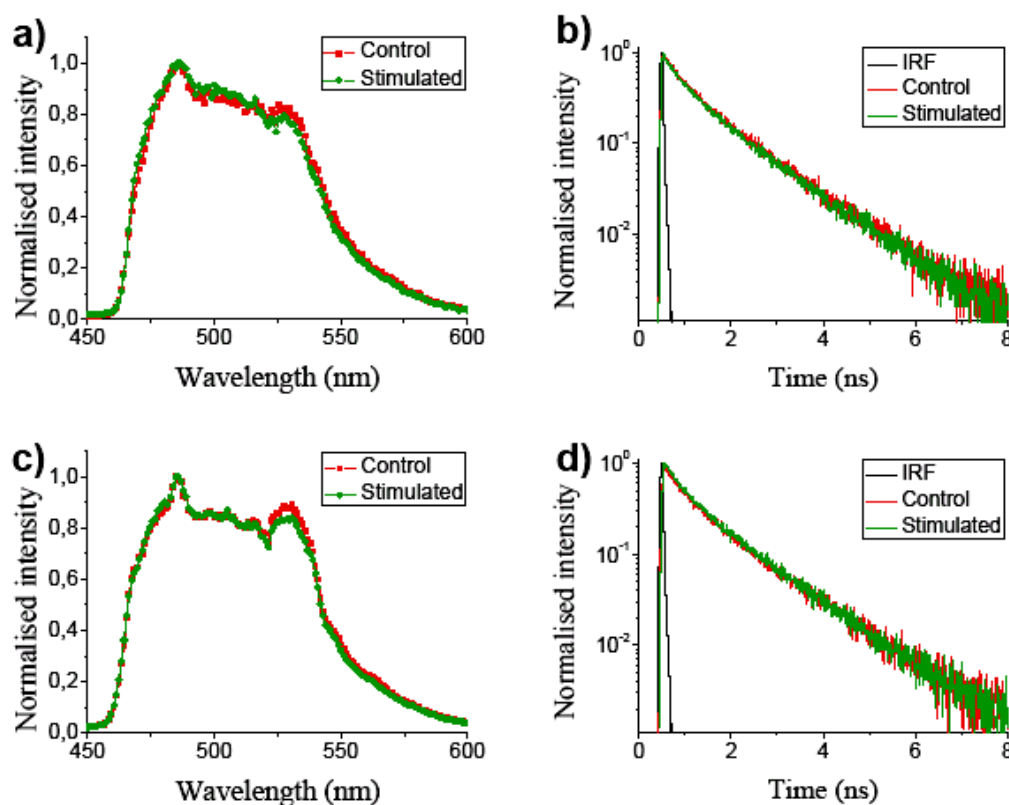


Figure 4.14) The fluorescence dynamics of PSD95^{FRET} and SAP90^{FRET} after incubation with calmodulin inhibitor. The cells were incubated with inhibitor^{w7} before and during stimulation. a) Fluorescence emission spectra of PSD95^{FRET} construct before (red) and after stimulation (green) b) Intensity decays of PSD95^{FRET} before (red) and after stimulation (green) c) Fluorescence emission spectra of SAP90^{FRET} construct b before (red) and after stimulation (green) d) Intensity decays of SAP90^{FRET} before (red) and after stimulation (green). Fluorescence dynamics were similar before and after stimulation in both the MAGUKs in contrast to the case without calmodulin inhibitor.

FRET-FLIM studies showed that SH3-HOOK-GUK units were in a compact conformation in unstimulated cells. This indicated the possibility of intramolecular association of MAGUKs, keeping them in a closed conformation in unstimulated cells. These conformations of SH3-HOOK-GUK unit of SAP97/hDlg and SAP90/PSD95 were dependent on intracellular calcium levels. In the presence of elevated calcium, both constructs responded with changes in fluorescence emission dynamics. Blocking of the calmodulin activity abolished these changes indicating the response of SH3-HOOK-GOOK units to calcium was regulated by the activity of calcium sensor calmodulin (Figure 4.14).

4.4 Relevance of alternative splicing of insertion I1 in SAP97/hDlg in Jurkat T cells

The formation of immunological synapse is followed by recruitment of several cytoplasmic adaptor proteins which can be involved the modifications of cytoskeleton. Many of these proteins affecting the actin dynamics have been found to contain SH3 domain (Torres and Rosen, 2006). I1 spliced insertion in SAP97/hDlg harbours several proline-rich motifs which can potentially associate with multiple SH3 domain containing proteins. Biochemical studies have pointed out an interaction between SH3 domain of Lck and I1 region of SAP97/hDlg in lymphocytes (Hanada et al., 1997). Here, with the help of novel microscopy methods, the relevance of I1 and its interaction to Lck is addressed by observing the differences in localisation of various isoforms of SAP97/hDlg in T-lymphocytes.

4.4.1 Distribution of I1 (I1A and I1B) insertions of SAP97/hDlg in Jurkat T cells.

MAGUKs like SAP97 can occur in various isoforms due to alternative splicing of encoding transcripts. An insertion, termed I1, is located between the N-terminus and the PDZ repeat RT-PCR confirmed the presence and distribution of I1 isoforms in T cells. RT-PCR on total RNA of Jurkat T cells was performed to identify the I1 splicing in hDlg (Figure 4.15).

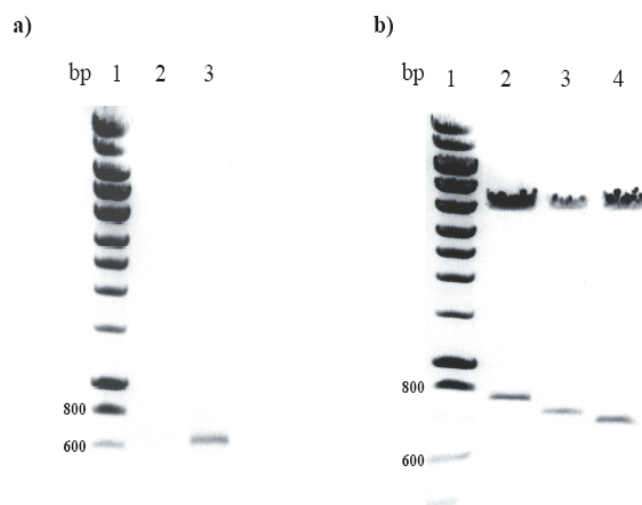


Figure 4.15) Distribution of insertions I1A and I1B isoforms in Jurkat T cells. a) cDNA fragments of N terminal part of SAP97/hDlg were generated by reverse transcription from total RNA extracts from Jurkat T cells. A PCR product was detected in a band between 800 and 600 base pairs. In the figure, lane1 indicated the marker, lane2 indicate the control where PCR was performed without RNA template, and Lane 3 denotes PCR product. b) The PCR products were cloned into Topo-TA cloning vectors, transformed into bacteria and random colonies were selected. Purified DNAs were sequenced and selected plasmid DNAs were cut with EcoR1. Different splice forms were observed as bands between 800 to 600 base pairs. Lane 1 indicates the marker, lane 2 indicates the presence of both I1 splicing I1A and I1B, lane3 indicate I1B and in lane4 represent the absence of I1 splicing. I1A alone was not detected.

PCR amplification of cDNA molecules was used to analyse all combinations of I1A and I1B insertions found in hDlg transcripts from human Jurkat T cells. Transcripts containing I1A and I1B together (I1A + B), I1B without I1A (I1B), and neither I1A nor I1B (Δ I1) were identified. PCR products containing I1A but lacking I1B (I1A) were not detected from the template. However, these results were consistent with previous studies that reported I1A to be barely detectable in other cell types (McLaughlin et al., 2002). Earlier studies indicated that I1A was detected in brain after a 30-cycle PCR reaction but not after a 20-cycle

PCR (McLaughlin et al., 2002). This suggested that the transcript coding for I1A alone is present only in low amounts in brain and other tissues.

4.4.2 Subcellular localisation of endogenous SAP97/hDlg in Jurkat T cells

To explore the possible role of SAP97/hDlg in T-Lymphocytes, the distribution of endogenous protein was analysed in unstimulated and stimulated T cells. A protocol was adopted for generating surrogate formation of immunological synapse by incubation of Jurkat T cells with beads coupled to anti-CD4 and anti-CD28 antibodies. Antibody cross-linked beads presented to T-cells were reported to be a valid system for observing the subcellular distribution of PDZ domain containing proteins (Ludford-Menting et al., 2005; Xavier et al., 2004). These beads were used to study the formation of mock immunological synapse to evaluate the reorganisation of endogenous proteins after exposure to agonistic stimuli. In unstimulated cells, the endogenous protein is distributed in the cytoplasm.

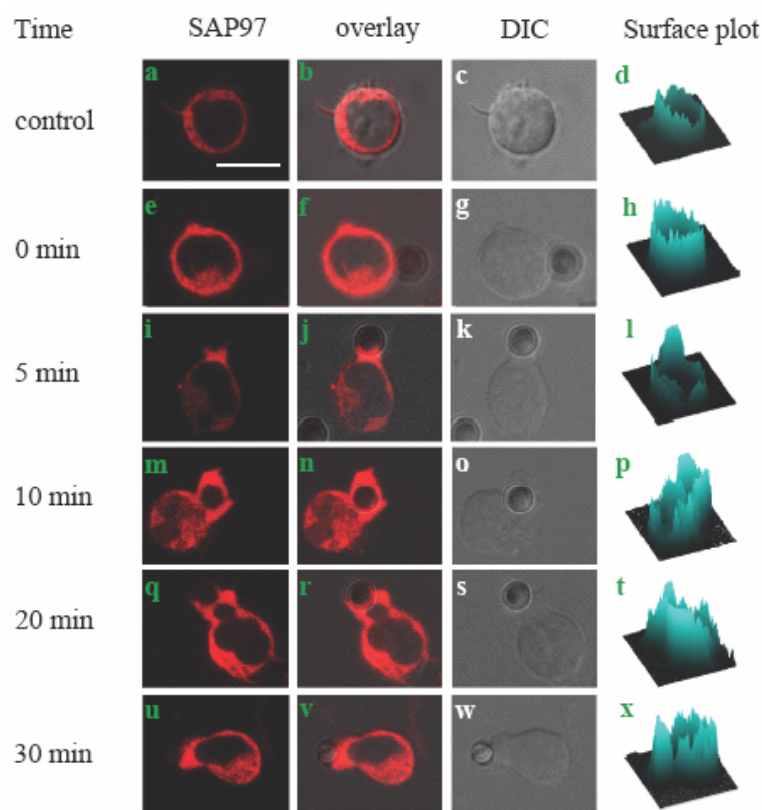


Figure 4.16) Translocation of endogenous SAP97/hDlg to the cell-bead interface in Jurkat T cells. Figures e, i, m, q and u denotes the subcellular distribution of SAP97/hDlg at different time points from formation of cell-bead contact. Figure a is the control unstimulated cell. Figures c, g, k, o, s and w indicate the corresponding differential interference contrast images. Figures b, f, j, n, r, and v are the overlay images. Figures d, h, l, p, t and x display the corresponding surface plots of the fluorescent images. Surface plots of unstimulated cells and cells which at the starting of stimulation indicated a homogeneous distribution of fluorescence (d,h). It could be observed that within 5 min (l) of the contact, there was a translocation of fluorescence to the cell-bead interface indicated by the increased fluorescence intensity compared to rest of the membrane. The fluorescence intensity at the cell bead contact decreased with time after the formation of cell-bead contact (p,t). At 30 min (x), fluorescence in the cell body and cell bead interface was nearly the same indicating a redistribution of proteins as in the resting cells. The images were acquired in a single plane using a confocal microscope. Scale bar indicates 10 μ m.

As displayed in Figure 4.16 upon contact with the beads endogenous SAP97/hDlg was recruited to the membrane caps. This was observed by the higher level of fluorescence at the cell-bead contact compared to the other parts of the cell body. 30 min after the stimulation the fluorescence in the cell-bead contact and the cytoplasm was nearly the same indicating a redistribution of proteins as in the unstimulated cells. However, it was observed that even after 30 min the fluorescence at the cell bead contact persisted indicating that a fraction of SAP97/hDlg molecules are still present at the cell-bead interface. This would indicate the possibility that a pool of the recruited proteins can be tightly associated with the near-membrane matrix. This pool could be involved in regulating scaffolds which is essential for maintaining a stable contact between the bead and the cell. This data is in agreement with previous reports suggesting an activity-dependent increase of hDlg towards the T cell-bead contact and T cell-APC contact at 5 min after stimulation (Xavier et al., 2004).

4.4.3 Localisation of I1-containing isoforms to the cell-bead contact

Presence of multiple proline-rich motifs on SAP97/hDlg, I1 domain, was shown to interact with the SH3 domain of Lck in Jurkat T cells (Hanada et al., 1997). Interestingly previous reports showed that Lck translocates to the immunological synapse in 5 min after the initial contact is made and then redistributes to the resting level localisation in 30 min time after the formation of immunological synapse (Ehrlich et al., 2002; Holdorf et al., 2002). To investigate the potential role of I1 splicing GFP-tagged SAP97/hDlg splice isoforms were observed in unstimulated and T cells making contact with antibody coated beads. Stimulation was done similar to section 4.4.2 by presenting anti-CD4 and anti-CD28 antibody coupled beads to Jurkat cells.

GFP tagged SAP97/hDlg isoforms (see Figure 1.6) containing I1 and I2 splicing (referred as I1-I2 SAP97/hDlg), I1 and I3 splicing (referred as I1-I3 SAP97/hDlg) and I3 splicing alone (referred as I3 SAP97/hDlg) were expressed in Jurkat cell lines Jurkat E6.1 and JCaM 1.6 to study the distribution of the protein in the presence and absence of Lck (Figure 4.17). Results showed that cells expressing the construct containing I1 splicing (I1-I2 SAP97/hDlg, I1-I3 SAP97/hDlg) translocated to the cell-bead interface in 5 min similar to the distribution of endogenous SAP97/hDlg in Jurkat E6.1 cells. The isoforms lacking I1 splicing (I3 SAP97/hDlg) was not translocated to cell-bead interface in Jurkat E6.1 cells (Figure 4.17). The molecular involvement of Lck was verified using JCaM 1.6 cell line deficient in Lck. In these cells, the presence of I1 isoform did not facilitate the recruitment of I1-I3 SAP97/hDlg to the cell-bead interface. This indicated that Lck might be important in the subcellular localisation of SAP97/hDlg .

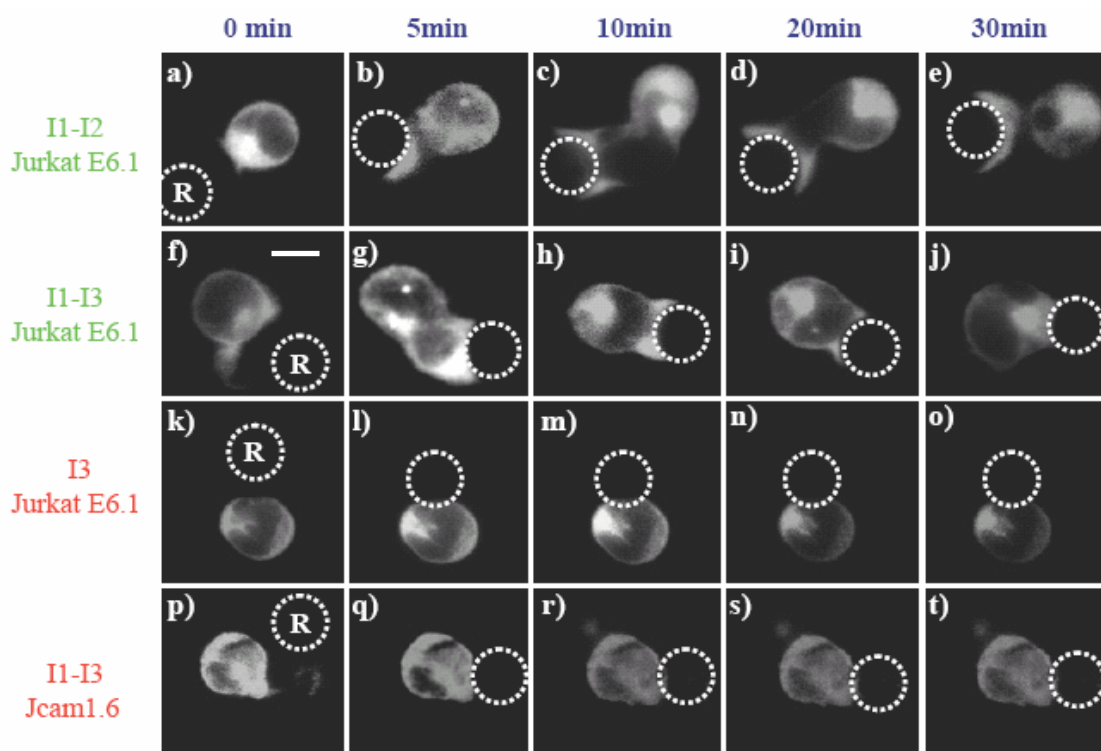


Figure 4.17) Translocation of GFP tagged isoforms of SAP97/hDlg to the cell-bead interface. The left side indicate the combination of the isoforms in the fusion constructs and the Jurkat cell line used. The antibody-coated beads are shown as dotted circles marked as R. The images were acquired using a video microscope at different time intervals as indicated on the top of the Figure. a-e) The changes in fluorescence distribution of GFP I1-I2 SAP97/hDlg expressed in Jurkat E6.1 cells. f-j) The changes in fluorescence distribution of GFP I1-I3 SAP97/hDlg expressed in Jurkat E 6.1 cells. k-o) The changes in fluorescence distribution of GFP I3 SAP97/hDlg expressed in Jurkat E 6.1 cells. p-t) The changes in fluorescence distribution of GFP I1-I3 SAP97/hDlg expressed in JCaM 1.6 cells. The I1 containing isoforms, GFP I1-I2 SAP97 and GFP I1-I3 SAP97/hDlg, translocated to cell-bead contact immediately after the contact with the bead. Interestingly the absence of I1 domain (Figures k-o) or the absence of endogenous Lck (JCaM 1.6 cells) in the cells (Figures p-t) disrupted the localisation of SAP97/hDlg to the cell-bead interface. Scale bar indicates 10 μ m.

I1 isoforms are proposed to bind multiple SH3 domain containing proteins (McLaughlin et al., 2002). A number of SH3 domain containing proteins are known to interact with N-WASP, a main mediator for actin polymerisation (Torres and Rosen, 2006). Previous studies indicated that SAP97/hDlg and N-WASP could be involved in a multimeric complex (Round et al., 2005). The set of experiments performed in this section indicated that I1 containing isoforms might be essential for the localisation at membrane caps, where polymerised actin seemed to be enriched. There are different ways for MAGUKs to be translocated to the immunological synapse. Interaction of MAGUKs with 4.1-like proteins play a vital role in deciding the localisation of MAGUKs (Hanada et al., 2003). Alternatively I1 can provide a completely different mechanism for near-membrane localisation of cytoplasmic and membranous pools of SAP97 to immunological synapse. Thus it can be part of multiple signalling complexes stabilising a nascent immunological synapse.

5 DISCUSSION

Fluorescence resonance energy transfer in combination with lifetime imaging is a very sensitive approach to comprehend subtle changes in macromolecular association and dissociation. A new approach of FRET –FLIM studies (as discussed in chapter 2) was used to address these small changes directly from living cells. The excited state energy transfer from ECFP to EYFP was studied at picosecond time resolution and nanometer spectral resolution in the time domain using Fluorescence Lifetime Micro-Spectroscopy (FLMS). The sensitivity of this approach was checked using tandem constructs of Clomeleon, where the distance between donor and acceptor fluorophores were varied in steps of 8 aa. The simultaneous detection of fluorescence lifetimes at high temporal resolution as a function of wavelength and fluorescence emission spectra was used to understand the photophysics of FRET from multiple conformations of CFP to Topaz. These insights in to the photophysics of the system were used to verify the structure of the multidomain domain proteins Lck, SAP97/hDlg and SAP90/PSD95 in unstimulated and stimulated cells.

5.1 FRET as excited state reactions

It was essential to gain insights in to the photophysics of CFP before investigating how it could take part in FRET. The fluorescence decays of ECFP were modelled with two exponentials, well in agreement with previous works (Borst et al., 2005; Duncan et al., 2004; Tramier et al., 2004). Calculation of FRET efficiencies using mean lifetimes indicated a decrease in efficiency with increase in spacer lengths (Table 4.2). The spacers between the fluorophores were changed in steps of eight amino acids, and with the help of the FLIM-FLMS system in combination with global analysis the differences between these constructs were detected. The analysis of mean lifetimes along the spectrum showed a significant reduction for the donor with a corresponding increase in the mean lifetimes of the acceptor due to the occurrence of an energy transfer. Further analysis of the control acceptor decays was not possible because of the lack of direct excitation of Topaz in the experimental setup.

The negative amplitudes of the pre-exponential factors at the Topaz emission maximum indicated that the energy transfer caused the excitation of the Topaz from CFP rather than the direct excitation by the laser pulse. This was confirmed by coexpressing ECFP and Topaz molecules where the DAS showed only positive amplitudes for all the lifetimes indicating the absence of energy transfer. The mean lifetimes obtained in this case were similar to the control ECFP indicating that fluorescence emission characteristics of CFP was not perturbed in the presence of acceptor molecules when they were not within the Foerster radius. The direct excitation of acceptor at 420 nm gave a multiexponential decay well in

agreement with previous reports where excitation of YFP in solution at 400 nm showed a fast multiexponential decay at shorter wavelengths (440 nm) in contrast to its monoexponential character at higher excitation wavelengths (560 nm) (Habuchi et al., 2002; Jose et al., 2007). This was attributed to the excitation of the protonated band of YFP. The multiexponential decays of the acceptor in cells could arise due to autofluorescence as well. Excitation with 420 nm, resulted in less than 5% excitation for YFP, while the flavin molecules were excited more than 70% (Holzer et al., 2002). The DAS obtained from YFP analysis in cells showed that the origin of fluorescence of short lifetimes were different from the longest emitting species. The short lifetimes observed were proposed to be originating from autofluorescence molecules and the long lifetime from the deprotonated species of YFP.

5.1.1 Kinetic model of FRET from a two state donor to single state acceptor

DAS of the tandem FRET constructs indicated the involvement of two short lifetimes in energy transfer, which could arise from the two conformational states of the CFP molecule. Since CFP is biexponential, it was expected to have at least four lifetimes in the intensity decay when involved in energy transfer. Here, it was possible to fit the intensity decays of FRET constructs with a three exponential model. It should be noted that τ_2 involved in energy transfer was very close to the short lifetime of the unperturbed donor (Table 4.1). Consequently, deconvoluted τ_2 of the FRET sample (Table 4.1) could be a mix of a FRET lifetime and an unperturbed donor lifetime resulting in a three exponential fit. The acceptor is regarded to have monoexponential decay when excited at the deprotonated band, whereas the protonated form is considered not to be involved in energy transfer. Due to the overlap of fluorescence emission of CFP with the absorption of the deprotonated band of YFP (Habuchi et al., 2002), the monoexponential nature of YFP is perturbed when participating in energy transfer as an acceptor. If both conformations of CFP take part in energy transfer, it may yield two different transfer rates resulting in two lifetimes displaying negative pre-exponential factors at the acceptor emission maximum. Consequently, a three exponential fit was performed for both donor and acceptor decays involved in energy transfer. For the FRET constructs, short lifetime components (τ_2 and τ_3 , Table 4.1) showed negative pre-exponential factors in intensity decays near the Topaz emission maximum, which implied that these conformations of CFP could individually be involved in energy transfer. Though the control had to be fit with different multiexponential models (Table 4.1), the negative pre-exponential factor or the rise time in the intensity arose only due to excited state reaction between different fluorophores (Davenport et al., 1986; Lakowicz, 1999).

In Jurkat T cells, CFP was modelled with two exponentials consistent with the kinetic model predicted for CFP (Tramier et al., 2004). The current experimental approach allowed to predict a kinetic model of energy transfer occurring from CFP to Topaz (Figure 5.1). Two different fluorescent species, A and B, could exist for CFP. The difference in the excitation spectra (Tramier et al., 2004) of these two species could give rise to the emission maximum (486 nm) and a red shifted shoulder (505 nm) in the emission spectrum of CFP. It is hypothesised that the two excited state species A^* and B^* can return to an equilibrium via an intermediate excited state species I^* (Tramier et al., 2004). The crystallographic studies has indicated an interconversion between different conformers of CFP at longer timescales (ms to s) compared to fluorescence (Seifert et al., 2002).

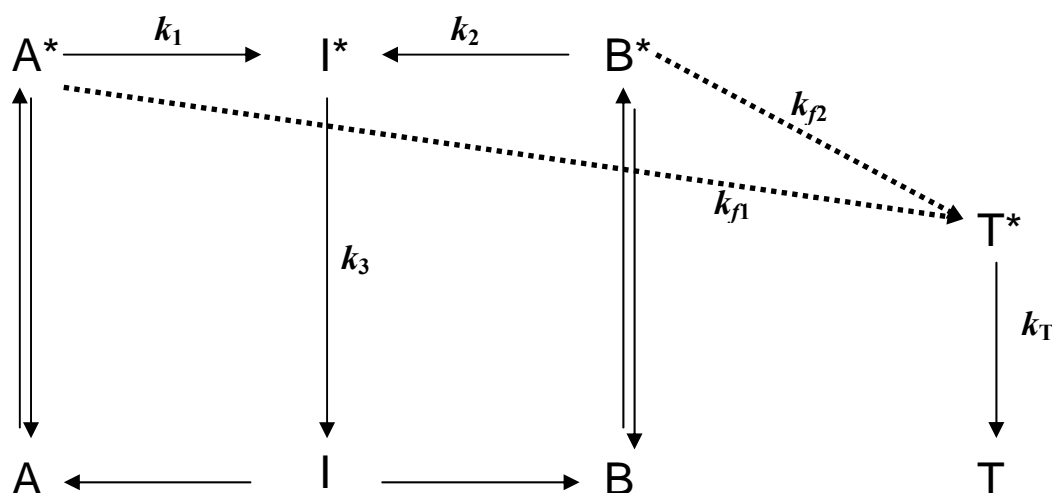


Figure 5.1) Kinetic model of CFP fluorescence and FRET occurring from CFP to Topaz. A, B, I denote ground state species; A^* , B^* , I^* , excited state species and k_i , kinetic constants. T and T^* are the ground and the excited state species of Topaz. The kinetic model elucidate that both conformations of CFP can independently be involved in FRET. The excited state interconversion between conformers of CFP has been proposed to occur at the scale of milliseconds. So the model explained here approximates these conformers to act as independent donors.

The results in section 4.1 were in agreement with the existing hypotheses and further verified the potential role of CFP conformers as individual donor molecules with distinct emission characteristics (Figure 5.1). The two excited state species of CFP namely, A^* and B^* , can independently transfer energy to the excited state species of Topaz T^* with distinct rates k_{f1} and k_{f2} . The deexcitation of Topaz would result in two different decay rates (k_{f1} and k_{f2}) for both the conformations, indicated by the negative pre-exponential factors for the two short lifetimes confirming an excited state reaction. In this model, the occurrence of other excited state reactions in the acceptor like proton transfer and ionic quenching were excluded. In the current model, the fluorescence of Topaz was assumed to be due to energy transfer from CFP, rather than direct excitation from the laser. The efficiency of energy transfer via

B*T*T was more efficient than A*T*T (indicated by increased FRET efficiency $E_{\tau_3} > E_{\tau_2}$ from Table 4.2) because of the characteristics of the excited state species of CFP. This can be attributed to differences in relative orientations of emission dipole moments of multiple conformations of CFP, where the conformation corresponding to the short lifetime can be in a favourable state resulting in a more efficient energy transfer to the acceptor chromophore. The results were corroborative with previous reports on CFP in solutions, where the second conformation giving a lifetime of approximately 1 ns was least affected by its immediate microenvironment (Borst et al., 2005). Comparison of DAS of different tandem FRET constructs demonstrated that the excited state characteristics of CFP conformers could be different. Simultaneous detection and global analysis of donor and acceptor lifetimes provided information on multiple conformations involved in FRET, resulting in a kinetic model for the CFP-YFP system (Figure 5.1).

FRET efficiencies of multiple conformations of CFP were calculated based on the kinetic model, and were found to be similar between the Clomeleon variants (Table 4.2). Since energy transfer efficiencies obtained from multiple lifetimes were very similar, the prediction of distance was not feasible. A possible explanation might be due to the relative orientation of the dipole moments of donor and acceptor fluorophores in the different Clomeleon variants. The value of the orientation factor was fixed to 2/3 (Patterson et al., 2000), assuming randomisation of relative orientation of the fluorophores. Though the variations in the spacer length between donor and acceptor were small, the different spacers might result in different orientations of dipoles for each of the constructs. Interestingly, the efficiencies calculated (Table 4.2) from mean lifetimes differed due to differences in the contributions of multiple lifetimes involved (Table 4.1), thereby clearly differentiating between the constructs. However, the calculation of absolute distances for tandem constructs was not feasible due to the lack of information about the orientation factor. Alternatively, it has already been reported that the FRET efficiencies obtained from τ_{mean} could be used to understand the distance distribution within macromolecules (dos Remedios and Moens, 1995). This approach avoids the uncertainties arising due to the random approximation of the orientation factor within macromolecules. Thus, FRET efficiencies calculated for each tandem constructs were clearly different and inversely dependent on the number of amino acids in the spacers between the tandem constructs.

5.1.2 Significance of DAS in living cells

The fluorescence characteristics of FRET are altered due to the sensitivity of donor and acceptor molecules to the microenvironment. The energy transfer efficiency in living cells

has already been observed to be highly dependent on intracellular ionic concentrations (Kuner and Augustine, 2000), the major sources of these perturbations being chloride and pH levels (Jose, 2007; Jose et al., 2007). In resting T cells, these effects were considered to be low due to low chloride and high pH levels. The intracellular chloride concentrations in these cells were less than 15 mM, as calculated from the ratio of intensity between CFP and Topaz in C24T transfected cells and comparing with recent reports (Jose et al., 2007). The biexponential decay of CFP confirmed the high pH levels in these cells. Therefore, the deviations in the fluorescence dynamics between the constructs were attributed to the differences in the donor-acceptor distances, as verified by DAS (Figure 4.5).

The simultaneous multiexponential analysis of donor and acceptor yield invaluable information about the FRET system. Elucidation of the photophysical basis of FRET occurring from CFP to Topaz can be used to interpret time domain FLIM data more effectively. This information was successfully used to model FRET as an excited state reaction and served as a basis to study conformational changes of proteins in living cells.

5.2 Activity dependent conformational changes of Lck: structure as a key to the function

Owing to its importance in the formation of immunological synapse, it was essential to comprehend the folding of Lck in resting and stimulated T-Lymphocytes. It is thought that the inhibition of the kinase activity is linked to the inhibitory structure of the protein. However, these assumptions are based on the kinase activity of the cell, rather than investigating the folding of the protein in its natural environment. Thus, evaluating the folding of Lck was crucial to understand the function of the protein in resting and stimulated cells. FRET-FLMS studies using the full-length Lck constructs allowed to verify the inhibitory structure of Lck in resting T cells. To achieve insights into the real-time conformational change of this protein in response to a stimulus, T cells expressing FRET construct of Lck were activated using soluble antibodies as well as Antigen presenting cells.

5.2.1 Conformations of Lck in unstimulated Jurkat T cells

Analysis of FRET between Lck constructs tagged with CFP and YFP (Figure 4.6) revealed the maximum efficiency (Table 4.4) with shortest values of τ_2 and τ_3 as well as mean lifetimes (Table 4.3), when CFP was located between SH3 and SH2 domains with YFP at the C-terminus (W52). Irrespective of whether CFP was positioned between the unique and SH3 domains (W51) or SH2 and kinase domains (W53) similar lifetimes, and FRET efficiencies were obtained, indicating comparable distances between the fluorophores in these constructs in their folded state (Table 4.4). DAS of W52 and W53 displayed negative pre-exponential

factors of τ_2 at the emission maximum of the acceptor, in contrast to W51. All the three FRET constructs were modelled with three exponentials, consistent with the previous kinetic model (Section 5.1.1) of CFP-YFP FRET pairs (Jose et al., 2007; Nair et al., 2006). The deviations in the mean lifetime and τ_3 of W51 indicated a large spread in the inter-chromophore distance in W51 compared to the other FRET constructs. This spread in the inter-chromophore distance in W51 implied the influence of interacting ligands on the structure of the unique domain in the final tertiary structure of Lck.

The foresaid folding pattern was in agreement with the crystal structure of Lck in its inactive form (Figure 1.3), where the SH2 domain can form an intramolecular bridge with the C-terminal tyrosine residue Y-505 (Mendieta and Gago, 2004; Sicheri and Kuriyan, 1997). In addition, the SH3 domain and the proline-rich region in the linker between the kinase and SH3 domain could also be engaged in a simultaneous intramolecular interaction. This interaction could position the kinase domain close to the SH3 domain in the final tertiary structure of the protein, as verified by the FRET-FLIM data. The structural prediction from the spectroscopic data was in agreement with the molecular modelling (Figure 5.2). These data were consistent with NMR and crystallographic observations on the structure of C-terminal part of the protein (Figure 1.3), indicating the reliability of the FRET results.

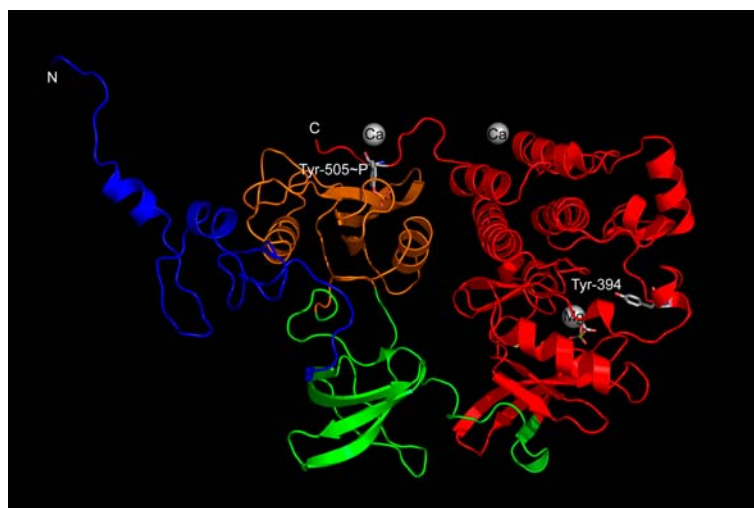


Figure 5.2) 3D model of Lck: The different domains of Lck are shown. Red, orange, and green indicate the kinase, SH2 domain and the SH3 domain, respectively. The blue colour denotes the N-terminal part of the Lck comprising of the unique region. White spheres indicate the bivalent cations binding to Lck. In this structure, the SH2 domain is in the physical proximity of C-terminal tyrosine residue, and the SH3 domain is placed close to the linker connecting SH2 and kinase domains. In the crystal structure, the proline-rich region within the linker is engaged in an intramolecular interaction with the SH3 domain (modelled by Carsten Reissner).

It has also been shown by NMR spectroscopy that unique domain has no defined structural elements in the absence of ligands and membranes (Briese and Willbold, 2003). The unique domain is highly flexible in solution, but in cells in the presence of ligands and membranes, it would be expected to have a defined tertiary structure. The large variations in the mean lifetime of W51 indicated different structures for the unique domain when engaged in interactions with different ligands. Thus the N-terminal part as previously suggested may

not be critical in the folding of the C-terminal part, but could have independent regulatory mechanisms dependent on the microenvironment of the protein. This could be interesting since the N-terminus is responsible for the interaction of the protein with the cell membrane. However, inside the cytosol, it may have a different structure which may contribute to the final folded structure of the full-length protein.

The fluorescence dynamics of different Lck constructs indicated the protein to be in an inactive conformation in unstimulated cells, where the different domains are engaged in intramolecular interactions. The fraction of molecules showing FRET (30-40%) was assumed to be in this closed passive conformation. It has been proposed that interactions of SH2 and SH3 domains of Lck with other proteins could open up the passive conformation of the protein, keeping it in a partial or fully open conformation (Xu et al., 1999). Taking intermolecular interactions of Lck into account, this would indicate at least two conformations of the protein in unstimulated T cells namely, a closed structure and a partially opened structure. Phosphate mapping experiments have shown a pool of Lck in resting T cells to be already dephosphorylated at Y505, resulting in a partially active state (Shaw et al., 1995). This pool of Lck could be involved in interactions with other proteins, which would result in prolonged open conformations of the protein. Such a fraction of Lck in an open or partially open conformation (60-70%) was also observed by FRET-FLIM studies, indicated by the fraction of ECFPs not involved in energy transfer resulting in unperturbed lifetimes similar to the control (contribution of τ_1 in Table 4.3). The presence of multiple conformations suggested equilibrium between active and passive conformations of Lck in unstimulated Jurkat T cells. This would be physiologically relevant since a partially open structure can react faster to a signal, thus contributing to the initial signalling events on T-cell stimulation.

Here, a combination of FRET and FLIM proved to be a useful technique to attain reliable information on the folding patterns of large macromolecules like Lck. The GFPs tagged to a single protein cannot be assumed to undergo free isotropic motion. It has already been suggested that changes in FRET efficiencies are more reliable than absolute FRET distances calculated (dos Remedios and Moens, 1995), dispelling the problem of unknown orientation factors for these studies. Previous sections have already shown the sensitivity of the present approach in detecting subtle changes in proteins (Section 4.1). This technique was successfully used to evaluate the conformation of Lck in unstimulated Jurkat T cells. The results were in agreement with the crystallographic and NMR studies on the structure of Lck (Sicheri and Kuriyan, 1997).

5.2.2 Conformational dynamics of Lck in stimulated Jurkat T cells

The lifetime dynamics of Lck variants in activated T cells showed an increase in the donor mean lifetime in the first few minutes, indicating a decrease in FRET efficiency. This decrease in FRET can be accounted to the opening of the conformation of Lck, bringing the ECFP and EYFP apart. Interestingly, the FRET recovered to its basal values in around 20 min, indicating the return of the protein to its original passive conformation at these later time points. These changes in protein conformation was in direct correlation with the described changes in kinase activity of Lck (Holdorf et al., 2002).

The first few minutes of the formation of an immunological synapse is followed by changes in the cytoskeleton, and an active change in the molecular ordering at the near-membrane region. These changes at the interface between T cell and antigen presenting cell is highly dynamic in spatial and temporal organisation (Cannon and Burkhardt, 2002; Kabouridis, 2006; Torres and Rosen, 2006). The SH3 domain of Lck is known to be associated with N-WASP molecule, which is a main mediator for actin polymerisation (Torres and Rosen, 2006). The open conformation of Lck could thus contribute to a rapid change in the cytoskeleton via its association with N-WASP, while the SH2 and kinase domains could be involved in the phosphorylation of near-membrane scaffolding proteins resulting in a wider distribution of signals in the active molecular region.

The active form of Lck (resulting from autophosphorylation of Y-394 between Kinase lobes) has been reported to be localised to the distal edges of the mature immunological synapse (Holdorf et al., 2002). The localisation of the open conformation of Lck to the periphery of the synapse, indicated by increase in donor mean lifetimes from the FLIM studies, was in agreement with this (Figure 4.11). At the early stages of synapse formation, Lck could be involved in the formation of a temporary rigid molecular framework by opening its conformation. It could possibly associate with other scaffolding proteins and with the same family of proteins by forming dimers or oligomers using its regulatory domains. This may stabilise the initial horizontal scaffolds of the immunological synapse, which would hinder the free movements of receptors, lipid rafts, and transmembrane molecules forcing them to stay at the active area of the synapse.

Investigation of the spatial and temporal conformations of Lck was done using real-time FLIM in living cells. The studies on Lck in unstimulated cells (Section 5.2.1) indicated equilibrium between the open and closed conformations of the protein. The partially or fully

open conformations may contribute to the initial signalling events in the immunological synapse. Upon contact with Antigen presenting cells, a spatial and temporal segregation of conformations for Lck was observed, where the protein was translocated to the T cell-APC contact (Figure 4.11). The temporal conformational changes of Lck during the synapse formation implied the restricted nature of the binding of the protein via its protein-protein interaction domains, highlighting a specific dynamic mechanism of signal divergence and cell polarisation at the immunological synapse.

5.3 Calcium-dependent conformational changes of MAGUKs: modular scaffolds and near-membrane complexes

The structural regulation of the C-terminal part of the MAGUKs is very important, considering the role of these proteins in multiple signalling pathways. The regulation of the restrained structure is mediated by changes in intracellular calcium levels, which indirectly affects the structure of the protein. MAGUKs are very important proteins in various cell-adhesion interfaces, and recruit several molecules to stabilise them. It was thus essential to understand the regulation of SH3-HOOK-GUK unit and comprehend how it could participate in multiple scaffolding mechanisms.

5.3.1 Regulatory structure of Dlg family proteins and comparison with Src kinases

FLIM studies on CFP-SH3-HOOK-GUK-YFP revealed the donor mean lifetimes of the MAGUK FRET constructs in resting cells to be significantly lower compared to the FRET control (Table 4.5). This confirmed an intramolecular interaction between SH3 and GUK domains of MAGUKs in resting cells, as predicted by biochemical methods and consistent with X-ray crystallographic structures (McGee et al., 2001; Wu et al., 2000). The X-ray crystallographic studies of SH3-HOOK-GUK region of SAP90/PSD95 has characterised the intramolecular interaction of SH3 and GUK domains (McGee et al., 2001; Wu et al., 2000). Intramolecular interactions of SH3 domains are well established in the Src family of non-receptor tyrosine kinases (Sicheri and Kuriyan, 1997). These interactions are vital in keeping the kinase in a catalytically inactive state. SH3 domains of these PTKs play an important role in defining conformation or activity of the kinase. The SH3 domain of Src interacts with type II poly-proline segment in the linker between SH2 and kinase domains. In addition, it contacts the kinase domain through parts of the SH3 domain distinct from the core-ligand binding surfaces (Roskoski, 2004; Sicheri and Kuriyan, 1997). The regulatory intramolecular interaction between SH3 and GUK domains of MAGUKs may resemble that in Src kinases. Interestingly, the SH3 domains of both these proteins are positioned to bring them N-terminal to the tyrosine and guanylate kinase domains of Src kinase and MAGUKs, respectively.

These interactions define restrained structures for the proteins, hindering intermolecular association using these domains. This study is focussed on activity-dependent conformational changes and folding patterns of the SH3-HOOK-GUK unit of MAGUKS in living cells.

5.3.2 Calcium-dependent conformational changes of Dlg family of proteins

Upon elevation of intracellular calcium, calcium-binding proteins like calmodulin may bind to the HOOK region of MAGUKs (Masuko et al., 1999; Paarmann et al., 2002). This interaction is thought to open up the conformation, destabilising the interaction between SH3 and GUK domains or alternatively stabilising the open conformation by binding to the HOOK region (McGee et al., 2001; Tavares et al., 2001). In both cases, MAGUKs are believed to respond by a conformational change bringing SH3 and GUK domains apart. Interestingly, FLIM-FLMS measurements on CFP-SH3-HOOK-GOOK-YFP units of SAP90/PSD95 and SAP97/hDlg indicated an increase in FRET efficiency in response to elevation of intracellular calcium. This was in contrast to the expected decrease in intramolecular FRET as a result of opening of the conformation, bringing the flanking CFP and YFP fluorophores further apart (Table 4.6).

On elevating the intracellular calcium levels in cells expressing the FRET constructs, the ratio of YFP to CFP intensities increased, and the percentage of this increase was consistent with the increase in FRET efficiency (Table 4.6). This increase cannot be attributed to the intramolecular FRET since at high calcium levels calcium-binding proteins like calmodulin can access the HOOK region separating the two interacting domains, thus keeping the SH3 and GUK domain further apart. There are biochemical evidences indicating a possible interaction within the SH3 domain and GUK regions of different MAGUKs. At high levels of calcium and in the presence of calmodulin SAP102/NE-Dlg has been shown to be associated with PSD95, highlighting a probability of clustering of MAGUK family members via the SH3 and GUK domains (Masuko et al., 1999; Nix et al., 2000; Shin et al., 2000; Wu et al., 2000). This clustering could explain an increase in FRET efficiency due to the formation of parallel or anti-parallel dimers (Figure 5.3), which could serve as a rigid molecular backbone in response to an increase in the near-membrane calcium levels. Since the MAGUKs have similar SH3 and GUK domains, the dimer formation could be between the same or different proteins of the family.

Of the different calcium-binding proteins, only calmodulin has been shown to be associated with the HOOK regions of SAP97/hDlg and SAP102/NE-Dlg (Masuko et al., 1999; Paarmann et al., 2002). The disruption of association of MAGUKS with calmodulin abolished the increase in FRET on increasing the intracellular calcium (Figure 4.14). The

calcium-binding activity of calmodulin was inhibited by inhibitor^{W7} in living cells, which produced comparable effects on SAP97 and PSD95 (Table 4.6). To date, a direct association of PSD95 with calmodulin has not been shown, though biochemical studies indicate an association of SAP90/PSD95 with other MAGUKs in presence of calcium and calmodulin (Masuko et al., 1999). Interestingly, FRET-FLMS measurements indicated similar response for the protein as observed for SAP97/hDlg on increasing the calcium levels or on inhibiting calmodulin activity, pointing towards similar calcium-dependent changes at the molecular level in this family of proteins. However, the possibility for the presence of calcium-binding proteins similar to calmodulin, which may associate with PSD95 in a calcium-dependent manner, cannot be ruled out. Thus, FRET studies indicated a novel mechanism of formation of molecular frameworks of scaffolding proteins in response to an extracellular signal.

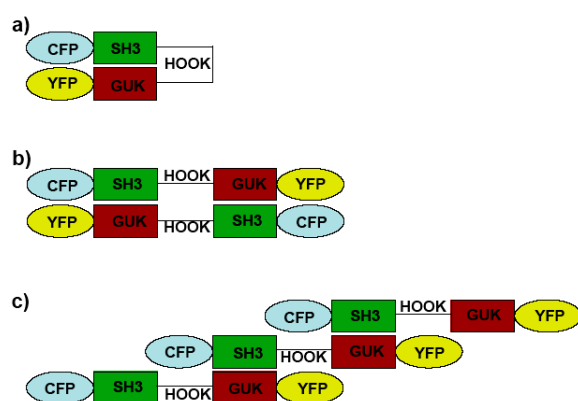


Figure 5.3) Possible conformations of MAGUKs deciding the different states of signalling in the molecule. a) The closed conformation of MAGUKs: the SH3 and the GUK domain is engaged in an intramolecular interaction. b) Possible anti-parallel dimers of MAGUKs upon elevation of intracellular calcium c) Possible parallel arrangement of MAGUKs upon stimulation. These parallel and antiparallel dimers can be formed between the same or different molecules within the MAGUK family.

5.3.3 Role of MAGUKs in near-membrane scaffolds

Physiologically, the conformational changes of MAGUKS in response to a signal could spontaneously rearrange cellular cytoskeleton and scaffolding molecules associated with cell-adhesion, receptors, and cell signalling. The HOOK region is a flexible linker, which can provide the key activation required for the conformational change by placing calcium-binding proteins between these domains, thus sterically disturbing the physical proximity of intramolecular interaction of SH3 and GUK domains. However, the elevation of calcium in response to an extracellular signal is a key process in all cell types, especially when forming and maintaining stable contacts with identical cells. This can turn out to be a crucial mechanism for the molecular rearrangement at these cell-cell interfaces resulting in a dynamic molecular polarisation and gradient, which may decide the morphology and signalling state of the cell.

Calcium-dependent conformational changes of Dlg family of MAGUKs were addressed by FRET and FLIM. The changes in FRET were ascribed to the formation of parallel or anti-parallel dimers, creating a rigid molecular framework of cytoplasmic

scaffolds. The FRET data indicated the potential role of intra- and intermolecular interactions of MAGUKs to mediate near-membrane molecular polarisation. This rigid framework can be involved in positioning the cell-adhesion molecules, receptors, and channels at their respective signalling zones within a synapse or cell-cell interface. On the other hand, the open conformation of MAGUKS could interact with the cytoskeleton and other signalling molecules, resulting in a spontaneous reorganisation of the membrane cytoskeleton in response to the signals. It would be interesting to know how the dissociation of this complex is regulated, since the calcium levels decrease with time after an activity-dependent elevation. Thus, the calcium-dependent conformational changes of these proteins could be a basic mechanism that decides not only the resulting molecular architecture, but also the morphology and signalling state of the cell.

5.4 Lck as a regulatory protein affecting localisation SAP97/hDlg to synapses

Src kinases and MAGUKs are implicated in the formation, stabilisation, and maintenance of a variety of cell-adhesion mechanisms. The molecules in the Src kinase family have been shown to interact with different members of the MAGUK family. The activity of these molecules is regulated by their conformational changes, allowing them to interact with nearby molecules. To date, Lck is the only Src family protein known to associate with SAP97/hDlg. Since Lck is known to redistribute itself upon the formation of an immunological synapse, it was vital to understand the redistribution of its binding partner namely, SAP97/hDlg in T-lymphocytes. Investigation of a proline-rich alternative splicing at the N-terminus of SAP97/hDlg, which is thought to potentially mediate its binding to Lck, revealed this splicing to be critical in its subcellular localisation as well as for its functional association with Lck.

5.4.1 Relevance of I1 splicing on the recruitment of SAP97/hDlg to the immunological synapse

Though the I1 splicing has been reported to be important in the membrane localisation of SAP97/hDlg, to date, no clear investigation on the possible effects of this splicing regarding the recruitment of the protein to the immunological synapse has been undertaken (McLaughlin et al., 2002). SAP97/hDlg belongs to a set of molecules which are regulated by the variation in intracellular calcium, as discussed in Section 5.3. Previous works have shown the recruitment of this protein to the T cell-APC interface (Xavier et al., 2004). Similar studies with T cells presented with antigen coated beads, which have been shown to be reliable model systems for generating surrogate or mock immunological synapses, have also displayed the recruitment of the protein to the cell-bead interface (Ludford-Menting et al.,

2002; Xavier et al., 2004). Therefore, to study the role of the N-terminal splicing of SAP97/hDlg on the recruitment of the protein during the formation of an immunological synapse, a similar model system was used.

Comparison of the distribution of endogenous SAP97/hDlg in unstimulated and stimulated Jurkat T cells indicated an activity-dependent localisation of SAP97/hDlg in different subcellular compartments. The endogenous SAP97/hDlg was translocated to the cell-bead interface in 5 min, consistent with the previous reports (Xavier et al., 2004). Interestingly, the distribution of spliced isoforms of this protein differed with respect to the presence or absence of its proline-rich I1 splice domain. I1 splicing was investigated in combination with either of the two splicing between the HOOK region, namely I2 or I3. A cytosolic pool of SAP97/hDlg was observed, in addition to its membrane localisation. In stimulated Jurkat T cells, SAP97/hDlg containing I1 translocated to the cell-bead contact similar to the distribution of the endogenous protein upon stimulation.

Interestingly, on expressing SAP97/hDlg lacking the I1 splicing, the protein did not show a translocation to the cell-bead contact. This indicated the relevance of this splicing in the recruitment of SAP97/hDlg in Jurkat T cells, which could play a critical role in its localisation to the immunological synapse. This could be important considering the significance of the transsynaptic signalling through SAP97/hDlg in the stabilisation of synapses in neurons and epithelial cells (Funke et al., 2005; Regalado et al., 2006). Therefore, it was crucial to extend the studies to natural systems involving the stimulation of T cells with Antigen presenting cells, which form an immunological synapse at their contact sites, to appreciate the physiological relevance. The subcellular distribution of I1 containing SAP97/hDlg in resting and stimulated T cells was similar to the reports on the distribution pattern of Lck (Ehrlich et al., 2002; Holdorf et al., 2002). The loss of recruitment of SAP97/hDlg including I1 to the cell-bead contacts in Lck deficient T cell lines amplified its relevance. Therefore, the association of SAP97/hDlg with Lck seemed to be crucial, deciding its translocation to the immunological synapse. This affirmed the possibility for the intermolecular interactions between these proteins to be critical in the signal stabilisation of immunological synapses, considering the potential for both proteins to organise multiprotein scaffolds and affect the cell morphology (Round et al., 2005).

5.4.2 Role of SAP97/hDlg-Lck interaction in the immunological synapse

It has been observed that an initial period of approach of the T cell and APC with a homogeneous distribution of TCR and peptide-MHC ligand is followed within seconds of

contact by a step of TCR triggering resulting in an initiation of T-cell intracellular signalling. After few minutes, receptor clustering and surface molecule redistribution is induced by the early and robust signalling events resulting from this early TCR–ligand contact (Huppa and Davis, 2003). This early stage is marked by high tyrosine phosphorylation and calcium levels, resulting in a change in the cellular microenvironment (Delon and Germain, 2000). The current study indicates the potential role of Lck and SAP97 to be key molecules involved in a multiprotein complex which regulates the resulting molecular architecture of the immunological synapse by changes in their localisation and conformation.

The C-terminal part of MAGUKs has been implicated in the formation of multimeric complexes with other members in the same protein family, as discussed in Section 5.3. It is not clear how these interlocked complexes are distributed within the signalling zones of the immunological synapse. The interaction with Lck could be critical in the localisation of these interlocked scaffolds to respective signalling zones. This hypothesis gets along with the current ideas about MAGUK mediated complexes (McGee et al., 2001; Montgomery et al., 2004), since the proline-rich I1 splicing could be involved in deciding the localisation of the protein independent of its C-terminal unit, which is calcium-regulated. This was consistent with the recent notion, that a network of PDZ domain containing proteins may be critical in deciding the polarity of the immunological synapse (Ludford-Menting et al., 2005).

The activity-dependent localisation of SAP97/hDlg isoforms indicated their possible recruitment of different pools of proteins to synapses. This in turn implied that combinations of different splicings may be involved in recruiting multiple signalling complexes, serving the function of different proteins controlling the formation and maintenance of the synapse. It is thought that the localisation and structural regulation of proteins are critical factors affecting the stability and maintenance of a stable cell-cell contact. Here, with the help of advanced microscopy data, it is shown that the multidomain proteins Lck and SAP97/hDlg is not only translocated to the immunological synapse, but could be involved in activity-dependent structural regulation which may be critical in deciding the organisation of the immunological synapse.

Multidomain proteins like Src kinases and MAGUKs might be critical in the differentiation and spatial regulation of signalling zones by regulating the changes at the molecular and submolecular level. These changes occurring in dimensions of few nanometers may be relevant to the momentary regulation of scaffolds leading to the dynamic changes in the molecular organisation, resulting in the functioning of a mature immunological synapse.

6 CONCLUSIONS

Activity-dependent redistribution of proteins is fundamental in the self-organisation of a system for biological functions. This organisation happens at the molecular or submolecular level below the limit of conventional optical microscopy (few 100 nm). Thus, it was technologically challenging to probe these molecular processes (1-10 nm) without disturbing the living state of the cell. Here, a multiwavelength FRET-FLIM system with simultaneous donor-acceptor detection and analysis was adopted to study these changes from living cells. Decay Associated Spectrum enabled to distinguish subtle changes in the distance distribution within a macromolecule. Constructs that differed in few amino acids showed profound differences in their FRET efficiencies. Thus, the FRET efficiency was taken as a direct measure for understanding distance distributions, rather than calculating absolute distances prone to errors in estimating the value of orientation factor. However, the current detection and analysis protocol could not be used for detecting changes in intensity decays at very short time scales (ms to seconds) to study faster processes, frequently observed in biological samples.

The changes in FRET efficiencies were effectively used to understand the structure of full-length Lck in unstimulated lymphocytes. The FRET efficiencies between different constructs of Lck indicated a folding pattern of the protein in agreement with the existing hypothesis. However, the studies revealed equilibrium between different Lck conformations in unstimulated cells. This would be crucial when the cell initiates response to a stimulus by recruiting the protein to respective signalling zones, followed by transient conformational changes. The conformational distribution profiles of Lck were in accordance with the existing knowledge on kinase activity (Holdorf et al., 2002). It remains to be confirmed if Lck could form oligomers with other members in the Src family kinases in its open conformation. This would provide a short-lived but stable mechanism responsible for clustering and differentiation of the different macromolecules into various signalling zones during the initial moments of cell-cell contact.

Similar to the activity-dependent changes in the conformation of Lck; MAGUKs showed ligand-dependent conformational changes. These responses to the changes in intracellular calcium levels were restricted by disturbing the activity of calcium-binding protein calmodulin. Interestingly in SAP90/PSD95, similar to SAP97/hDlg, the changes were abolished suggesting either a calmodulin-dependent mechanism or the activity of a possible calcium-binding protein similar to calmodulin. However, the results were conclusive in

showing that the changes observed were directly in correlation with the changes in intracellular calcium. The insights into conformational changes of SAP97/hDlg illustrated that the balance between its restrained structure and the ligand-modulated structure may be principal in deciding the scaffolding state of the molecule. Thus, it would be equally important to investigate how these complexes are disassembled or regulated for longer duration. More studies would be required to answer these questions, since MAGUKs are central components involved in the organisation of synapses and other cell-adhesion interfaces.

The results indicated the potential role of the C-terminus of SAP97/hDlg in the molecular organisation of scaffolds. Alternatively, the presence of the N-terminal splicing was observed to be relevant to the localisation of the protein in an active cell. Since, this is the only splicing known outside the conserved C-terminus, it could be a fundamental mechanism involved in the corecruitment of multidomain proteins to the newly formed cell-cell interface. The absence of N-terminal proline-rich region as well as the deficiency of Lck in cells affected the final localisation of SAP97/hDlg. The structural regulation and distribution profiles of SAP97/hDlg supported the current hypothesis for the scaffolding mechanism of MAGUKs. Therefore, it would be interesting to see whether such effects would also be observed in neurons and other cell-adhesion interfaces, since there is no information so far concerning the localisation of these isoforms (except I3) during different stages of neuronal maturation or synaptogenesis.

Multidomain proteins are imperative in the organisation of scaffolding molecules in various signalling zones, elevating the importance of understanding not only their subcellular distribution but also their molecular behaviour in the respective compartments. Here, a combination of multidisciplinary approaches has provided insights into the transient conformational changes of these proteins in relation to their spatial distribution patterns. It was possible to evaluate the structure and localisation of these molecules in correlation to their activity and function, considering the complex spectroscopic characteristics of the fluorophores involved. Currently these observations are made on an ensemble of proteins, and the resulting observations are statistical in nature. In future, these studies could be extended to the regime of single fluorescent molecules and diffusion related processes to isolate characterise and control macromolecular behaviour in their natural environment.

REFERENCES

- Abbas, A. K., and Lichtman, A. H. (2003). Cellular and Molecular Immunology, 5 edn (Philadelphia, Saunders).
- Beechem, J. M. (1992). Global analysis of biochemical and biophysical data. *Methods Enzymol* 210, 37-54.
- Beechem, J. M., and Brand, L. (1986). Global analysis of fluorescence decay: applications to some unusual experimental and theoretical studies. *Photochem Photobiol* 44, 323-329.
- Borst, J. W., Hink, M. A., Hoek, A. V., and Visser, A. J. W. G. (2005). Effects of Refractive index and viscosity on Fluorescence and Anisotropy Decays of Enhanced Cyan and Yellow Fluorescent Proteins. *J Fluoresc* 15, 153-160.
- Briese, L., and Willbold, D. (2003). Structure determination of human Lck unique and SH3 domains by nuclear magnetic resonance spectroscopy. *BMC Struct Biol* 3, 3.
- Bromley, S. K., Burack, W. R., Johnson, K. G., Somersalo, K., Sims, T. N., Sumen, C., Davis, M. M., Shaw, A. S., Allen, P. M., and Dustin, M. L. (2001). The immunological synapse. *Annu Rev Immunol* 19, 375-396.
- Brunger, A. T. (1988). X-PLOR, HHMI, DMBB. Yale University, New Haven, CT.
- Bystroff, C., Thorsson, V., and Baker, D. (2000). HMMSTR: a hidden Markov model for local sequence-structure correlations in proteins. *J Mol Biol* 301, 173-190.
- Cannon, J. L., and Burkhardt, J. K. (2002). The regulation of actin remodeling during T-cell-APC conjugate formation. *Immunol Rev* 186, 90-99.
- Chan, F. K., Siegel, R. M., Zacharias, D., Swofford, R., Holmes, K. L., Tsien, R. Y., and Lenardo, M. J. (2001). Fluorescence resonance energy transfer analysis of cell surface receptor interactions and signaling using spectral variants of the green fluorescent protein. *Cytometry* 44, 361-368.
- Chattoraj, M., King, B. A., Bublitz, G. U., and Boxer, S. G. (1996). Ultra-fast excited state dynamics in green fluorescent protein: multiple states and proton transfer. *Proc Natl Acad Sci U S A* 93, 8362-8367.
- Clegg, R. M. (1996). Fluorescence resonance energy transfer. In *Fluorescence Imaging Spectroscopy and Microscopy*, X. F. Wang, and B. Herman, eds. (New York, John Wiley & Sons Inc.), pp. 179-251.
- Davenport, L., Knutson, J. R., and Brand, L. (1986). Excited-state proton transfer of equilenin and dihydroequilenin: interaction with bilayer vesicles. *Biochemistry* 25, 1186-1195.
- Day, R. N., Periasamy, A., and Schaufele, F. (2001). Fluorescence resonance energy transfer microscopy of localized protein interactions in the living cell nucleus. *Methods* 25, 4-18.
- Deisseroth, K., Heist, E. K., and Tsien, R. W. (1998). Translocation of calmodulin to the nucleus supports CREB phosphorylation in hippocampal neurons. *Nature* 392, 198-202.
- DeLano, W. L. (2002). The PyMOL Molecular Graphics System. Delano Scientific, San Carlos, CA, USA.

- Delon, J., and Germain, R. N. (2000). Information transfer at the immunological synapse. *Curr Biol* 10, R923-933.
- Delon, J., Stoll, S., and Germain, R. N. (2002). Imaging of T-cell interactions with antigen presenting cells in culture and in intact lymphoid tissue. *Immunol Rev* 189, 51-63.
- Donnadieu, E., Bismuth, G., and Trautmann, A. (1994). Antigen recognition by helper T cells elicits a sequence of distinct changes of their shape and intracellular calcium. *Curr Biol* 4, 584-595.
- dos Remedios, C. G., and Moens, P. D. (1995). Fluorescence resonance energy transfer spectroscopy is a reliable "ruler" for measuring structural changes in proteins. Dispelling the problem of the unknown orientation factor. *J Struct Biol* 115, 175-185.
- Duncan, R. R., Bergmann, A., Cousin, M. A., Apps, D. K., and Shipston, M. J. (2004). Multi-dimensional time-correlated single photon counting (TCSPC) fluorescence lifetime imaging microscopy (FLIM) to detect FRET in cells. *J Microsc* 215, 1-12.
- Dustin, M. L. (2003). Coordination of T cell activation and migration through formation of the immunological synapse. *Ann N Y Acad Sci* 987, 51-59.
- Dustin, M. L. (2005). A dynamic view of the immunological synapse. *Semin Immunol* 17, 400-410.
- Dustin, M. L. (2006). Impact of the immunological synapse on T cell signaling. *Results Probl Cell Differ* 43, 175-198.
- Dustin, M. L., and Colman, D. R. (2002). Neural and immunological synaptic relations. *Science* 298, 785-789.
- Dye, B. T., Schell, K., Miller, D. J., and Ahlquist, P. (2005). Detecting protein-protein interaction in live yeast by flow cytometry. *Cytometry A* 63, 77-86.
- Eck, M. J., Atwell, S. K., Shoelson, S. E., and Harrison, S. C. (1994). Structure of the regulatory domains of the Src-family tyrosine kinase Lck. *Nature* 368, 764-769.
- Eck, M. J., Shoelson, S. E., and Harrison, S. C. (1993). Recognition of a high-affinity phosphotyrosyl peptide by the Src homology-2 domain of p56lck. *Nature* 362, 87-91.
- Ehrlich, L. I., Ebert, P. J., Krummel, M. F., Weiss, A., and Davis, M. M. (2002). Dynamics of p56lck translocation to the T cell immunological synapse following agonist and antagonist stimulation. *Immunity* 17, 809-822.
- El-Husseini, A. E., Topinka, J. R., Lehrer-Graiwer, J. E., Firestein, B. L., Craven, S. E., Aoki, C., and Bredt, D. S. (2000). Ion channel clustering by membrane-associated guanylate kinases. Differential regulation by N-terminal lipid and metal binding motifs. *J Biol Chem* 275, 23904-23910.
- Ellenberg, J., Lippincott-Schwartz, J., and Presley, J. F. (1999). Dual-colour imaging with GFP variants. *Trends Cell Biol* 9, 52-56.
- Emptage, N. J. (2001). Fluorescent imaging in living systems. *Curr Opin Pharmacol* 1, 521-525.
- Evans, J., and Yue, D. T. (2003). New turf for CFP/YFP FRET imaging of membrane signaling molecules. *Neuron* 38, 145-147.

- Fujita, A., and Kurachi, Y. (2000). SAP family proteins. *Biochem Biophys Res Commun* 269, 1-6.
- Funke, L., Dakoji, S., and Brecht, D. S. (2005). Membrane-associated guanylate kinases regulate adhesion and plasticity at cell junctions. *Annu Rev Biochem* 74, 219-245.
- Gadella, T. W. J., Jr., G. N. M. van der Krogt, and T. Bisseling (1999). GFP-based FRET microscopy in living plant cells. *Trends Plant Sci* 4, 287-291.
- Garner, C. C., Nash, J., and Huganir, R. L. (2000). PDZ domains in synapse assembly and signalling. *Trends Cell Biol* 10, 274-280.
- Germain, R. N., and Jenkins, M. K. (2004). In vivo antigen presentation. *Curr Opin Immunol* 16, 120-125.
- Germain, R. N., Miller, M. J., Dustin, M. L., and Nussenzweig, M. C. (2006). Dynamic imaging of the immune system: progress, pitfalls and promise. *Nat Rev Immunol* 6, 497-507.
- Godreau, D., Neyroud, N., Vranckx, R., and Hatem, S. (2004). MAGUKs: beyond ionic channel anchoring. *Med Sci (Paris)* 20, 84-88.
- Gonfloni, S., Williams, J. C., Hattula, K., Weijland, A., Wierenga, R. K., and Superti-Furga, G. (1997). The role of the linker between the SH2 domain and catalytic domain in the regulation and function of Src. *Embo J* 16, 7261-7271.
- Grimbacher, B., Warnatz, K., and Peter, H. H. (2003). The immunological synapse for B-cell memory: the role of the ICOS and its ligand for the longevity of humoral immunity. *Curr Opin Allergy Clin Immunol* 3, 409-419.
- Guex, N., and Peitsch, M. C. (1997). SWISS-MODEL and the Swiss-PdbViewer: an environment for comparative protein modeling. *Electrophoresis* 18, 2714-2723.
- Habuchi, S., Cotlet, M., Hofkens, J., Dirix, G., Michiels, J., Vanderleyden, J., Subramaniam, V., and Schryver, F. C. D. (2002). Resonance Energy Transfer in a Calcium Concentration-Dependent Cameleon Protein. *Biophys J* 83, 3499-3506.
- Hanada, N., Makino, K., Koga, H., Morisaki, T., Kuwahara, H., Masuko, N., Tabira, Y., Hiraoka, T., Kitamura, N., Kikuchi, A., and Saya, H. (2000). NE-dlg, a mammalian homolog of *Drosophila* dlg tumor suppressor, induces growth suppression and impairment of cell adhesion: possible involvement of down-regulation of beta-catenin by NE-dlg expression. *Int J Cancer* 86, 480-488.
- Hanada, T., Lin, L., Chandy, K. G., Oh, S. S., and Chishti, A. H. (1997). Human homologue of the *Drosophila* discs large tumor suppressor binds to p56lck tyrosine kinase and Shaker type Kv1.3 potassium channel in T lymphocytes. *J Biol Chem* 272, 26899-26904.
- Hanada, T., Takeuchi, A., Sondarva, G., and Chishti, A. H. (2003). Protein 4.1-mediated membrane targeting of human discs large in epithelial cells. *J Biol Chem* 278, 34445-34450.
- Hanahan, D. (1983). Studies on transformation of *Escherichia coli* with plasmids. *J Mol Biol* 166, 557-580.
- Harpur, A. G., Wouters, F. S., and Bastiaens, P. I. (2001). Imaging FRET between spectrally similar GFP molecules in single cells. *Nat Biotechnol* 19, 167-169.

- Hofmann, G., Schweimer, K., Kiessling, A., Hofinger, E., Bauer, F., Hoffmann, S., Rosch, P., Campbell, I. D., Werner, J. M., and Sticht, H. (2005). Binding, domain orientation, and dynamics of the Lck SH3-SH2 domain pair and comparison with other Src-family kinases. *Biochemistry* 44, 13043-13050.
- Holdorf, A. D., Lee, K. H., Burack, W. R., Allen, P. M., and Shaw, A. S. (2002). Regulation of Lck activity by CD4 and CD28 in the immunological synapse. *Nat Immunol* 3, 259-264.
- Holzer, W., Penzkofer, A., Fuhrmann, M., and Hegemann, P. (2002). Spectroscopic characterization of flavin mononucleotide bound to the LOV1 domain of Phot1 from *Chlamydomonas reinhardtii*. *Photochem Photobiol* 75, 479-487.
- Horejsi, V., Zhang, W., and Schraven, B. (2004). Transmembrane adaptor proteins: organizers of immunoreceptor signalling. *Nat Rev Immunol* 4, 603-616.
- Huppa, J. B., and Davis, M. M. (2003). T-cell-antigen recognition and the immunological synapse. *Nat Rev Immunol* 3, 973-983.
- Inaba, K., and Inaba, M. (2005). Antigen recognition and presentation by dendritic cells. *Int J Hematol* 81, 181-187.
- Janeway, C., Travers, P., Walport, M., and Shlomchik, a. M. (2001). *immunobiology*, 5 edn (Newyork and London, Garland Science).
- Jares-Erijman, E. A., and Jovin, T. M. (2003). FRET imaging. *Nat Biotechnol* 21, 1387-1395.
- Jones, D. T., Taylor, W. R., and Thornton, J. M. (1992). A new approach to protein fold recognition. *Nature* 358, 86-89.
- Jose, M. (2007) Investigating protein-protein interactions by FRET-FLIM in living cells: insights into interactions mediated by the presynaptic protein Bassoon, PhD thesis submitted to Otto-von-Guericke University, Magdeburg.
- Jose, M., Nair, D. K., Reissner, C., Hartig, R., and Zuschratter, W. (2007). Photophysics of Clomeleon by FLIM: discriminating excited state reactions along neuronal development. *Biophys J* 92, 2237-2254.
- Kabouridis, P. S. (2006). Lipid rafts in T cell receptor signalling. *Mol Membr Biol* 23, 49-57.
- Kalia, L. V., and Salter, M. W. (2003). Interactions between Src family protein tyrosine kinases and PSD-95. *Neuropharmacology* 45, 720-728.
- Kapusta, P., Erdmann, R., Ortmann, U., and Wahl, M. (2003). Time-resolved fluorescence anisotropy measurements made simple. *J Fluoresc* 13, 179-183.
- Karpova, T. S., Baumann, C. T., He, L., Wu, X., Grammer, A., Lipsky, P., Hager, G. L., and McNally, J. G. (2003). Fluorescence resonance energy transfer from cyan to yellow fluorescent protein detected by acceptor photobleaching using confocal microscopy and a single laser. *J Microsc* 209, 56-70.
- Kelley, L., Bennett-Lovsey, R., Herbert, A., and Fleming, K. (2006). Phyre - Protein Homology/analogy Recognition Engine. ,Imperial College, London.
- Kemnitz, K., Pfeifer, L., Paul, R., and Coppey-Moisán, M. (1997). Novel detectors for fluorescence lifetime imaging on the picosecond time scale. *J Fluoresc* 7, 93-98.

- Kemnitz, K., Pfeifer, L., Paul, R., Fink, A., and Bergmann, A. (1995). Time- and Space correlated Single Photon Counting Spectroscopy. *SPIE Proc* 2628, 2-11.
- Kim, E., and Sheng, M. (2004). PDZ domain proteins of synapses. *Nat Rev Neurosci* 5, 771-781.
- Knutson, J. R., Walbridge, D. G., and Brand, L. (1982). Decay-associated fluorescence spectra and the heterogeneous emission of alcohol dehydrogenase. *Biochemistry* 21, 4671-4679.
- Kuner, T., and Augustine, G. J. (2000). A genetically encoded ratiometric indicator for chloride: capturing chloride transients in cultured hippocampal neurons. *Neuron* 27, 447-459.
- Kupfer, A., and Dennert, G. (1984). Reorientation of the microtubule-organizing center and the Golgi apparatus in cloned cytotoxic lymphocytes triggered by binding to lysable target cells. *J Immunol* 133, 2762-2766.
- Kupfer, A., and Singer, S. J. (1989a). Cell biology of cytotoxic and helper T cell functions: immunofluorescence microscopic studies of single cells and cell couples. *Annu Rev Immunol* 7, 309-337.
- Kupfer, A., and Singer, S. J. (1989b). The specific interaction of helper T cells and antigen-presenting B cells. IV. Membrane and cytoskeletal reorganizations in the bound T cell as a function of antigen dose. *J Exp Med* 170, 1697-1713.
- Kupfer, A., Singer, S. J., Janeway, C. A., Jr., and Swain, S. L. (1987). Coclustering of CD4 (L3T4) molecule with the T-cell receptor is induced by specific direct interaction of helper T cells and antigen-presenting cells. *Proc Natl Acad Sci U S A* 84, 5888-5892.
- Kupfer, A., Swain, S. L., Janeway, C. A., Jr., and Singer, S. J. (1986). The specific direct interaction of helper T cells and antigen-presenting B cells. *Proc Natl Acad Sci U S A* 83, 6080-6083.
- Lakowicz, J. R. (1999). *Principles of Fluorescence Spectroscopy*, Second edn, Kluwer Academic/Plenum Publishers).
- Lakowicz, J. R., Szmacinski, H., Nowaczyk, K., Berndt, K. W., and Johnson, M. (1992a). Fluorescence lifetime imaging. *Anal Biochem* 202, 316-330.
- Lakowicz, J. R., Szmacinski, H., Nowaczyk, K., and Johnson, M. L. (1992b). Fluorescence lifetime imaging of calcium using Quin-2. *Cell Calcium* 13, 131-147.
- Lakowicz, J. R., Szmacinski, H., Nowaczyk, K., and Johnson, M. L. (1992c). Fluorescence lifetime imaging of free and protein-bound NADH. *Proc Natl Acad Sci U S A* 89, 1271-1275.
- Lanzavecchia, A., and Sallusto, F. (2000). From synapses to immunological memory: the role of sustained T cell stimulation. *Curr Opin Immunol* 12, 92-98.
- Laskowski, R. A., Rullmannn, J. A., MacArthur, M. W., Kaptein, R., and Thornton, J. M. (1996). AQUA and PROCHECK-NMR: programs for checking the quality of protein structures solved by NMR. *J Biomol NMR* 8, 477-486.
- Lippincott-Schwartz, J., and Patterson, G. H. (2003). Development and use of fluorescent protein markers in living cells. *Science* 300, 87-91.

- Ludford-Menting, M. J., Oliaro, J., Sacirbegovic, F., Cheah, E. T., Pedersen, N., Thomas, S. J., Pasam, A., Iazzolino, R., Dow, L. E., Waterhouse, N. J., *et al.* (2005). A network of PDZ-containing proteins regulates T cell polarity and morphology during migration and immunological synapse formation. *Immunity* 22, 737-748.
- Ludford-Menting, M. J., Thomas, S. J., Crimeen, B., Harris, L. J., Loveland, B. E., Bills, M., Ellis, S., and Russell, S. M. (2002). A functional interaction between CD46 and DLG4: a role for DLG4 in epithelial polarization. *J Biol Chem* 277, 4477-4484.
- Lue, R. A., Marfatia, S. M., Branton, D., and Chishti, A. H. (1994). Cloning and characterization of hdlg: the human homologue of the Drosophila discs large tumor suppressor binds to protein 4.1. *Proc Natl Acad Sci U S A* 91, 9818-9822.
- Manes, S., and Viola, A. (2006). Lipid rafts in lymphocyte activation and migration. *Mol Membr Biol* 23, 59-69.
- Masuko, N., Makino, K., Kuwahara, H., Fukunaga, K., Sudo, T., Araki, N., Yamamoto, H., Yamada, Y., Miyamoto, E., and Saya, H. (1999). Interaction of NE-dlg/SAP102, a neuronal and endocrine tissue-specific membrane-associated guanylate kinase protein, with calmodulin and PSD-95/SAP90. A possible regulatory role in molecular clustering at synaptic sites. *J Biol Chem* 274, 5782-5790.
- McGee, A. W., and Bretz, D. S. (1999). Identification of an intramolecular interaction between the SH3 and guanylate kinase domains of PSD-95. *J Biol Chem* 274, 17431-17436.
- McGee, A. W., Dakoji, S. R., Olsen, O., Bretz, D. S., Lim, W. A., and Prehoda, K. E. (2001). Structure of the SH3-guanylate kinase module from PSD-95 suggests a mechanism for regulated assembly of MAGUK scaffolding proteins. *Mol Cell* 8, 1291-1301.
- McGuffin, L. J., and Jones, D. T. (2003). Improvement of the GenTHREADER method for genomic fold recognition. *Bioinformatics* 19, 874-881.
- McHeyzer-Williams, M. G. (2003). B cells as effectors. *Curr Opin Immunol* 15, 354-361.
- McLaughlin, M., Hale, R., Ellston, D., Gaudet, S., Lue, R. A., and Viel, A. (2002). The distribution and function of alternatively spliced insertions in hDlg. *J Biol Chem* 277, 6406-6412.
- Meiri, K. F. (2005). Lipid rafts and regulation of the cytoskeleton during T cell activation. *Philos Trans R Soc Lond B Biol Sci* 360, 1663-1672.
- Mendieta, J., and Gago, F. (2004). In silico activation of Src tyrosine kinase reveals the molecular basis for intramolecular autophosphorylation. *J Mol Graph Model* 23, 189-198.
- Miletic, A. V., Swat, M., Fujikawa, K., and Swat, W. (2003). Cytoskeletal remodeling in lymphocyte activation. *Curr Opin Immunol* 15, 261-268.
- Monks, C. R., Freiberg, B. A., Kupfer, H., Sciaky, N., and Kupfer, A. (1998). Three-dimensional segregation of supramolecular activation clusters in T cells. *Nature* 395, 82-86.
- Monks, C. R., Kupfer, H., Tamir, I., Barlow, A., and Kupfer, A. (1997). Selective modulation of protein kinase C- θ during T-cell activation. *Nature* 385, 83-86.
- Montgomery, J. M., Zamorano, P. L., and Garner, C. C. (2004). MAGUKs in synapse assembly and function: an emerging view. *Cell Mol Life Sci* 61, 911-929.

- Montoya, M. C., Sancho, D., Vicente-Manzanares, M., and Sanchez-Madrid, F. (2002). Cell adhesion and polarity during immune interactions. *Immunol Rev* 186, 68-82.
- Nair, D. K., Jose, M., Kuner, T., Zuschratter, W., and Hartig, R. (2006). FRET-FLIM at nanometer spectral resolution from living cells. *Optics Express* 14, 12217-12229.
- Nakanishi, J., Takarada, T., Yunoki, S., Kikuchi, Y., and Maeda, M. (2006). FRET-based monitoring of conformational change of the beta2 adrenergic receptor in living cells. *Biochem Biophys Res Commun* 343, 1191-1196.
- Niggli, E., and Egger, M. (2004). Applications of multi-photon microscopy in cell physiology. *Front Biosci* 9, 1598-1610.
- Nix, S. L., Chishti, A. H., Anderson, J. M., and Walther, Z. (2000). hCASK and hDlg associate in epithelia, and their src homology 3 and guanylate kinase domains participate in both intramolecular and intermolecular interactions. *J Biol Chem* 275, 41192-41200.
- Norcross, M. A. (1984). A synaptic basis for T-lymphocyte activation. *Ann Immunol (Paris)* 135D, 113-134.
- O'Connor, D. V., and Phillips, D. (1984). *Time-Correlated Single Photon Counting* (New York, Academic Press).
- Paarmann, I., Spangenberg, O., Lavie, A., and Konrad, M. (2002). Formation of complexes between Ca²⁺-calmodulin and the synapse-associated protein SAP97 requires the SH3 domain-guanylate kinase domain-connecting HOOK region. *J Biol Chem* 277, 40832-40838.
- Palacios, E. H., and Weiss, A. (2004). Function of the Src-family kinases, Lck and Fyn, in T-cell development and activation. *Oncogene* 23, 7990-8000.
- Patel, V. P., Moran, M., Low, T. A., and Miceli, M. C. (2001). A molecular framework for two-step T cell signaling: Lck Src homology 3 mutations discriminate distinctly regulated lipid raft reorganization events. *J Immunol* 166, 754-764.
- Patterson, G. H., Piston, D. W., and Barisas, B. G. (2000). Forster distances between green fluorescent protein pairs. *Anal Biochem* 284, 438-440.
- Paul, W. E., and Seder, R. A. (1994). Lymphocyte responses and cytokines. *Cell* 76, 241-251.
- Pepperkok, R., Squire, A., Geley, S., and Bastiaens, P. I. (1999). Simultaneous detection of multiple green fluorescent proteins in live cells by fluorescence lifetime imaging microscopy. *Curr Biol* 9, 269-272.
- Randriamampita, C., and Trautmann, A. (2004). Ca²⁺ signals and T lymphocytes; "New mechanisms and functions in Ca²⁺ signalling". *Biol Cell* 96, 69-78.
- Regalado, M. P., Terry-Lorenzo, R. T., Waites, C. L., Garner, C. C., and Malenka, R. C. (2006). Transsynaptic signaling by postsynaptic synapse-associated protein 97. *J Neurosci* 26, 2343-2357.
- Rizzo, M. A., Springer, G. H., Granada, B., and Piston, D. W. (2004). An improved cyan fluorescent protein variant useful for FRET. *Nat Biotechnol* 22, 445-449.
- Roskoski, R., Jr. (2004). Src protein-tyrosine kinase structure and regulation. *Biochem Biophys Res Commun* 324, 1155-1164.

- Roskoski, R., Jr. (2005). Src kinase regulation by phosphorylation and dephosphorylation. *Biochem Biophys Res Commun* 331, 1-14.
- Round, J. L., Humphries, L. A., Tomassian, T., Mittelstadt, P., Zhang, M., and Miceli, M. C. (2007). Scaffold protein Dlg1 coordinates alternative p38 kinase activation, directing T cell receptor signals toward NFAT but not NF-kappaB transcription factors. *Nat Immunol* 8, 154-161.
- Round, J. L., Tomassian, T., Zhang, M., Patel, V., Schoenberger, S. P., and Miceli, M. C. (2005). Dlg1 coordinates actin polymerization, synaptic T cell receptor and lipid raft aggregation, and effector function in T cells. *J Exp Med* 201, 419-430.
- Rumbaugh, G., Sia, G. M., Garner, C. C., and Huganir, R. L. (2003). Synapse-associated protein-97 isoform-specific regulation of surface AMPA receptors and synaptic function in cultured neurons. *J Neurosci* 23, 4567-4576.
- Santana, M. A., and Esquivel-Guadarrama, F. (2006). Cell biology of T cell activation and differentiation. *Int Rev Cytol* 250, 217-274.
- Seifert, M. H., Ksiazek, D., Azim, M. K., Smialowski, P., Budisa, N., and Holak, T. A. (2002). Slow exchange in the chromophore of a green fluorescent protein variant. *J Am Chem Soc* 124, 7932-7942.
- Sekar, R. B., and Periasamy, A. (2003). Fluorescence resonance energy transfer (FRET) microscopy imaging of live cell protein localizations. *J Cell Biol* 160, 629-633.
- Shaner, N. C., Steinbach, P. A., and Tsien, R. Y. (2005). A guide to choosing fluorescent proteins. *Nat Methods* 2, 905-909.
- Shaw, A. S., Gauen, L. K., and Zhu, Y. (1995). Interactions of TCR tyrosine based activation motifs with tyrosine kinases. *Semin Immunol* 7, 13-20.
- Shin, H., Hsueh, Y. P., Yang, F. C., Kim, E., and Sheng, M. (2000). An intramolecular interaction between Src homology 3 domain and guanylate kinase-like domain required for channel clustering by postsynaptic density-95/SAP90. *J Neurosci* 20, 3580-3587.
- Sicheri, F., and Kuriyan, J. (1997). Structures of Src-family tyrosine kinases. *Curr Opin Struct Biol* 7, 777-785.
- Sicheri, F., Moarefi, I., and Kuriyan, J. (1997). Crystal structure of the Src family tyrosine kinase Hck. *Nature* 385, 602-609.
- Sims, T. N., and Dustin, M. L. (2002). The immunological synapse: integrins take the stage. *Immunol Rev* 186, 100-117.
- Stradal, T. E., Pusch, R., and Kliche, S. (2006). Molecular regulation of cytoskeletal rearrangements during T cell signalling. *Results Probl Cell Differ* 43, 219-244.
- Suhling, K., Siegel, J., Phillips, D., French, P. M., Leveque-Fort, S., Webb, S. E., and Davis, D. M. (2002). Imaging the environment of green fluorescent protein. *Biophys J* 83, 3589-3595.
- Tavares, G. A., Panepucci, E. H., and Brunger, A. T. (2001). Structural characterization of the intramolecular interaction between the SH3 and guanylate kinase domains of PSD-95. *Mol Cell* 8, 1313-1325.

- Tezuka, T., Umemori, H., Akiyama, T., Nakanishi, S., and Yamamoto, T. (1999). PSD-95 promotes Fyn-mediated tyrosine phosphorylation of the N-methyl-D-aspartate receptor subunit NR2A. *Proc Natl Acad Sci U S A* 96, 435-440.
- Thomas, U., Ebitsch, S., Gorczyca, M., Koh, Y. H., Hough, C. D., Woods, D., Gundelfinger, E. D., and Budnik, V. (2000). Synaptic targeting and localization of discs-large is a stepwise process controlled by different domains of the protein. *Curr Biol* 10, 1108-1117.
- tom Dieck, S., Sanmarti-Vila, L., Langnaese, K., Richter, K., Kindler, S., Soyke, A., Wex, H., Smalla, K. H., Kampf, U., Franzer, J. T., *et al.* (1998). Bassoon, a novel zinc-finger CAG/glutamine-repeat protein selectively localized at the active zone of presynaptic nerve terminals. *J Cell Biol* 142, 499-509.
- Torres, E., and Rosen, M. K. (2006). Protein-tyrosine kinase and GTPase signals cooperate to phosphorylate and activate Wiskott-Aldrich syndrome protein (WASP)/neuronal WASP. *J Biol Chem* 281, 3513-3520.
- Tramier, M., Kemnitz, K., Durieux, C., and Coppey-Moisán, M. (2004). Picosecond time-resolved microspectrofluorometry in live cells exemplified by complex fluorescence dynamics of popular probes ethidium and cyan fluorescent protein. *J Microsc* 213, 110-118.
- Tramier, M., Piolot, T., Gautier, I., Mignotte, V., Coppey, J., Kemnitz, K., Durieux, C., and Coppey-Moisán, M. (2003). Homo-FRET versus hetero-FRET to probe homodimers in living cells. *Methods Enzymol* 360, 580-597.
- Truong, K., Sawano, A., Mizuno, H., Hama, H., Tong, K. I., Mal, T. K., Miyawaki, A., and Ikura, M. (2001). FRET-based in vivo Ca²⁺ imaging by a new calmodulin-GFP fusion molecule. *Nat Struct Biol* 8, 1069-1073.
- Tseng, S. Y., and Dustin, M. L. (2002). T-cell activation: a multidimensional signaling network. *Curr Opin Cell Biol* 14, 575-580.
- Tsien, R. Y. (1998). The green fluorescent protein. *Annu Rev Biochem* 67, 509-544.
- Vyas, Y. M., Maniar, H., and Dupont, B. (2002). Visualization of signaling pathways and cortical cytoskeleton in cytolytic and noncytolytic natural killer cell immune synapses. *Immunol Rev* 189, 161-178.
- Wouters, F. S., and Bastiaens, P. I. (1999). Fluorescence lifetime imaging of receptor tyrosine kinase activity in cells. *Curr Biol* 9, 1127-1130.
- Wu, H., Reissner, C., Kuhlendahl, S., Coblenz, B., Reuver, S., Kindler, S., Gundelfinger, E. D., and Garner, C. C. (2000). Intramolecular interactions regulate SAP97 binding to GKAP. *Embo J* 19, 5740-5751.
- Wu, P., and Brand, L. (1994). Resonance energy transfer: methods and applications. *Anal Biochem* 218, 1-13.
- Xavier, R., Rabizadeh, S., Ishiguro, K., Andre, N., Ortiz, J. B., Wachtel, H., Morris, D. G., Lopez-Illasaca, M., Shaw, A. C., Swat, W., and Seed, B. (2004). Discs large (Dlg1) complexes in lymphocyte activation. *J Cell Biol* 166, 173-178.
- Xu, W., Doshi, A., Lei, M., Eck, M. J., and Harrison, S. C. (1999). Crystal structures of c-Src reveal features of its autoinhibitory mechanism. *Mol Cell* 3, 629-638.

- Yamaguchi, H., and Hendrickson, W. A. (1996). Structural basis for activation of human lymphocyte kinase Lck upon tyrosine phosphorylation. *Nature* 384, 484-489.
- Zal, T., and Gascoigne, N. R. (2004). Using live FRET imaging to reveal early protein-protein interactions during T cell activation. *Curr Opin Immunol* 16, 418-427.
- Zamoyska, R., Basson, A., Filby, A., Legname, G., Lovatt, M., and Seddon, B. (2003). The influence of the src-family kinases, Lck and Fyn, on T cell differentiation, survival and activation. *Immunol Rev* 191, 107-118.
- Zhang, J., Campbell, R. E., Ting, A. Y., and Tsien, R. Y. (2002). Creating new fluorescent probes for cell biology. *Nat Rev Mol Cell Biol* 3, 906-918.
- Zheng, L., Hoeflich, K. P., Elsby, L. M., Ghosh, M., Roberts, S. G., and Ikura, M. (2004). FRET evidence for a conformational change in TFIIB upon TBP-DNA binding. *Eur J Biochem* 271, 792-800.

ABBREVIATIONS

% (vol/vol)	percent by volume
% (w/v)	percent by mass
3D	three dimensional
°C	Degree Celsius
µg	microgram
µl	microlitre
µm	micrometer
µM	micromolar
λ	wavelength
κ ²	Orientation factor
τ	lifetime
τ _D	Donor lifetime
τ _{DA}	Donor lifetime in presence of acceptor
τ _{mean}	Mean lifetime
aa	amino acid
APC	Antigen Presenting Cells
Arp2/3	seven-subunit protein containing Actin-Related Proteins 2 and 3
a.u.	Absolute units
bp	base pair
BSA	bovine serum albumin
Ca ²⁺	calcium ion
CCD	Charge Coupled Device
CD	cluster of differentiation
cDNA	complementary DNA
CFD	Constant Fraction Discriminator
CFP	Cyan Fluorescent Protein
Cl ⁻	Chloride ion
C-SMAC	Cental Supra Molecular Activation Clusture
CNS	Central Nervous System
COS-7	african green monkey cell line
C-terminal	carboxy-terminal
DAS	Decay Associated Spectra
DC	Dendritic Cells
DIC	Differential Interference Contrast
DL	Delay Line
DMEM	Dulbecco's Modified Eagle Medium
DNA	deoxyribonucleic acid
DNase	deoxyribonuclease
D-SMAC	Distal Supra Molecular Activation Clusture
ECFP	Enhanced CFP
E. coli	<i>Escherichia coli</i>
EDTA	ethylenediamine-N,N,N',N'-tetraacetic acid
EGFP	Enhanced GFP

EGTA	ethylene glycol-bis(2-aminoethylether)-N,N,N',N'-tetraacetic acid
EYFP	Enhanced YFP
FC	Fibre coupler
Fig	Figure
FLIM	Fluorescence Lifetime Imaging Microscopy
FLMS	Fluorescence Lifetime Imaging Micro-Spectroscopy
FRET	Förster's/Fluorescence Resonance Energy Transfer
FWHM	Full Width at Half Maximum
g	gram
GABA	γ Amino butyric acid
GFP	green fluorescent protein
GUK	Guanylate kinase Domain
HBSS	Hank's Balanced salts
Hck	Hemopoietic cell kinase
hDlg	Human Discs Large
HEPES	4-2-hydroxyethyl-1-piperazineethanesulfonic acid
Hg	mercury
Hz	Herz
IF	immunofluorescence
I	iris
Ig	immunoglobulin
IP	immunoprecipitation
kb	Kilo base pair
KD	Karl Diesseroth
kDa	kilo Dalton
l	litre
L	lens
LASER	Light Amplification by Stimulated Emission of Radiation
LAT	Linker of Activated T cells
LB	lysogeny broth
Lck	Lymphocyte Specific Protein tyrosine kinase
M	molar
M1-4	Mirrors 1-4
mA	Milli Ampere
MAGUK	Membrane Associated Guanylate kinase
MCA	Multichannel Analyser
MCP	Multichannel Plate
MHC	Major Histocompatibility Complex
min	minutes
ml	Milli litre
mM	millimolar
N	Normal
n	number of measured cells
ND	Neutral density
nm	nanometer

ns	nanosecond
N-terminal	amino-terminal
OCFD	Optical Constant Fraction Discriminator
PAGE	polyacrylamide gel electrophoresis
PC	Personal Computer
PBS	phosphate buffered saline
PCR	polymerase chain reaction
PDZ	PSD-95/Dlg/ZO-1
PKA	Protein kinase A
PLC γ_1	Phospholipase C γ_1 isoform
PMT	Photo-Multiplier Tube
ps	picosecond
PSD	postsynaptic density
PSD 95	Postsynaptic Density Protein of 95 kDa
P-SMAC	Peripheral Supra Molecular Activation Clusture
QA	Quadrant Anode
R	Intensity ratio of acceptor to donor emission maxima
RNase	ribonuclease
rpm	revolutions per minute
RT	Room temperature
sec	second
SAP	Synapse-associated Protein
SAP 90	Synapse-associated Protein of 90 kDa
SAP 97	Synapse-associated Protein of 97 kDa
SH2	Src homology domain type 2
SH3	Src homology domain type 3
SMAC	Supra Molecular Activation Clusture
S.O.C:	Super Optimal catobolite repression
TAE	Tris-Acetate-EDTA
TAC	Time to Amplitude Converter
Taq	<i>Thermus aquaticus</i>
TBE	Tris-Borate-EDTA
TCR	T cell Receptor
TRES	Time Resolved Emission Spectra
U	unit
UV	ultraviolet
Vav	The 'onc F' proto-oncogene
WASP	Wiscott-Aldrich Syndrome Protein
WB	Western blot
Xe	xenon
YFP	Yellow Fluorescent Protein
ZAP-70	Zeta-chain-associated protein kinase 70

CURRICULAM VITAE

Personal information

- Name: Deepak
- Family Name: Kumaran Nair
- Date of birth: 10th March 1980
- Place of birth: Mararikulam, Kerala, India
- Nationality: Indian
- Parents: Padmanabhapilla, Kumaran Nair
Lalithamma, Thayyil Subhadramma
- Spouse: Mini Jose
- Child: Naina Maria

Academic background

1990-1997	<i>Pre Degree</i> Sainik School Kazhakootam, Trivandrum, Kerala, India
1997-2000	<i>Bachelor of Science/Physics</i> S.N.College, Kerala University, Cherthala, Kerala, India
2000-2002	<i>Master of Science/Physics</i> Indian Institute of Technology, Madras, TamilNadu, India
2003-2007	<i>PhD/Biophysics</i> Leibniz Institute for Neurobiology, Magdeburg, Germany

Awards received

1993-1997	Defence scholarship for academic excellence
1997-2000	Recognition for merit
2002	GATE: Graduate Aptitude Test For Engineering
Since 2007	Invited student member, Optical Society of America

Scientific projects

2001	Project work on ‘‘Photothermal Optics Induced by Lasers’’, International School of Photonics, Cochin University of Science and Technology, Kerala, India
2001-2002	Master’s project on ‘Lateral Shear Interferometers using Phase Gratings’’, Laboratory of Applied Optics, Indian Institute of Technology, Madras, India
2002-2003	Project on ‘‘Fluorescence Quenching of Flavin Adenine Dinucleotide in Aqueous Solution by pH Dependent Isomerisation and Photo-Induced Electron Transfer’’. Institute für Experimentel and Applied Physics, University of Regensburg, Germany

Scientific services

Since 2007	Reviewer, journals of Optical Society of America
------------	--------------------------------------------------

SCIENTIFIC PUBLICATIONS

Published Articles

2006

DK Nair, M. Jose, T. Kuner, W. Zuschratter, and R. Hartig, „FRET-FLIM at nanometer spectral resolution from living cells", Opt. Express **14**, 12217-12229 (2006)

(selected for republication in virtual journal of Biomedical Optics)

<http://www.opticsinfobase.org/abstract.cfm?URI=oe-14-25-12217>

First author, Corresponding author

Jose M, **Nair DK**, Reissner C, Hartig R, Zuschratter W, "Photophysics of Clomeleon by FLIM: discriminating excited state reactions along neuronal development", Biophys J., 92, 6, 2237-2254 (2007)

<http://www.biophysj.org/cgi/rapidpdf/biophysj.106.092841v1>

equal author

Jose M, **Nair DK**, Altrock WD, Dresbach T, Gundelfinger ED, Zuschratter W, "Investigating Interactions mediated by the presynaptic protein Bassoon in living cells by FRET-FLIM" Biophys. J accepted for publication

equal author

Posters and Abstracts

2003

Shafiq-ul-islam, **Deepak Nair**, Peter Hegemann, Alfons Penzkofer

‘Sensory Photoreceptors in natural and Artificial Systems’, Regensburg, Jan 2003
‘Fluorescence Quenching of Flavin Adenine Dinucleotide in Aqueous Solution by pH Dependent Isomerisation and Photo-Induced Electron Transfer’.

Werner Zuschratter, Mini Jose, **Deepak Nair**, Daniela Dieterich , Thomas Dresbach, Eckart D Gundelfinger, Martin Kreutz, Michael Kreutz, Klaus Kemnitz.

Proceedings of Göttingen Neurobiology Conference, June 2003 “Fluorescence Lifetime Imaging and Spectroscopy of xFP-fused Proteins in Hippocampal Cell Cultures using Ultra-Low Excitation Levels and Ultra-Sensitive Imaging Detectors”

Mini Jose, **Deepak Nair**, Klaus Kemnitz, Werner Zuschratter.

Ultra school on ‘Ultrafast processes in Photochemistry and Photobiology’, Torun, Poland, Aug 2003 “Fluorescence analysis of molecular dynamics in the synaptic cytomatrix at ultra-low excitation levels”.

Deepak Nair, Mini Jose, Klaus Kemnitz, Zdenek Petrasek, Werner Zuschratter.

Ultra school on 'Ultrafast processes in Photochemistry and Photobiology', Torun, Poland Aug 2003 "FLIM at minimal invasive conditions: Microspectroscopy of the living state".

2004

Mini Jose, **Deepak Nair**, Thomas Kuner, Thomas Dresbach, Eckart D. Gundelfinger, Klaus Kemnitz, Werner Zuschratter.

First Westerburg Symposium, 'Spinogenesis and Synaptic Plasticity' Westerburg, Aug 2004 "Imaging interactions in living hippocampal neurons at minimal invasive conditions using the chloride indicator Clomeleon"

Ronald Steffen, Mini Jose, **Deepak Nair**, Thomas Dresbach, Thomas Kuner, Eckart D. Gundelfinger, Klaus Kemnitz, Werner Zuschratter.

Annual meeting of SPP 1128 Supramolecular biostructures, Asselheim, Nov 2004 "Fluorescence lifetime imaging Microspectroscopy using ultra low excitation levels and ultra sensitive imaging detectors".

2005

Mini Jose, **Deepak Nair**, Thomas Dresbach, Klaus Kemnitz, Michael Kreutz, Eckart D. Gundelfinger and Werner Zuschratter.

Proceedings of Göttingen Neurobiology Conference, Feb2005 "FRET in calcium indicator Cameleon and chloride indicator Clomeleon with maturation of hippocampal neurons"

Deepak Nair, Mini Jose, Thomas Kuner, Roland Hartig, Carsten Reissner, Klaus Kemnitz, Michael Kreutz, Eckart. D. Gundelfinger and Werner Zuschratter.

Proceedings of Göttingen Neurobiology Conference, Feb 2005, "Mapping distances between chromophores in macromolecules using FRET FLIM microscopy: comparison with predicted 3D structures"

Mini Jose, **Deepak Nair**, Ronald Steffen, Roland Hartig, Thomas Kuner, Klaus Kemnitz, Werner Zuschratter.

Focus on Microscopy, Jena, March 2005 "FRET in calcium indicator Cameleon and chloride indicator Clomeleon with maturation of hippocampal neurons".

Deepak Nair, Mini Jose, Ronald Steffen, Roland Hartig, Thomas Kuner, Carsten Reissner, Klaus Kemnitz, Werner Zuschratter.

Focus on Microscopy, Jena, March 2005 "Mapping distances between chromophores in macromolecules using FRET-FLIM microscopy: comparison with predicted 3D structures"

Mini Jose, **Deepak Nair**, Ronald Steffen, Roland Hartig, Thomas Kuner, Klaus Kemnitz, Werner Zuschratter.

XIth Magdeburg International Neurobiological symposium 'Learning and Memory: Cellular and Systemic Views', May 2005 "Visualisation of Interactions in Living Cells at Minimal Invasive Conditions"

Deepak Nair, Mini Jose, Ronald Steffen, Roland Hartig, Thomas Kuner, Carsten Reissner, Klaus Kemnitz, Werner Zuschratter.

XIth Magdeburg International Neurobiological symposium 'Learning and Memory: Cellular and Systemic Views', May 2005 "Imaging Interactions in Living Hippocampal Neurons Using the Chloride Indicator Clomeleon"

2006

Mini Jose, **Deepak Nair**, Wilko Altmann, Thomas Dresbach, Thomas Kuner, Carsten Reissner, Eckart D. Gundelfinger, Werner Zuschratter.

International Symposium, Optical Analysis of Biomolecular Machines Berlin, July 2006 "Imaging spatial and temporal interaction profiles of proteins in living cells using FRET-FLIM"

Deepak Nair, Mini Jose, Roland Hartig, Thomas Kuner, Klaus Kemnitz, Werner Zuschratter.

International Symposium, Optical Analysis of Biomolecular Machines Berlin, July 2006 "Fluorescence Lifetime Imaging of protein-protein interactions in living hippocampal neurons"

Invited talks

Forschungsseminar, IFN, Bernburg, Sep 2004 "Imaging protein interactions in living cells."

University of Bordeaux 2, Bordeaux, April 2007 "Spatial and temporal profiles of conformational changes of multidomain proteins in living cells"